University of Naples “Federico II”

C.I.R.A.M. - Interdepartmental Centre for Environmental Research

PhD School in Earth Sciences

PhD Course in Environmental Systems Analysis

XXVII cycle

PhD thesis

An hybrid Imaging-Inversion method applied to potential fields data

Daniela Mastellone

Tutor:
Prof. Maurizio Fedi

PhD Coordinator:
Prof. Maurizio Fedi

Table of contents

Summary

The aim of this thesis is to implement an integrated approach of potential fields data analysis, which combines the most employed inversion techniques (Li & Oldenburg, 1996; Pilkington, 1997; Zhdanov, 2002; Fedi et al., 2005) with multi-scale imaging methodologies (i.e. DEXP from Fedi (2007), or others (Fedi and Pilkington, 2012)).

Such a complementary approach brings two focal benefits: on the one hand, a multi-scale analysis will provide us with valuable information, e.g. excess mass (magnetization intensity), source shape parameters and source depth, which we will use in the inversion algorithms. On the other hand, the imaging methods could be extended by defining a density/magnetization model based on various type of constraints (density/magnetization contrast, source compactness), as usual for inversion algorithms.

Within the scope of this research work, the first above-mentioned aspect has been further investigated, in particular for data coming from “non-simple” sources; their multi-scale behaviour and characteristics have been first analysed and then transferred into the inversion domain.

In order to estimate source properties in the multi-scale domain, we referred to the DEXP method (Fedi, 2007) among the imaging approaches, while to perform 2D constrained inversion, we pertained to Li & Oldenburg algorithm (1996), taking into account also the suggestions by Cella et al. (2012).

We had to adjust both the reference inversion and the imaging methods we chose for this research work to make them suitable for the integration: first, constraints on source shape, depth and density/magnetization range had to be set in the inversion domain. More specifically, we used one of the outputs of the DEXP transform, called scaling exponent, as an inversion constrain.

After defining a preliminary workflow, simple source magnetic anomalies have been synthetically generated to test the proposed approach; then, data caused by more complex sources have been analysed. Finally, some real data from the Bouguer gravity anomaly in the Campanian Plain (Italy) have been examined to have a further confirmation of the effectiveness of the method.

Both tests on synthetic and real data showed that adding, as inversion constraints, source information retrieved by a multiscale analysis of the data has

a great potential to lead to well-constrained solutions with respect to the source depth and to the horizontal variations of the source-density/magnetization intensity distribution.

Throughout the development of the main topic of this thesis, we have also expanded our research field inpecting the upward continuation transform of potential field data. We got involved in this issue because multi-scale imaging methods such as the continuous wavelet transform (Sailhac et al., 2003; Fedi et al., 2010; Fedi and Cascone, 2011), the DEXP transformation (Fedi, 2007) and the multiridge analysis (Cella et al., 2009) involve potential fields data available on a 3D volume, which in turn is generated by upward continuation of data measured at a single - flat or draped - surface.

Fedi and Pilkington (2012) show that multiscale imaging techniques are highly influenced by the way the field is upward continued, apart from the depth-weighting factor.

Therefore, we defined an alternative approach to upward continue potential field data: the VOCO (Volume Continuation), which has important advantages above existing techniques and is suitable for all types of data continuation between surfaces in the space. VOCO has also been coupled with second order horizontal derivatives of gravimetric data to investigate on the estimate of the sources horizontal limits changing the field continuation height value.

Papers regarding the VOCO approach will be introduced in the last chapter and attached at the bottom of this text.

Introduction

Discovering and evaluating the potential of oil or gas deposits, or energy and environmental resources in general (i.e. minerals and water), requires the integration of information gathered from geology, drilling, seismology, EM, potential fields and others. The final goal, is, obviously, to gain a good estimate of the in place volumes and to plan the discovered resources production in the best way.

Even if seismic reflection is still the primary exploration method of exploring for energy, the use of gravity and magnetic methods is continuously expanding, thanks to their successful contribution in deeper and more challenging environments, such as sub-salt structures and deep sea, to their smaller cost and to new powerful methods of analysis and modelling, which are indeed related to high-quality and high-resolution data.

Moreover, information provided by inverting 3D sets of gravity and magnetic data can help to refine the targets and so to efficiently define and focus projects early on, in order to minimize the risk of investigation before the actual potential is defined.

Additionally, these methods can be successfully, applied in the environmental and engineering areas of interest, to assess the size of existing issues and to mitigate consequences, for example forecasting polluting fluids movements and leading future drilling tests.

Moreover, measured data, once have been analysed and interpreted, can be used as input to model various systems, to prevent future environmental and engineering critical situations.

Two of the most valuable methods to gain relevant information from potential field data are inversion and multi-scale imaging methods

The multi-scale method investigated in this work is the Depth from Extreme Points (DEXP) method (Fedi, 2007). The DEXP method is used in potential field in order to get a fast imaging of the source distribution and to have information about the depth to the source, the structural index, N, and the mass or magnetic moment modulus, respectively for gravity and magnetic data (Fedi, 2007). In particular, this method fits in the framework of semi-automatic methods, as Euler Deconvolution method, used in potential field to estimate the

source position and N (Reid el al, 1990). N is a source-dependent parameter, which corresponds to the fall- off rate of the field with distance for many, but not all, ideal sources. A more general meaning of N is that it is the opposite of the homogeneity degree of the field.

On the other hand inversion methods allow deriving the distribution of some physical properties of the earth rocks (density or magnetization intensity for gravity and magnetic fields data respectively) solving an inverse problem starting from measured data.

In the first three sections of this thesis an overview of the key topics involved in this research work will be given: first a general introduction on potential fields theory, then the state of art on inversion theory and multi-scaling imaging techniques.

Then the novel approach of multi-scale inversion of potential field data will be described, focusing on how multi-scale (even fractional) source-related information have been included in the inversion procedure. Several examples of single-source and multi-source synthetic data will be analysed, finally real data will be also inspected and conclusions settled.

1. Potential fields theory

Gravitational and magnetic fields are both potential fields. In the mass free space, potential fields obey Laplace's equation, which states that the sum of the rates of change of the field gradient in three orthogonal directions is zero (Kearey et al., 2002). In Cartesian coordinates, Laplace's equation is:

$$\frac{\partial^2 \phi}{\partial x^2} + \frac{\partial^2 \phi}{\partial y^2} + \frac{\partial^2 \phi}{\partial z^2} = 0 \qquad (\mathbf{1.1})$$

where ϕ refers to a gravitational or magnetic field and is a function of (x, y, z).

1.1. Gravity field

The gravitational field is defined in terms of the gravitational potential U:

$$U = \frac{\gamma M}{r} \qquad (\mathbf{1.2})$$

Where γ is the Gravitational Constant, M is the mass of the Earth, and r is the distance from the centre of the Earth.
The first derivative of U in any directions gives the component of gravity in that direction (Kearey et al., 2002).
The gradient of U is equal to the gravity g:

$$g = \nabla U \qquad (\mathbf{1.3})$$

So the gravity field g is:

$$g = \nabla^2 U = \frac{\partial^2 U}{\partial x^2} i + \frac{\partial^2 U}{\partial y^2} j + \frac{\partial^2 U}{\partial z^2} k = 0 \qquad (\mathbf{1.4})$$

Where i, j, k represents unit vectors in the direction of the positive x, y, z axes respectively. The gradient of the gravity field g is:

$$\nabla g = \nabla^2 U = \frac{\partial^2 U}{\partial x^2} + \frac{\partial^2 U}{\partial y^2} + \frac{\partial^2 U}{\partial z^2} \qquad (\mathbf{1.5})$$

In non "mass-free" space:

$$\nabla g = \nabla^2 U = 4\pi\gamma\rho \qquad (\mathbf{1.6})$$

ρ is the density of mass distribution at the point considered. Equation 1.6 is Poisson's equation and describes the potential at all points, even inside the mass distribution. Laplace's equation (1.1) is simply a special case of Poisson's equation valid for mass-free regions of space (Blakely 1996).
Gravimeters measure the vertical component of g given by:

$$g_z = \frac{\partial g}{\partial z} \qquad (\mathbf{1.6b})$$

Before the results of a gravity survey can be interpreted it is necessary to correct for all variation in the Earth's gravitational field, which do not result from the differences of density in the underlying rocks. The observed gravity is the sum of the following components (Blakely, 1996):

- attraction of the reference ellipsoid (theoretical gravity)
- effect of elevation above sea level (free air effect)
- effect of "normal" mass above sea level (Bouguer slab and terrain effects)
- time-dependent variations (tidal and instrumental drift effects)
- effect of moving platform (Eötvös effect)
- effect of masses that support topographic loads (isostatic effects)
- effect of crust and upper mantle density variations ("geology").

Our goal is to isolate the last quantity, the effect of crustal and upper mantle density variations, from all other terms. This process is referred to as gravity reduction. The mean value of gravity at the Earth's surface is about 9.8 ms^{-2}. Variations in gravity caused by density variation in the subsurface are of the order of 100 μms^{-2}. In honour of Galileo, the cgs unit of acceleration due to gravity (1 cms^{-2}) is the Gal and its sub-units milliGal (1 mGal=10^{-3} Gals) (Kearey et al. 2002). The measurement of gravity gradients is often given in the Eötvös unit, which equals 10^{-4} mGal/m or 0.1 mGal/km.

1.2. Magnetic field

Magnetic fields can be defined in term of magnetic potentials in a manner similar to gravitational fields. For a single dipole of strength m the magnetic potential V at a distance r from the pole is given by:

$$V = \frac{\mu_0 m}{4\pi\mu_r r} \quad (\mathbf{1.7})$$

where μ_0 and μ_r are the free space magnetic permeability and the relative magnetic permeability of the medium separating the poles respectively (Kearey et al. 2002).

Magnetic field can also be defined in terms of a force field which is produced by electric currents. This magnetizing field strength H is defined as being the field strength at the centre of a loop of wire of radius r through which a current I is flowing such that H=I/2r.

Materials can acquire a component of magnetization in the presence of an external magnetic field. For low-amplitude magnetic fields, say on the order of the Earth's magnetic field, this induced magnetization is proportional in magnitude and is parallel (or antiparallel) in direction to the external field, that is:

$$M_i = \chi H \quad (\mathbf{1.8})$$

The proportionality constant χ is called the magnetic susceptibility (Blakely, 1996).

Susceptibility is in essence a measure of how susceptible a material is to becoming magnetized (Reynolds, 1997) and is dimensionless.

The susceptibility χ is related to magnetic permeability □ by the following equation:

$$\mu = \mu_0(1+\chi) \quad (\mathbf{1.9})$$

where μ_0 is the free space magnetic permeability.

The magnetic permeability μ_0 correlates the magnetic induction field B with magnetization H:

$$B = \mu H \quad (\mathbf{1.10})$$

The relationship between M and H is not necessarily linear as implied by equation 1.8; χ may vary with field intensity, may be negative, and may be represented more accurately in some materials as a tensor.

There are many kinds of magnetization (Blakely, 1996).

Diamagnetism, for example, is an inherent property of all matter. In diamagnetism, an applied magnetic field disturbs the orbital motion of electrons in such a way as to induce a small magnetization in the opposite sense to the applied field. Consequently, diamagnetic susceptibility is negative.

Paramagnetism is a property of those solids that have atomic magnetic moments.
Application of a magnetic field causes the atomic moments to partially align parallel to the applied field thereby producing a net magnetization in the direction of the applied field. Thermal effects tend to oppose this alignment, and paramagnetism vanishes in the absence of applied fields because thermal effects act to randomly orient the atomic moments. All minerals are diamagnetic and some are paramagnetic, but in either case these magnetizations are insignificant contributors to the geomagnetic field.

There is, however, a class of magnetism of great importance to geomagnetic studies.
Certain materials not only have atomic moments, but neighbouring moments interact strongly with each other. This interaction is a result of a quantum mechanical effect called exchange energy. Suffice it to say that the exchange energy causes a spontaneous magnetization that is many times greater than paramagnetic or diamagnetic effects. Such materials are said to be ferromagnetic. There are various kinds of ferromagnetic materials too, depending on the way that the atomic moments align. These include ferromagnetism proper, in which atomic moments are aligned parallel to one another; antiferromagnetism, where atomic moments are aligned antiparallel and cancel one another; and ferrimagnetism, in which atomic moments are antiparallel but do not cancel. At the scale of individual mineral grains, spontaneous magnetization of a ferromagnetic material can be very large. At the outcrop scale, however, the magnetic moments of individual ferromagnetic grains may be randomly oriented, and the net magnetization may be negligible. The magnetization of individual grains is affected, however, by the application of a magnetic field, similar to but far greater in magnitude than for paramagnetism. Hence, rocks containing ferromagnetic minerals will acquire a net magnetization, called induced magnetization and denoted by Mi, in the direction of an applied field H, where of course the Earth's magnetic field produces the same response in such materials, and the material is magnetic in its natural state. In small fields, with magnitudes comparable to the earth's magnetic field, the relationship between induced magnetization and applied

field is essentially linear, and the susceptibility χ is constant. Induced magnetization falls to zero if the rock is placed in a field-free environment. However, ferromagnetic materials also have the ability to retain a magnetization even in the absence of external magnetic fields.
This permanent magnetization is called remanent magnetization, which we denote here by Mr. In crustal materials, remanent magnetization is a function not only of the atomic, crystallographic, and chemical make-up of the rocks, but also of their geologic, tectonic, and thermal history. In geophysical studies, it is customary to consider the total magnetization M of a rock as the vector sum of its induced and remanent magnetizations, that is:

$$M = M_i + M_r = \chi H + M_r \qquad \textbf{(1.11)}$$

The relative importance of remanent magnetization Mr to induced magnetization Mi is expressed by the Koenigsberger ratio Q:

$$Q = \frac{M_r}{M_i} \qquad \textbf{(1.12)}$$

These may be oriented in different direction and may differ significantly in magnitude. The magnetic effects of a rock arise from the resultant M of the two magnetization vectors.
Magnetic anomalies caused by rocks are localized effects superimposed on the normal magnetic field of the Earth. Consequently, knowledge of the behavior of the magnetic field is necessary both in the reduction of magnetic data to a suitable datum and in the interpretation of the resulting anomalies. The magnetic field is geometrically more complex than the gravity field of the Earth and exhibits irregular variation in both orientation and magnitude with latitude, longitude and time (Kearey et al. 2002).
Total-field magnetometers are usually the instrument of choice for airborne and shipborne magnetic surveys. As the name implies, total-field magnetometers measure the magnitude of the total magnetic field without regard to its vector direction.
The total field T is given by:

$$T = F + \Delta F \qquad \textbf{(1.13)}$$

where and F is the geomagnetic field and ΔF represents the perturbation of F due to some crustal magnetic source.

The total-field anomaly is calculated from total-field measurements by subtracting the magnitude of a suitable regional field, usually the IGRF model appropriate for the date of the survey.
If T represents the total field at any point, and F is the regional field at the same point, then the total-field anomaly is given by (Blakely, 1996):

$$\Delta T = |\mathbf{T}| - |\mathbf{F}| \qquad \textbf{(1.13b)}$$

If $|\mathbf{F}| >> |\Delta\mathbf{F}|$ the total field ΔT can be considered as the component of the anomalous field $\Delta\mathbf{F}$ in the direction of **F** and thus it can be considered a harmonic function (e.g., Blakely, 1996). This condition is usually verified in crustal magnetic studies.
The SI unit of magnetic field strength is the tesla (T). The tesla is too large a unit in which to express the small magnetic anomalies caused by rocks and therefore a subunit, the nanotesla (nT), is commonly used ($1\ nT=10^{-9}T$) (Kearey et al. 2002).
The strength of *F* varies from about 25000 nT in equatorial regions to about 70000 nT at the poles (Kearey et al. 2002).

2. Potential fields inversion

The starting place in most inverse problems[1] is a description of the data. Since in most inverse problems the data are simply a table of numerical values, a vector provides a convenient means of their representation. If N measurements are performed in a particular experiment, for instance, one might consider these numbers as the elements of a vector **d** of length N. Similarly, the model parameters can be represented as the elements of a vector **m** is of length M.

$$\begin{aligned} &\textit{data}: && \mathbf{d} = [d_1, d_2, d_3, d_4, \ldots, d_N]^T \\ &\textit{model parameters}: && \mathbf{m} = [m_1, m_2, m_3, m_4, \ldots, m_M]^T \end{aligned} \qquad (\mathbf{2.1})$$

The basic statement of an inverse problem is that the model parameters and the data are in some way related. This relationship is called the model. Usually the model takes the form of one or more formulas that the data and model parameters are expected to follow.
The simplest and best-understood inverse problems are those that can be represented with the explicit linear equation:

$$\mathbf{A}\,\mathbf{m} = \mathbf{d} \qquad (\mathbf{2.2})$$

The matrix **A** (with N x M dimension) is called kernel, this equation, therefore, forms the foundation of the study of discrete inverse theory. Many important inverse problems that arise in the physical sciences involve precisely this equation. Others, while involving more complicated equations, can often be solved through linear approximations (Menke, 1989).
The simplest kind of solution to an inverse problem is an estimate $\mathbf{m}_{\mathbf{est}}$ of the model parameters. An estimate is simply a set of numerical values for the model parameters.

One remedy to the problem of defining the quality of an estimate is to state additionally some bounds that define its certainty. These bounds can be either absolute or probabilistic. Absolute bounds imply that the true value of the model parameter lies between two stated values. When they exist, bounding

[1] Much of the content of this section follows the book by Menke (1989), which the reader is invited to consult for further details.

values can often provide the supplementary information needed to interpret properly the solution to an inverse problem (Menke, 1989).

2.1. Least-squares solution

When the number of the data (*N*) is greater than the number of model parameters (*M*) the problem in eq. 2.2 is called overdetermined problem.
The simplest of methods for solving this kind of problem is based on measures of the size, or length, of the estimated model parameters $\mathbf{m}_{\mathbf{est}}$ and of the predicted data $\mathbf{d}_{\mathbf{PR}} = \mathbf{A}\,\mathbf{m}_{\mathbf{est}}$.
One of the most common measures of length is the least squares method.
For each observation one defines a prediction error, or misfit, $\mathbf{e_i} = \mathbf{d_i}^{\mathbf{obs}} - \mathbf{d_i}^{\mathbf{pre}}$.
The least square solution is then the one with model parameters that leads to the smallest overall error *E*, defined as:

$$E = e^T e = \sum_{i=1}^{N} e_i^2 \qquad (\mathbf{2.3})$$

The total error *E* (the sum of the squares of the individual errors) is exactly the squared Euclidean length of the vector **e**.
Note that although the Euclidean length (Eq. 2.3) is one way of quantifying the size or length of a vector, it is by no means the only possible measure.
Extending the least squares to general linear inverse problem we obtain the least square solution of the problem 2.2 (Menke, 1989):

$$\mathbf{m} = \left[\mathbf{A}^{\mathbf{T}}\mathbf{A}\right]^{-1}\mathbf{A}^{\mathbf{T}}\mathbf{d} \qquad (\mathbf{2.4})$$

2.2. Minimum length solution

When the number of the data (*N*) is less than the number of model parameters (*M*) the problem in eq. 2.2 is called *underdetermined* problem.
For these problems it is possible to find more than one solution for which the prediction error *E* is zero.
To obtain a solution $\mathbf{m}_{\mathbf{est}}$ to the inverse problem, we must have some means of finding precisely one of the infinite solutions with zero prediction error *E*. To do this, we must add to the problem some information not contained in the equation $\mathbf{A}\,\mathbf{m} = \mathbf{d}$. This extra information is called a priori information and can take many forms, but in each case it quantifies expectations about the character of the solution that are not based on the actual data (Menke, 1989).

The first kind of a priori assumption we shall consider is the expectation that the solution to the inverse problem is “simple,” where the notion of simplicity is quantified by some measure of the length of the solution. One such measure is simply the Euclidean length of the solution:

$$L = m^T m = \sum_{i=1}^{N} m_i \qquad \textbf{(2.5)}$$

A solution is therefore defined to be simple if it is small when measured under the L_2 norm.
The problem we pose is to

find the $\mathbf{m_{est}}$

that minimizes $L = m^T m = \sum_{i=1}^{N} m_i$

subject to the constraint that $\mathbf{e = d - A\,m} = 0$

and we obtain the minimum length solution:

$$\mathbf{m} = \mathbf{A}^{\mathbf{T}}\left[\mathbf{A}\mathbf{A}^{\mathbf{T}}\right]^{-1}\mathbf{d} \qquad \textbf{(2.6)}$$

2.3. Add a priori information

There are many instances in which $L = \mathbf{m}^{\mathbf{T}}\mathbf{m}$ is not a very good measure of solution simplicity. One may not want to find a solution that is smallest in the sense of closest to zero but one that is smallest in the sense that it is closest to some other value. The obvious generalization of eq. 2.5 is then (Menke, 1989):

$$\mathbf{L} = (\mathbf{m}-\mathbf{m_0})^{\mathbf{T}}(\mathbf{m}-\mathbf{m_0}) \qquad \textbf{(2.7)}$$

Where $\mathbf{m_0}$ is the a priori value of the model parameters.
Sometimes the whole idea of length as a measure of simplicity is inappropriate and then we can introduce a weighting matrix $\mathbf{W_m}$ that represents our a priori information. So the eq. 2.7 becomes:

$$\mathbf{L} = (\mathbf{m}-\mathbf{m_0})^{\mathbf{T}}\mathbf{W_m}(\mathbf{m}-\mathbf{m_0}) \qquad \textbf{(2.8)}$$

By suitably choosing the a priori model vector $\mathbf{m_0}$ and the weighting matrix $\mathbf{W_m}$ we can quantify a wide variety of measures of simplicity.

Weighted measures of the prediction error can also be useful. Frequently some

observations are made with more accuracy than others. In this case one would like the prediction error e_i, of the more accurate observations to have a greater weight in the quantification of the overall error E than the inaccurate observations. To accomplish this weighting, we define a generalized prediction error and the eq. 2.3 becomes:

$$\mathbf{E} = \mathbf{e}^{\mathbf{T}}\mathbf{W}_{\mathbf{d}}\mathbf{e} \qquad (\mathbf{2.9})$$

where the matrix $\mathbf{W_d}$ defines the relative contribution of each individual error to the total prediction error (Menke, 1989).
Now we can define the *weighted least squares solution*:

$$\mathbf{m} = \left[\mathbf{A}^{\mathbf{T}}\mathbf{W}_{\mathbf{d}}\mathbf{A}^{\mathbf{T}}\right]^{-1}\mathbf{A}^{\mathbf{T}}\mathbf{W}_{\mathbf{d}}\mathbf{d} \qquad (\mathbf{2.10})$$

and the *weighted minimum length solution*:

$$\mathbf{m} = \mathbf{m}_{\mathbf{0}} + \mathbf{W}_{\mathbf{m}}^{-1}\mathbf{A}^{\mathbf{T}}\left[\mathbf{A}\mathbf{W}_{\mathbf{m}}^{-1}\mathbf{A}^{\mathbf{T}}\right]^{-1}\left[\mathbf{d} - \mathbf{A}\mathbf{m}_{\mathbf{0}}\right] \qquad (\mathbf{2.11})$$

If the equation **Am = d** is slightly underdetermined, it can often be solved by minimizing a combination of prediction error (E) and solution length (L), ($E+\mu^2 L$).
The damping parameter μ is chosen to yield a solution that has a reasonably small prediction error.
The estimate of the solution is called weighted dumped least squares solution:

$$\mathbf{m} = \mathbf{m}_{\mathbf{0}} + \left[\mathbf{A}^{\mathbf{T}}\mathbf{W}_{\mathbf{d}}\mathbf{A} + \mu^{2}\mathbf{W}_{\mathbf{m}}\right]^{-1}\mathbf{A}^{\mathbf{T}}\mathbf{W}_{\mathbf{d}}\left[\mathbf{d} - \mathbf{A}\mathbf{m}_{\mathbf{0}}\right] \qquad (\mathbf{2.12})$$

which is equivalent to

$$\mathbf{m} = \mathbf{m}_{\mathbf{0}} + \mathbf{W}_{\mathbf{m}}^{-1}\mathbf{A}^{\mathbf{T}}\left[\mathbf{A}\mathbf{W}_{\mathbf{m}}^{-1}\mathbf{A}^{\mathbf{T}} + \mu^{2}\mathbf{W}_{\mathbf{d}}^{-1}\right]\left[\mathbf{d} - \mathbf{A}\mathbf{m}_{\mathbf{0}}\right] \qquad (\mathbf{2.13})$$

2.4. The problem of minimum length solution: depth-weighting fuction

As we have just said in the previous paragraph, the minimum length solution can be defined as the solution for the underdetermined problem. This hypothesis on the solution is the first and the most common a priori information that can be used and in fact all three algorithm studied use this type of constraint.

This kind of minimization, without other constraints, provides solutions with model parameter values as close as possible to zero. Then, because the kernel decays with distance, the minimum length solution will be always concentrated near the surface.

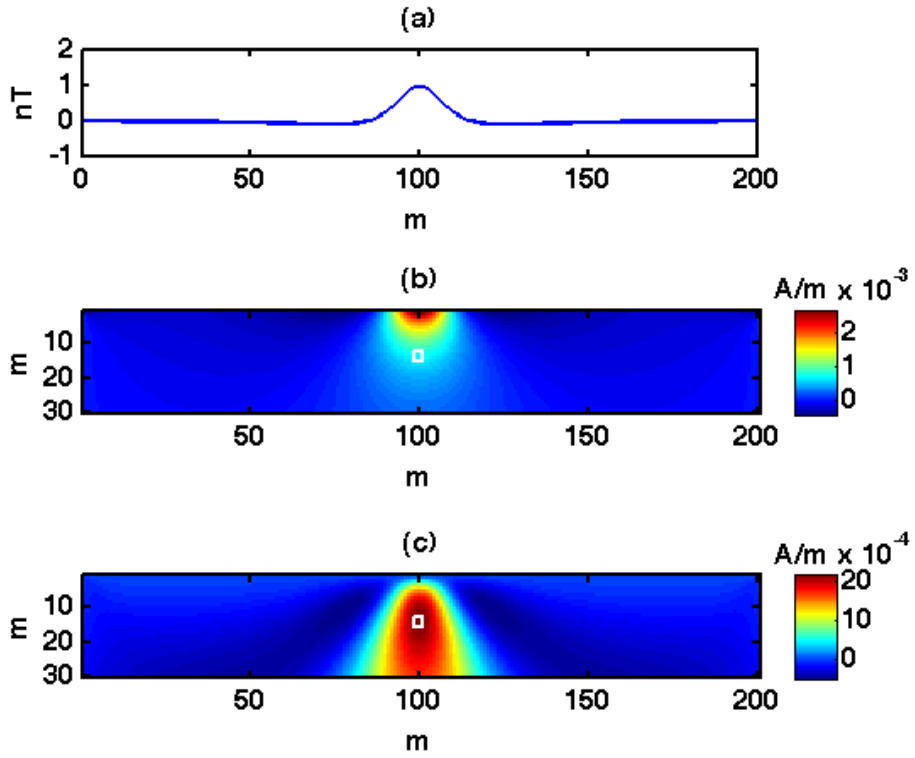

Figure 2.1 – 2D magnetization distribution (b) from minimum lenght inversion versus 2D magnetization distribution (c) from inversion with depth-weighting factor equal to 2. Both results are obtained inverting the magnetic anomaly in (a) generated by an infinite dipoles line placed at 15 m depth with unitary vertical magnetization.

In Fig. 2.1 we show a simple example of minimum length inversion of a magnetic field (Fig. 2.1a) generated by a synthetic model composed by an infinite dipoles line at x = 100m, and z = 15 m, with 1A/m magnetization. The 3D source domain was discretized with 200x30 cells, each sized 1x1 m^2. We assumed a vertical direction for both the inducing field and the magnetization vector.

The minimum length solution is shown in Fig. 2.1b and, as predicted above, the density distribution is concentrate near the surface.

This kind of density distribution does not depend on the characteristics of the observed data, but is a direct consequence of the supplied a priori information.

To avoid this too strong influence of the minimum length hypothesis, we need to introduce more a priori information. Li and Oldenburg (1996) were the first

that studied this problem and introduced a *depth-weighting function* able to counteract the natural decay of the kernel in **A**:

$$w_z = \frac{1}{(z + z_0)^{\beta}} \qquad \textbf{(2.14)}$$

where z is the depth of each layer in the 3D model and the value of z_0 depends upon the observation height and cell size (Oldenburg and Li, 2005). Li and Oldenburg propose to use for β a value equal to 3 in the magnetic case (Li and Oldenburg, 1996) and equal to 2 in the gravity case (Li and Oldenburg, 1998), assuming 3 and 2 as the rate decay of the magnetic or gravity field of a single, small, cubic cell.
Oldenburg and Li (2005) later suggested that the exponent value used in a particular inversion could be chosen, by finding the best performance of different exponent values applied to trial inversions of synthetic data from forward models similar to the expected solution.
In Fig. 2.1c we show the solution obtained using the depth-weighting function (eq. 3.1): the depth of the center is now correctly estimated.

Cella et al. (2012) showed instead that the appropriate value of β must be related to N, the structural index of the source (Table 1), rather than to the power-law decay of the field generated by a single cell.

Source	N (grav)	N (mag)
Point mass or dipole sources, spheres	2+k	3+k
Line or masses of dipols, infinite cylinder	1+k	2+k
Semi-infinite plane, thin dike, sill	0+k	1+k
Contact	-1+k	0+k

Table 1 – Structural Index (k = order of differentiation)

The structural index may be, in turn, estimated with standard methods such as Euler Deconvolution or the study of the scaling function (Fedi, 2007; Florio et al., 2009; Barbosa et al., 1999; Fedi and Florio, 2006). In chapter 3 we will see in detail how to estimate the structural index from the scaling function and how it is connected to the DEXP imaging method.

2.5. Inhomogeneous depth-weighting

Cella and Fedi (2012) showed that to obtain a correct estimate of depth to source in the inversion of undetermined problems it is necessary to use a depth-weighting function as proposed by Li and Oldenburg (1996, 1998) with an exponent β equal to the correct structural index (N) of the source.

We will now analyse the case of a field generated by sources with different structural indexes. This is a very important case, because it is the most common situation in real data. In this case, there is not a unique value for β allowing us to obtain a correct depth estimation for all sources.
The results are computed using the inversion algorithm from Li and Oldenburg (2003), which will be described in more details in paragraph 2.6.

In Fig. 2.2a a simple two source magnetic synthetic field is shown. The two sources are a infinite dipoles line (N=2), at x = 70 m and z = 15 m, with 1.5 A/m intensity of magnetization and a vertical dyke (N=1) centered at x = 130m and z = 15 m (top of dyke) with with 0.5 A/m intensity of magnetization. The 2D source domain was discretized as 200x30 cells, each sized 1x1 m^2.
The correct value to use as depth-weighting exponent β is 2 for the dipoles line source and 1 for the dyke.
The inversion solution obtained using β =1 is shown in Fig. 2.2b while setting β =2 we obtain the result in Fig. 2.2c. Using β =2 we correctly estimate the dipoles line depth, but the depth to top of the dyke is too deep and the results overestimated. Vice versa, using β =1 a correct estimate of the depth to the top of the dyke is obtained, but the depth of the dipoles line is too shallow m and the results underestimated.

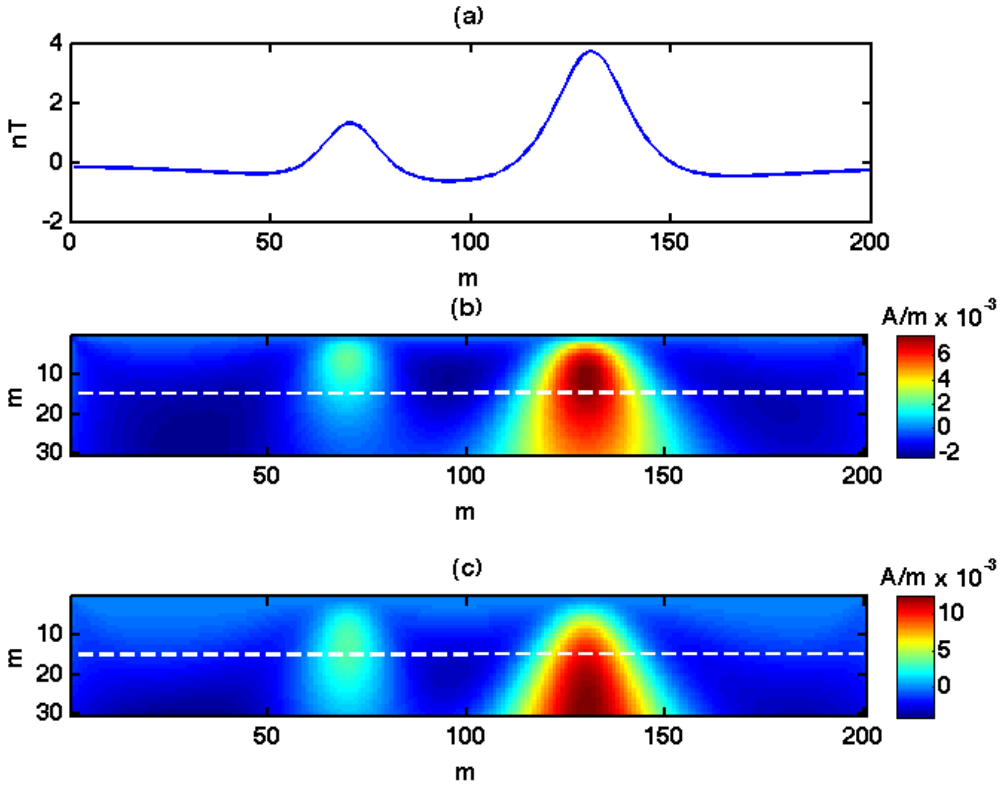

Figure 2.2 - 2D magnetization distribution (b) from inversion with depth-weighting factor equal to 1 versus 2D magnetization distribution (c) from inversion with depth-weighting factor equal to 2. Both results are obtained inverting the magnetic anomaly in (a) generated by an infinite dipoles line placed at 15 m depth and a dike with top at 15 m depth, both with unitary vertical magnetization.

To solve this problem different approaches could be used:

- ***use of an average value of β (=N);***

If the difference of the structural indices is not very big, we can assign to ***β*** the average value of the estimated structural indices, N_{AV}. For example we can invert the magnetic anomaly in Figure 2.2a using an average value of N_{AV}=1.5 between 2 and 1. By this approach the depth to sources are about -5 m and +5 m different from the depths (white dashed line) of the dipoles line and the dike respectively, then the depth is correctly estimated for both sources simultaneously (Figure 2.3).

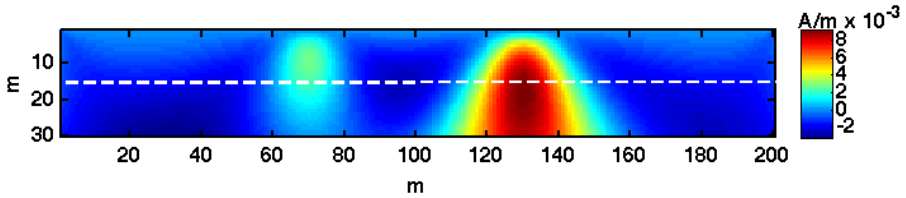

Figure 2.3 - 2D magnetization distribution (b) from inversion of the magnetic anomaly in Fig. 2.2a with a medium depth-weighting factor between 1 and 2. The dashed white line marks the depth of the sources (depth of the dipoles line and top of the dike).

- ***perform distinct inversions using different depth-weighting functions, one for each source with different N;***

If the difference of structural indices is greater than previous example, to limit the errors it is more convenient to perform distinct inversions using different values for the depth-weighting exponents and during the interpretation phase to consider as a valid solution only the portion of the model inverted with an exponent value consistent with the local structural index. This is basically the case we have already shown in Figure 2.2: so one should chose inversion result (b) for the field generated by a dike and inversion result (c) for the field generated by the dipoles line.

- **use of an inhomogeneous depth-weighting function that incorporates different values of N**

The *depth-weighting* introduced by Li and Oldenburg (1996, 1998), allow us to use a single value of exponent β, constant in the source volume. We can also set up an inhomogeneous depth-weighting function, in which we can introduce different values of β in different portions of model:

$$w(x,y,z) = \frac{1}{(z)^{\beta(x,y,z)/2}} \qquad \textbf{(2.15)}$$

For example if we consider again the synthetic field generated by a dipoles line and dyke (Fig. 2.2a), we could build a depth-weighting function with an exponent β that changes from 2 to 1 within the model.
There may be cases in which this approach does not work very well, for example when the sources are too close to each other. In this case one could build an inhomogeneous depth-weighting function with a smooth variation both in the horizontal and in the vertical directions between the ideal depth-weighting factors of the two sources.

Following Cella and Fedi (2012), who showed that it is necessary to use a depth-weighting function with an exponent β equal to the correct structural index (N) of the source, we will explore the possibility of extimating the structural index of a source as a function N(x,z) that is variable both in the horizontal and in the vertical direction. This is part of the integrated approach we will deal with in Chapter 4.

2.6. Li and Oldenburg algorithm

The algorithm we will use for all the inversion performed in this work is the Li and Oldenburg (2003) algorithm, which allows solving underdetermined problems, with the number of cells significantly larger than the amount of available data. The related objective function is able to built many different solution models that generate practically the same data. This goal is reached using appropriate weighting functions whose parameters are empirically selected, based on numerical modeling and qualitative analysis of typical gravity or magnetic anomalies.

The solution is obtained by the following minimization problem (Oldenburg and Li, 2005):

$$\begin{aligned} &\text{minimize } \varphi = \varphi_d + \mu\varphi_m \\ &\text{subject to } m_{min} \leq \mathbf{m} \leq m_{max} \end{aligned} \qquad (\mathbf{2.16})$$

where m_{min} and m_{max} are vectors containing the lower and upper bounds on the model values, and **m** is the vector containing model values.

The prior information that this algorithm allow to introduce might be:

(a) knowledge of a background or reference model and
(b) a general assumption that the structures should be smooth or that they have sharp edges (Oldenburg and Li, 2005).

The algorithm uses the primal logarithmic barrier method with the conjugate gradient technique (CG) as the central solver. In the logarithmic barrier method, the bound constraints are implemented as a logarithmic barrier term.

The objective function is given by (Gill et al. 1991):

$$\varphi(\lambda) = \varphi_d + \mu\varphi_m - 2\lambda\sum_{j=1}^{M}\left[\ln\left(m_j - m_j^{\min}\right) + \ln\left(m_j - m_j^{\min}\right)\right] \qquad (2.17)$$

where μ is the regularization parameter, λ is the barrier parameter.
φ_d is the weighted data misfit and φm is the model objective function. The weighted data misfit is given by:

$$\phi_d = \left\|\mathbf{W_d}\left(\mathbf{d} - \mathbf{d_{obs}}\right)\right\|^2 \qquad (2.18)$$

where **d** are the predicted data, $\mathbf{d}_{obs}$ are the observed data-vector and $\mathbf{W}_d$ is the inverse data covariance matrix.

$$\begin{cases} \varphi_m(m) = \alpha_s \int_{vol} w_s w^2(z)(\mathbf{m} - \mathbf{m_0})^2 dv + a_x \int_{vol} w_x \left(\frac{\partial w(z)(\mathbf{m} - \mathbf{m_0})}{\partial x}\right)^2 dv + \\ a_y \int_{vol} w_y \left(\frac{\partial w(z)(\mathbf{m} - \mathbf{m_0})}{\partial y}\right)^2 dv + a_z \int_{vol} w_z \left(\frac{\partial w(z)(\mathbf{m} - \mathbf{m_0})}{\partial z}\right)^2 dv \end{cases} \qquad (2.19)$$

where **m** is the unknown model, $\mathbf{m}_0$ is a reference model and w(z) is the depthweighting function (equation 2.14):

$$w_z = \frac{1}{(z + z_0)^{\beta}}$$

Li and Oldenburg propose to use for β a value equal to 3 in the magnetic case (Li and Oldenburg, 1996) and equal to 2 in the gravity case (Li and Oldenburg, 1998), assuming these values as corresponding with the rate decay with distance of a single small cubic cell in magnetic and gravity field respectively.
As explained in paragraph 2.4 the purpose of this function is to counteract the geometrical decay of the kernel with the distance from the observation location so that the recovered susceptibility is not concentrated near the observation locations.
The terms w_s, w_x, w_y, w_z are spatially dependent weighting functions to input additional prior information about density or susceptibility model. In particular The weights w_x,w_y,w_z, with or without a reference model, control the degree of smoothness of the solution along the three directions (Oldenburg and Li, 2005); finally α_s, α_x, α_y and α_z are coefficients controlling the importance of each term.
The logarithmic barrier term forms a barrier along the boundary of the feasible domain and prevents the minimization from crossing over to the infeasible region.

The method solves a sequence of nonlinear minimizations with decreasing λ and, as λ approaches zero, the sequence of solutions approaches the solution of eq (2.17).

Further details on how a numerical solution is obtained discretizing the model objective function can be found in Oldenburg and Li (1994).

Instead of carrying out the full minimization at each iteration, it is common to take a Newton step for each value of λ and adjust the step length so that the updated model remains positive (Gill et al. 1991). The step length is also used to determine the decreased value of the barrier parameter λ for the next iteration (Li and Oldenburg, 2003).

The barrier iteration continues until the value of λ is sufficiently small such that barrier term has a negligible contribution to the total objective function (eq. 2.18) and the iteration stops when the objective function is changing less than 1 per cent.

3. Imaging techniques for potential fields data: the DEXP method

The Depth from Extreme Points method (DEXP, Fedi et al., 2007) is based on the explicit scaling of the upward continued field by a power law of the continuation height. The type of power law is either assumed or determined directly from the field data; this means that DEXP, unlike the inversion methods, does not require a priori information about the source of the anomaly.
The method allows to obtain information about the position of the source, and its extension and shape.
The DEXP method is a very stable method respect to noise and can be applied to the field and his derivatives through the following steps.

- *Continuation of the field*
  Measured data has to be upward continued to create a 3D data volume; for the scopes of this work, only two-dimensional cases have been examined; so potential field data profiles have been upward continued using 1D upward-continuation algorithms to obtain a section.
- *Scaling the field*
  The upward continued field is then scaled according to specific power laws. So, a 3D field originated by a source at $\mathbf{r}_0$, expressed by a function $f(\mathbf{r}\text{-}\mathbf{r}_0)$, is then scaled to have $W(\mathbf{r}\text{-}\mathbf{r}_0)$.
- Estimating the source depth
  the source depth is then determined searching for the extreme points $\mathbf{r}(x,y,z)$ of $W(\mathbf{r}\text{-}\mathbf{r}_0)$. As will be shown the points $r(x,y,z)$ are symmetrical to $\mathbf{r}_0(x_0,y_0,z_0)$.
- Compute the excess mass
  the excess mass (or excess dipole moment intensity for the magnetic field) can be also computed, from the value of the scaled potential field at the extreme points.

The final result will then be a depth distribution of extreme points, excess mass values, and scaling exponents.
In this work I will pay particular attention to the scaling exponent and their dependence on the distance from the source both in the vertical and horizontal directions.

3.1. Theory of the DEXP method

In this paragraph I will breafly show thetheoretical background of the DEXP method, following the demonstration given by Fedi (2007) for the gravity field of a pole source.
The gravity field $f_1(\mathbf{r})$ due to an homogeneous sphere at $\mathbf{r}_0(x_0,y_0,z_0)$ with density M=1 and normalized by the gravity constant k, can be expressed as:

$$f_1(\mathbf{r}) = \frac{(z - z_0)}{\left\|\mathbf{r} - \mathbf{r}_0\right\|_2^3} \qquad (\mathbf{3.1})$$

If the source is at $r_0(0,0,z_0)$ and the field is measured at $x=x_0$, $y=y_0$ we have:

$$f_1(z) = \frac{1}{(z - z_0)^2} \qquad (\mathbf{3.2})$$

The scaling function can be defined as the derivative of the logarithm of the field f with respect to log (z):

$$\tau(z) = \frac{\partial \log\left[f_1(z)\right]}{\partial \log(z)} \qquad (\mathbf{3.3})$$

For the above mentioned example of the gravity field, the scaling function τ_1 is:

$$\tau_1(z) = -\frac{2z}{z - z_0} \qquad (\mathbf{3.4})$$

From the equation 3.4 we can see that $\tau_1(z)$ is singular at $z=z_0$ in the source region , but at $z=-z_0$ we have:

$$\tau_1(-z_0) = -1 \qquad (\mathbf{3.5})$$

it follows that

$$\left.\frac{\partial\left\{\log\left[f_1(z)\right] + \log(z)\right\}}{\partial(z)}\right|_{z-z_0} = 0 \qquad (\mathbf{3.6})$$

that can be written also as:

$$\left.\frac{\partial z f_1}{\partial z}\right|_{z-z_0} = 0 \qquad (\mathbf{3.7})$$

As we can see from this equation, the function zf_1 has a maximum at $z=-z_0$. This means that, scaling the gravity field with a power law of the altitude z and exponent equal to 1, we can have a scaled gravity field, W_g

$$W_g = f_1 z \qquad (3.8)$$

having a maximum at $x=x_0$, $y=y_0$ and $z=-z_0$. Obviously, the maximum is due to the fact that we have assumed a positive density contrast. If we choose a negative density contrast we will have a minimum at the point **r**($x=x_0$, $y=y_0$, $z=-z_0$). Moreover, instead to express the function W_g as function of **r**, we can express W_g as function of (x_0,y_0,z_0).

We can generalize the scaling function formula to any *p*-th order vertical derivative of the field f_p, and to any kind of homogeneous source; in fact, starting from the *p*-th order derivative of the gravity field, of homogeneity degree *n*,

$$f_p(x = x_0, y = y_0, z) = \frac{1}{(z - z_0)^{N+p}} \qquad (3.9)$$

Where $N=-n$, we get

$$\tau_p \frac{\partial \log\left[f_p(z)\right]}{\partial \log(z)} = -\frac{(N+p)z}{z - z_0} \qquad (3.10)$$

At $z=-z_0$ we will have:

$$\tau_p(-z_0) = -\frac{(N+p)}{2} \qquad (3.11)$$

Hence, the general scaled function, W_p, having as extreme point the point $x=x_0$, $y=y_0$ and $z=-z_0$, can be expressed as:

$$W_p = f_p z^{\frac{N+p}{z}} \qquad (3.12)$$

3.2. DEXP of simple sources

We have described the DEXP transform for the field and its derivatives of a simple pole source. Obviously real sources generate a field that cannot be explained by something like a simple pole source, unless the field is measured at a great distance. So we could define real soruces as source distributions within finite volumes with arbitrary shapes (Fedi, 2007).

But, in the majority of the cases, the source complexity can be semplified to semi-infinite volume-less shapes. For example we can see pipes, ridges, valleys, tunnels, volcanic necks as infinite cylinders.

These simple shape bodies are generally defined as one-point sources, meaning that we need the coordinates of just one singular point, i.e. the center or the edge, to define them (Stavrev, 1997; Fedi, 2007).
The DEXP transformation properties for most one point sources have been widely defined by Fedi (2007) by the same approach used to compute the DEXP transformation for a pole-source.

The following table displays the scaling exponent for the most common one point sources, adjacent to the source parameter involved in the well-known theory of Euler deconvolution (Reid et al., 1990, Stavrev, 1997), called the Structural Index both for gravity and magnetic anomalies.

	n = 1		n = 2	
Source	N	SI	N	SI
Point mass or dipole sources, spheres	1	2	1.5	3
Line or masses of dipols, infinite horizontal and vertical cylinder, thin bottomless prism	0.5	1	1	2
Semi-infinite plane, thin dike, sill	0	0	0.5	1

Table 3.1 - Scaling exponents ans structural indexes for the most common one point sources.

It is easy to note that the scaling exponent and the structural index for magnetic anomalies are connected by a clear relationship:

$$S_n = 2\,N_n \qquad \textbf{(3.13)}$$

since both SI and N are source parameters reflecting the type of source and the falloff rate of their fields.
In paragraph 2.4 we have mentioned that the structural index plays an important role in potential field data inversion because it allows to choose the appropriate value of the depth-weighting function exponent β, rather than to the power-law decay of the field generated by a single cell (Fedi and Cella, 2012). We will focus now the attention on the scaling exponent of the DEXP function and how it can be assessed directly from the data.

3.3. Determining the scaling exponent from the data

In the introduction we said that the type of power law for scaling the data is either assumed or determined directly from the field data itself; among the possible approaches to get the scaling esponent estimate from data (see Fedi, 2007) I will breafly describe the criterion of DEXP scaling-function intercept.

Starting from equation 3.10, we can arrange again the scaling function putting z=1/q:

$$\tau_p(q) = -\frac{(N+p)}{1-z_0 q} \qquad \textbf{(3.14)}$$

so, as q tends to 0 we have:

$$\lim_{q\to 0} \tau_p = -N + p \qquad \textbf{(3.15)}$$

Hence, the intercept of τ_p versus q will give an estimate of the structural index N plus the order of differentiation, and as we can note the estimation of N does not depend on the vertical position of the source z_0.

The DEXP multiscale approach will be analysed in more detail in the following chapter for simple and complex sources; for further technical details and examples please refer to Fedi (2007).

4. Potential fields data inversion constrained by multi-scale imaging information

One of the principal difficulties with the inversion of the potential field data is the inherent non-uniqueness. In fact, by Gauss' theorem we know that there are infinitely many equivalent source distributions that can produce a measured field (Blakely, 1996).

When the number of model parameters M is greater than the number of observations N, a unique solution for the inverse problem does not exist (underdetermined problem). This denotes an algebraic ambiguity and represents the most common problem in geophysics inversion. Thus we have two causes of ambiguity, both implying that there are infinitely many models that will fit the data to the same degree.

To solve an undetermined problem and obtain a unique solution we need to add a priori information. Prior information takes numerous forms (geological, geophysical or mathematical) and a good inversion algorithm is able to incorporate this information into the inversion.

In the following paragraphs I will show how information coming from imaging methods can be successfully used as constrain for inversion.

Imaging techniques can provide a result similar to inversion algorithms, even if they do not incorporate yet compactiveness or non-negativity constraints; on the other hand these techniques are non-iterative, meaning less computational time respect to the inversion algorithms, moreover they are stable, as a consequence of the properties of upward continuation, that acts like a low pass filter with an intrinsic attenuation of the field when the depth increase.

4.1. Integrating inversion algorithms and DEXP information

As already mentioned in chapter 2, inversion algorithms allow reconstructing the distribution of some of the rocks' physical properties (for example density or magnetization intensity, if talking about potential fields) in an indirect way, that is starting directly from the measured geophysical data.

The parameterization of the solution model space assumes fundamental importance both in the inversion and imaging algorithms, as it strongly

influence the way the solution will be build and the type of constraints it will incorporate.

This time we could start from Fredholm integral equations to describe the inverse gravity and magnetic problems, which are notoriously ill posed.

For example, the inverse geomagnetic problem has the following formulation (Fedi et al, 2005):

$$\int_{\Omega} K(\mathbf{r},\mathbf{r}_0) M(\mathbf{r}_0) d^3\mathbf{r}_0 = \Delta T(\mathbf{r}) \qquad (\mathbf{4.1})$$

where $\Delta T(\mathbf{r})$ is the magnetic field measured at ($\mathbf{r}$) and $M(\mathbf{r}_0)$ is the unknown magnetization distribution; the volume integral is calculated over Ω; while the kernel $K(\mathbf{r}, \mathbf{r}_0)$ inside the integral equation represent the field measure at a distance $\mathbf{r}$ from the centre of a magnetic dipole with intensity of magnetization equal to 1 and placed in $\mathbf{r}_0$.
If we assume for simplicity, that the source magnetization direction is parallel to the main magnetic field, and that both are vertical, so that the magnetic anomaly is reduced to the pole, than the kernel K can be rewritten as:

$$K(\mathbf{r},\mathbf{r}_0) = \frac{3(z-z_0)^2}{\|\mathbf{r}-\mathbf{r}_0\|_2^5} - \frac{1}{\|\mathbf{r}-\mathbf{r}_0\|_2^3} \qquad (\mathbf{4.2})$$

where z and z_0 are the vertical components of $\mathbf{r}$ and $\mathbf{r}_0$, while $\|\bullet\|_2$ is the Euclidean norm of a vector.
If we discretize the source volume Ω into N cells, following an $N_x \times N_y \times N_z$ grid, ad we assume that each cell Ω_j has a constant magnetization M_j, we can write the kernel K as a numeric matrix expression, solving equation (4.2) for each cell.
For the geomagnetic inverse problem we will have $ex \times ey$ equations (one for each measured data location) and each equation will have $N_x \times N_y \times N_z$ unknowns. That is a system of $P \times N$ linear equations:

$$\mathbf{K\,m = d} \qquad \mathbf{(4.3)}$$

where P is the number of measured and $N = N_x \times N_y \times N_z$ are the unknowns. The coefficients matrix **K** is formed by the following elements:

$$K_{ij} = \int_{\Omega_j} K(\mathbf{r}, \mathbf{r}_0) d^3\mathbf{r}_0 \qquad i=1, \ldots, P, \qquad j=1, \ldots, N; \qquad (\mathbf{4.4})$$

the data vector **d** is formed by P measurements $\Delta(\mathbf{r}_i)$, while the vector **m** is formed by *N* values of magnetization M_j . Each of the element of the K_{ij} can be calculated following equation 9.19 in Blakely (1996).

We showed in paragraph 2.4 that if the number of unknowns *N* is greater than the number of data *P*, the system of equations has infinite solutions and is called *undetermined*.

Among the infinite number of possible solutions the simplest is the *minimum length* one, which minimizes the euclidean norm of the solution; this means that the magnetization solution assumes the lowest possible value. This type of solution will necessarily be shallow, since newtonian potentials and their partial derivatives follow a decay law which is the inverse of the distance from the source.

The *minimum length* solution can be expressed also in matrix form following Menke (1989):

$$\mathbf{m} = \mathbf{K}^T(\mathbf{K}\mathbf{K}^T)^{-1}\mathbf{d} \qquad (\mathbf{4.5})$$

Cribb (1976) showed that, in the frequency domain, the solution to the magnetic continuous undetermined problem assumes the followinf formulation:

$$F[\mathbf{m}_i] = \frac{4}{V(\mathbf{k})} e^{-|\mathbf{k}|h_i} F[\mathbf{d}] \qquad i=1,\ldots, L \qquad (\mathbf{4.6})$$

where *F* denotes the Fourier transform operation, *L* is the number of layers of the solution space, $\mathbf{m}_i$ and h_i are the magnetization vector and the depth of the i^{th} layer of the model space, **k** is the wave vector with components k_x, k_y, **f** e **t** are versors placed respectively in the direction of the inducing field and of the total magnetization, both of them do not vary in the investigated region; lastly $V(\mathbf{k})$ can be expressed as:

$$V(\mathbf{k}) = \frac{(\mathbf{f}\cdot\mathbf{k})(\mathbf{t}\cdot\mathbf{k})}{\mathbf{k}^2} \qquad (\mathbf{4.7})$$

The solution in the frequency domain (**4.6**) shows an interesting relation between the computed magnetization distribution $\mathbf{m}_i$ and the upward continued magnetic field at an height equal to the depth of the h_i level of the source model; indeed, $\exp(-|\mathbf{k}|h_i)$ denotes the upward continuation operator expression in the frequency domain (Blakely, 1996).

Similarly, *imaging* methods allow obtaining a density (or magnetization intensity) 3D distribution, or to have an *image* of a quantity related to these distributions, wihout having to go through inversion alghorithms.

Among the available *imaging* methods, the *multi-scale* ones have the advantage of being capable of studying the complexity of the Earth System varying the survey scale. The interest of the scientific community into the multi-scale methods applied to potential field data has rised during the last ten years, as a large amount of published research shows (Fedi et al., 2005; Fedi et al., 2010; Fedi, 2007; Fedi e Florio, 2006; Fedi e Pilkington, 2012; Fedi e Abbas, 2013). The immediacy of the application of multi-scale methods on potential field data comes from the evidence that these fields can be considered as the sum of the effects given by different sources placed at differents depths. How these effects superimpose to each other is a complexity to solve analysing the contribute of each source at a different scale.

As alreasy showed in detail in chapter **3**, the DEXP method (Fedi, 2007), allows to have an estimate of the source body depth, density (in the gravity case, or magnetization intensity in the magnetic case) from maximum (or minimum) points of its field scaled according to a specific power law of the height of measurement.

The DEXP approach suggests one more interesting connection with equation (**4.6**) since it relates the upward continued field to some of the properties of its source, for example the Structural Index SI (a parameter related to the source shape, see table xx) or the depth:

$$\mathbf{\Omega}(\mathbf{r},z_i) = |z_i|^{N/2}\, d(\mathbf{r},z_i) \qquad i = 1,...,L \qquad (\mathbf{4.8})$$

where $\Omega(\mathbf{r},z_i)$ is the DEXP scaled field at height z_i, $\mathbf{r}$ is the vector related to the coordinates $[x,y]$, $d(\mathbf{r},z_i)$ is the field d upward continued at a height z_i and $|z_i|^{N/2}$ is the scale low, with the exponen $N/2$ depending on the source.

The depth of the source and the excess mass (or magnetization intensity) can be derived for each of the source looking at the position of the maxima (or minima) of the transformed field Ω (Fedi, 2007).

The DEXP transform can also be expressed in the frequency domain as follows:

$$F[\mathbf{\Omega}_i] = h_i^{N/2} e^{-|\mathbf{k}|h_i} F[\mathbf{d}] \qquad i = 1,..., L \qquad (\mathbf{4.9})$$

Where $\mathbf{\Omega}_i$ is the DEXP transformed field at a certain height z_i=-h_i.
Equations (**4.6**) e (**4.9**) can be combined together to get the following result:

$$F[\mathbf{\Omega}_i] = V(\mathbf{k}) \frac{h_i^{N/2}}{4} F[\mathbf{m}_i] \qquad i = 1,..., L \qquad (\mathbf{4.10})$$

In the magnetic case, and a similar expression in the gravimetric case.
Equation (**4.10**) shows that the DEXP transformed field is directly connected to the magnetization model obtained from equation (**4.5**), where the solution to the continuous undetermined magnetic problem is expressed in matrix form.
The weighting function $h_i^{N/2}$ places the DEXP result at the correct depth of the source, apart from a constatnt, which gives the result the correct physical dimensions.
Figure 4.1 shows a comparison of a DEXP transformation and an inversion of the anomaly (Figure 4.1a) given by a mass line placed at 10km depth with infinite extension in the direction perpendicular to tha plane of the figure.
The coordinates of the maximum of the DEXP transformed field (Figure 4.1c) give a correct estimate of the depth source; this is the same result we can obtain from an inversion (Figure 4.1b) algorithm without fixing any further constraint apart from the *depth weigthing* function (see paragraph 2.4) whose *depth weigthing* factor has been chosen following Cella et al. (2012). The absence of other type of constraints gives both the solution a shape not exactly reliable to the source body.
The computing time is 8 seconds for DEXP e and 96 seconds for the inversion using Li and Oldenburg approach.

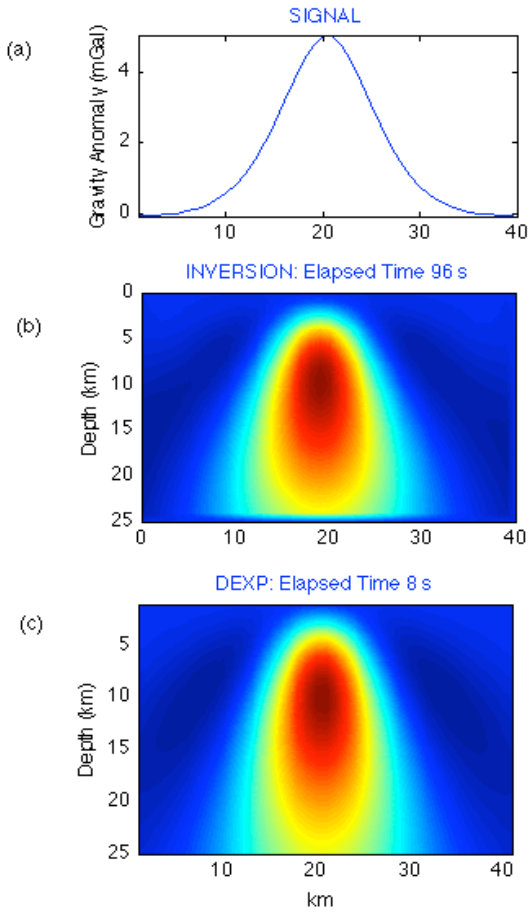

Figure 4.1 - Inversion vs DEXP transform. (a) Gravity anomaly given by a mass line placed at 10km depth with infinite extension in the direction perpendicular to tha plane of the figure. (b) Inversion of the gravity anomaly in (a), with depth-weighting factor equal to 2. (c) DEXP transforms of the field in (a).

Imaging results can be combined with inversion algorithms in different ways:

1. Source distributions can be converted into density (or magnetization intensity) and used as a-priori models for inverting or interpreting potential field data;
2. Source-related information (i.e. the Structural Index or the source depth) can be transferred into the inversion algorithms as constraints to the final solution.

To follow suggestion (1) the DEXP transformed field has to be converted in a density (or magnetization intensity) model, through equation (**4.10**), getting the following expression:

$$F[\mathbf{m}_i]h_i^{N/2} = F[\mathbf{\Omega}_i]\frac{4}{V(\mathbf{k})} \qquad (\mathbf{4.11})$$

Equation (**4.11**) show that the *minimum length* solution $\mathbf{m}_i$, when multiplied by a depth-weighting function $h_i^{N/2}$ corresponds to the DEXP transform multiplied by the constant 4/V(**k**). To validate equation (**4.11**) dimensions, the DEXP has to be converted from field units (mGal o nT) to density/magnetization intensity units (g or A/m) multiplying the result by a quantity having the same dimensions of the factor $h_i^{N/2}$, which is a length $l^{N/2}$.
Another interesting approach is the one described at point (2).

The DEXP theory has been developed for fields coming from sources with integer N index (see Table 3.1); if this theory is generalized to the family of fields with non-integer N or with N varying as the distance from the source varies (Fedi et al., 2012), then the DEXP source-related information can be used to invert the field coming from any complex source.

We have already mentioned in paragraph **3.2** that sources whose mass distribution can be concentrated in just one point (*one-point sources*), such as a mass point, a mass line, a contact, a sill, give potenatial fields, whose DEXPs allow to estimate an integer N index. For such sources N can be simply estimated for example with the criterion of DEXP scaling-function intercept (Fedi, 2007). Such approach supposes that N does not vary if the scale of study changes, so the value at the intercept can represent the real N of the source.

See for example in Figure 4.2b the magnetic anomaly generated by a line of dipoles placed at 15 m depth, the scaling function exponent exponent assumes an integer value and does not vary with the scale of study, and so consequently does the index N(z) shown in Figure 4.2a. The DEXP scaled field in Figure 4.2c has its maximum value in correspondence of the source depth.

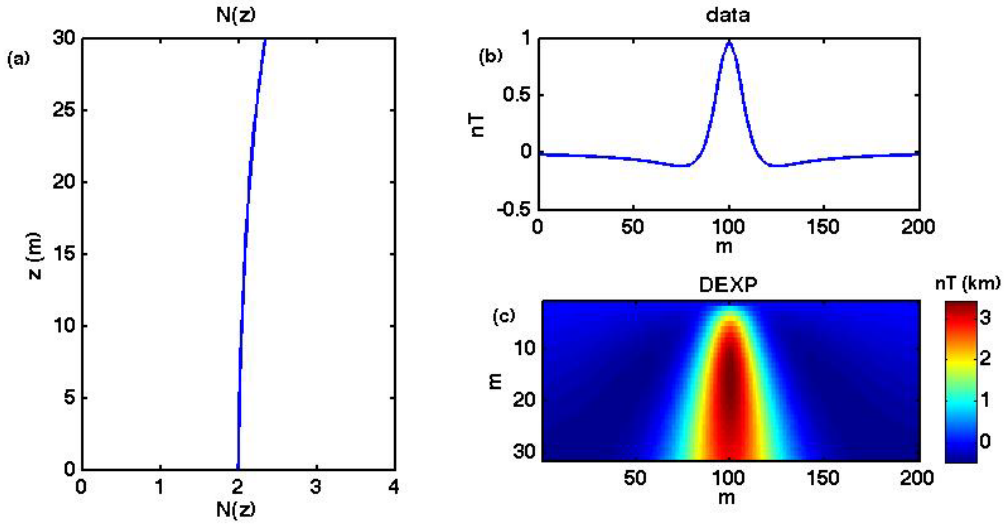

Figure 4.3 – DEXP scaled field (c) of a magnetic anomaly (b) generated by a line of dipoles placed at 15 m depth, the scaling function exponent assumes an integer value and does not vary with the scale of study, and so consequently does the index N(z) shown in (a).

If we examine the fields generated by complex sources (non one-point) the estimate of the scaling-factor N will be, first of all, a non-integer estimate, and will also be scale-variant, that is it will vary according to the field continuation height.

Fedi et al. (2012, 2015) showed that such kind of fields, called inhomogeneous, can be studied in the framework of the multiscale methods, assuming that the standard homogeneous equation can be "relaxed" to a local homogeneity equation. To define the homogeneity property in terms of local homogeneity, they follow Olmsted (1991), who distinguished between homogeneous functions and locally homogeneous func- tions, and gave an extension and converse of Euler's theorem (Eq. 15 in Fedi et al, 2015).

Instead of using the local-homogeneity equation for the fields Fedi et al. (2015) propose to use at each position the local-homogeneity equation for the scaling function. Equations 3.3 and 3.10 can be riarranged as:

$$\tau(z) = \frac{\partial \log T}{\partial \log z} = n\frac{z}{z - z_0} \qquad \textbf{(4.12)}$$

Where τ(z) is the scaling function, a dimensionless function of the altitude, which characterizes the scaling behaviour of a homogeneous field *T*; z is the altitude and z_0 is the source depth. Equation 4.12 provides a convenient tool to

study the field across scales. The main advantage of using the scaling function arises from its independency on either physical constants or density.

For a homogeneous field, the homogeneity degree n and the depth to the source z_0 may be estimated from τ in a number of ways (Fedi and Florio, 2006). For instance, altitudes and depths have an arbitrary zero-level, so that they may be rescaled by a guess depth value ζ:

$$\tau(z) = n\frac{z-\zeta}{z-z_0} \qquad \textbf{(4.13)}$$

and z_0 may be estimated as the value of $\zeta = z_0$ making τ the closest to a straight line with a zero-slope, whose intercept is n (see Fedi 2007, for additional details).
Equation 4.13 can be computed at each scale z as:

$$\tau(f) = n(z)\frac{z}{z-z_0(z)} \qquad \textbf{(4.14)}$$

where $n(z)$, $z_0(z)$ are the local homogeneity-degree and depth to the source at each scale z, while $\tau(f)$ is instead computed directly from the field at the various altitudes.

4.2. Integrated workflow

We will first examine the case of the 2D[2] magnetic anomaly given by a finite vertical cylinder, with unitary vertical magnetization, top base at 10 m and bottom base at 20 m depth, centered at x=100 m with unitary extension along the x direction, and infinite extension along the y direction, so it can be studied as a 2D source. Figure 4.4 shows the magnetic anomaly in (b), the upward continued field in (c), and the $N(z)$ index extracted along the along a vertical profile crossing the maximum of the field in (a).

[2] The two-dimensional (2D) approach assumes that the source body causing the anomaly is infinitely long parallel to the strike of the data profile direction.

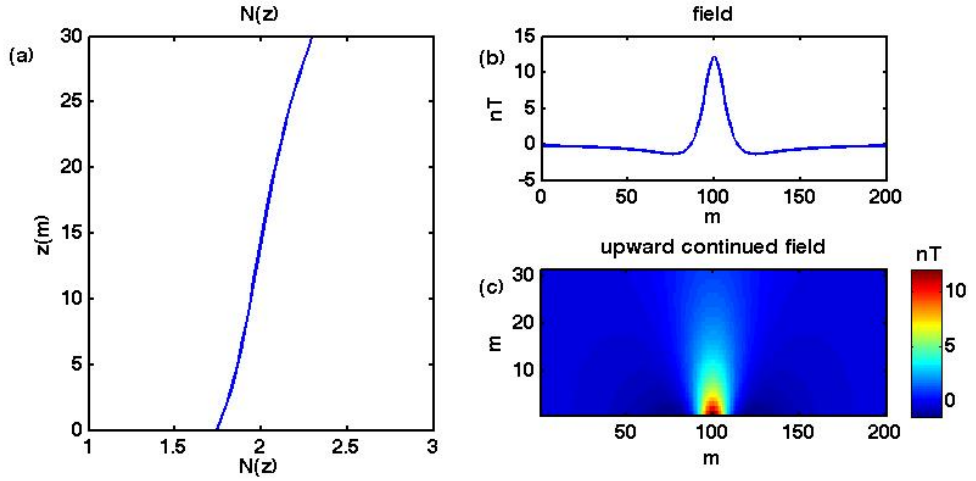

Figure 4.4 - The magnetic anomaly in (b) given by a finite vertical cylinder, with unitary vertical magnetization; the upward continued field in (c), and the N(z) index extracted along the along a vertical profile crossing the maximum of the field in (a).

The values of $N(z)$ coming from multiscale analysis can be used as weighting function rate decay in inversion algorithms, as showed by Cella and Fedi (2012), setting a weighting function which varies according to the depth of the solution model cells.

The 2D source domain was discretized with 200x30 cells, each sized 1x1 m. We assumed a vertical direction for both the inducing field and the magnetization vector.

Figure 4.5 shows the different magnetization distributions derived inverting the magnetic anomaly in Figure 4.4b using a depth-weighting factor equal to 1 (semi infinite plane (Fig. 4.5a)), 1.5 (Fig. 4.5b), 2 (infinite cylinder), variable with depth (after Fig. 4.5d). Among the results from inversion with integer depth-weighting parameters, the most reliable result seems the one obtained with N=1, while using N=1.5 or N=2 the maximum of the distribution is placed too deep if compared with the true source depth.

The inversion carried on setting a variable depth-weighting function (Fig. 4.5d), gives the most reliable distribution of the source, since the maxima of the distribution are confined in a depth range which agrees with the top and the bottom of the cylinder source (z top= 10 m and z bottom = 20 m).

From now on, the results coming from inversion with scale-variant depth-weighting factor will be compared with the results coming from inversion with depth-weighting parameter set equal to 1.

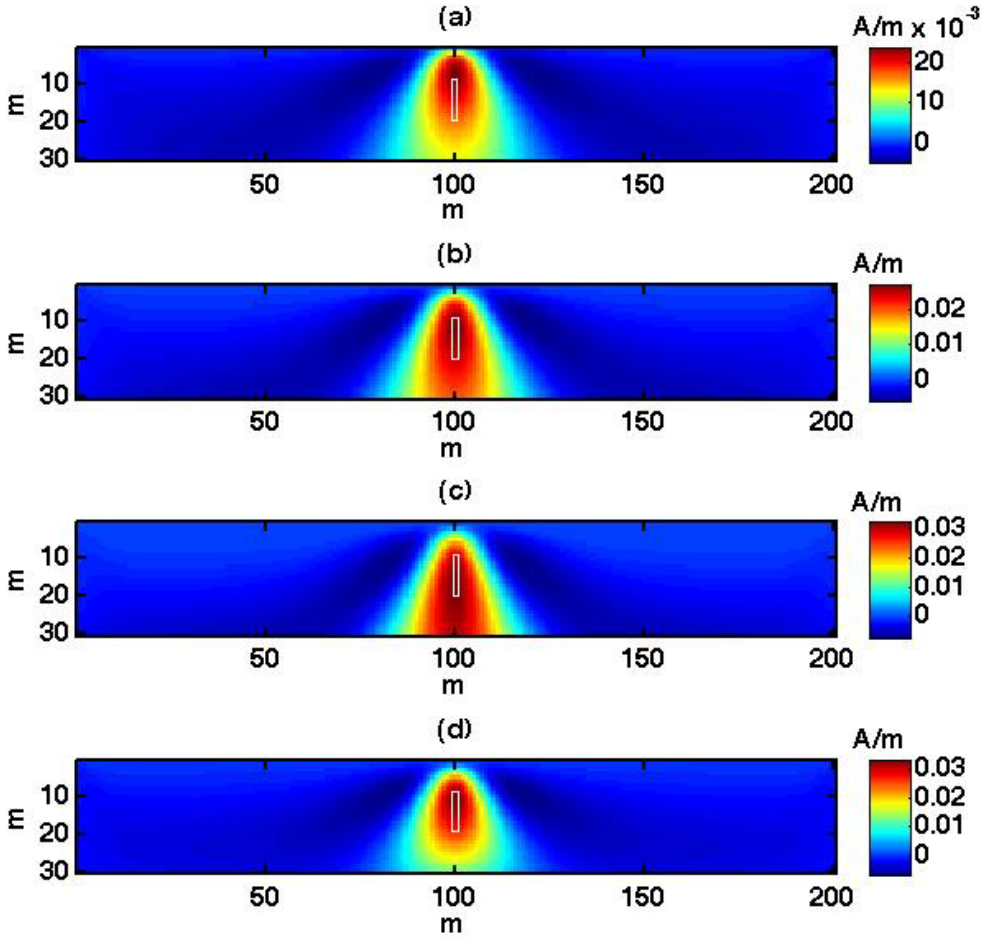

Figure 4.5 – Magnetization distribution derived inverting data in Figure 4.4b using different *depth-weighting* parameters: 1 (in panel a), 1.5 (in panel b), 2 (in panel c) and *depth-weighting* index varying with z according to Fig. 4.4a (in panel d).

The function $N(z)$ can be extracted also along along vertical profiles not crossing the maximum of the field, leading to a $N(x,z)$ function acting both in the vertical and in the horizontal direction of the source model domain.

Figure 4.6 shows the N(z) profiles extracted along different positions on the anomaly profile: the N(z) function named *ridge C* comes from a profile along the maximum of the field, the N(z) function named *ridge H* comes from location x=150 m, the N(z) function named *ridge F* comes from a location on the right boundary of the anomaly.

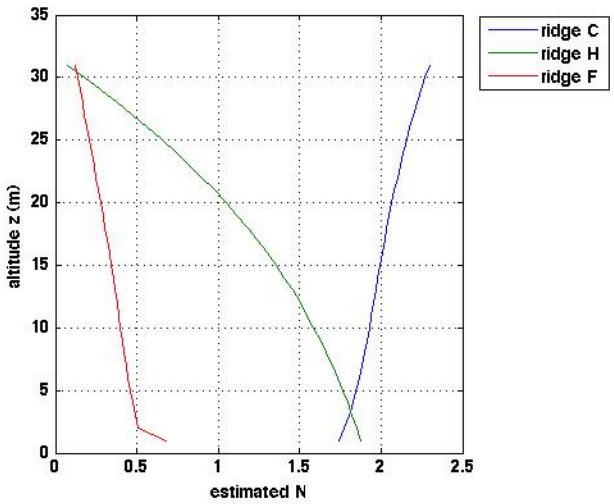

Figure 4.6 – Estimates of the N(z) function at different x location along the magnetic anomaly in Fig. 4.4b: ridge C is taken in correspondence of the centre of the anomaly; ridge H s taken at an intermediate distance from the maximum of the anomaly; ridge F is taken on the anomaly right border.

This first-pass analysis on the variability of the *N(z)* function along the profile direction shows that the N indexes are quite different if we estimate *N(z)* in the surroundings of the source or away from it. Our next goal is then to analyse the impact of this variability on the depth-weighting function.

In this testing stage, *N(z)* functions have been estimated along the profile keeping the sampling interval small, to better understand how fast it varies going aways from the field maximum. The results of the extractions all along the anomaly of Figure 4.4b are shown in picture 4.7.

Since the magnetic anomaly is symmetrical respect to the center of the profile, *N(z)* functions have been estimated along only one of the sides of the anomaly, labels from 100 to 190 denote the position of the *N(z)* along the profile (*N*(z, *x* =100 m) is taken at the centre of the profile, while *N*(z, *x* =190 m) is taken on its western border.

Figure 4.7(a) shows how *N(z)* varies gradually as the distance from the maximum of the anomaly is small; while from a certain point on, *N(z)* estimates become noisier and noisier (see Figure 4.7 (b) and (c)) and finally become regular again far away from the source.

At a first sight *N(z)* seems to vary according to the distance from the source; in particular, plotting the *N(z)* estimates vesurs the distance to the source (i.e. distance from the maximum of the field) it is possible to link the noisy behaviour of *N(z)* function with the horizontal limits of the source.

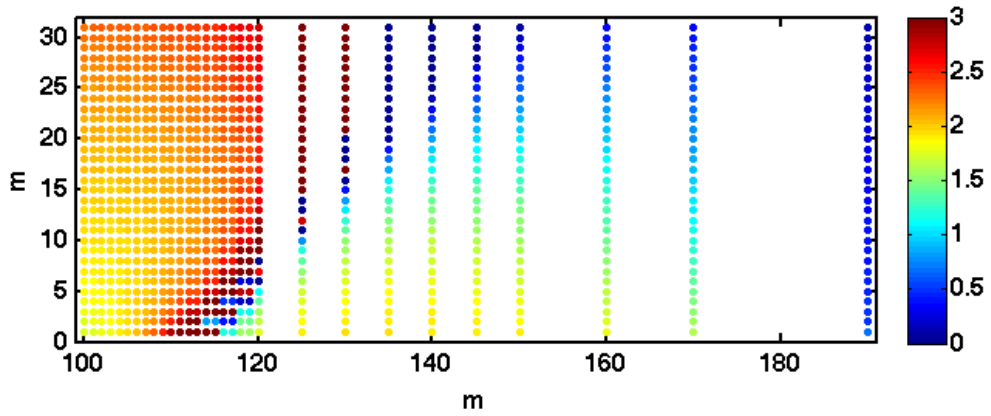

Figure 4.7 - N(z) functions estimated along the right sides of the anomaly in Fig. 4.4b; labels from 100 to 190 denote the position of the N(z) along the profile (N(z, x =100 m) is taken at the centre of the profile, while N(z, x =190 m) is taken on its western border.

From this we can infer two main areas where the *N(z)* behaviour varies homogeneously:

- a zone "inside" the source boundaries where *N(z,x)* can be sampled at regular intervals along the profile direction and then used directly to contrain the inversion
- a zone "outside the source boundaries where *N(z,x)* has a noisy shape, until it become stable again at the borders of the profile; here the *N(z,x)* sampled at the profile border can be assigned to the whole noisy zone.

The following picture compares the magnetization distributions coming from the inversion of the data shown in Figure 4.4b using a depth-weighting factor equal to 1in Figure 4.8a, variable with depth in Figure 4.8b, variable with depth and horizontal position in Figure 4.8c.

The inhomogeneous depth-weighting fuction has been derived from the *N(z)* extracted from x_n positions along the profile starting from x=100 m until x= 110 m, that is a region where the *N(z)* functions have a regular behaviour. For regions where *N(z)* is noisy we decided as a first choice, to assign the nearest regular *N(z)* function.

The inversion carried on using the above mentioned depth-weighting distribution, varying both with depth and with position along the anomaly profile, gives the most reliable distribution of the source, allowing to have a more precise estimate both of the top and the bottom of the cylinder source (Figure 4.8c).

The 2D source domain was discretized with 200x30 cells, each sized 1x1 m. We assumed a vertical direction for both the inducing field and the magnetization vector.

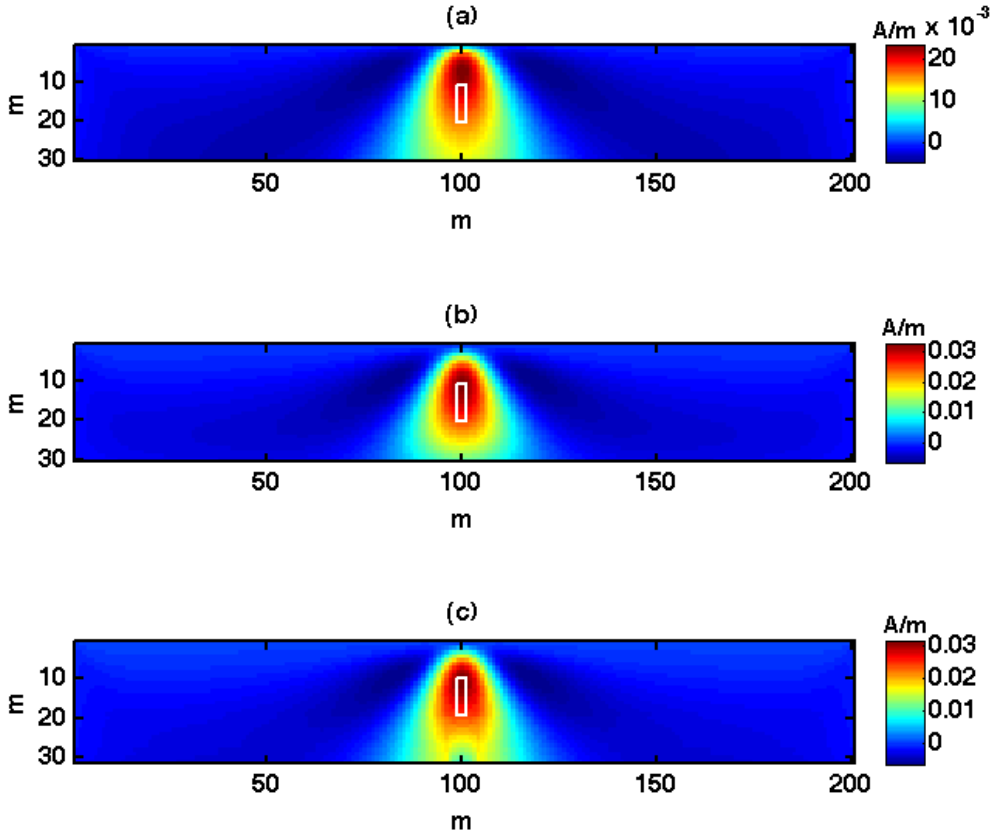

Figure 4.8 - Magnetization distribution derived inverting data in Figure 4.4b using different depth-weighting parameters: 1 (in panel a), depth-weighting index varying with z according to Fig. 4.4a (in panel b), depth-weighting index varying both with x and z according to Fig. 4.7a-b-c-d (in panel c)

Another option to build the inhomogeneous depth-weighting function could be to use the information given by the noisy *N(z)* as an "alarm bell" telling us that something is happening at that position. Since at this stage of the testing we know the sources which generate the field, we can easily find a connection between the *N(z)* noisy region and the boundaries of the source.

Following this idea we run another inversion and the resulting magnetization distribution is shown in Figure 4.9. We set the depth-weighting function equal to the previous example where *N(z)* is regular, while we attribute to the noisy region the *N(z)* estimated at the profile borders.

The result is a source distribution with an abrupt change clearly visible when the depth-weighting fuction switches from the "internal" estimate to the "external" one.

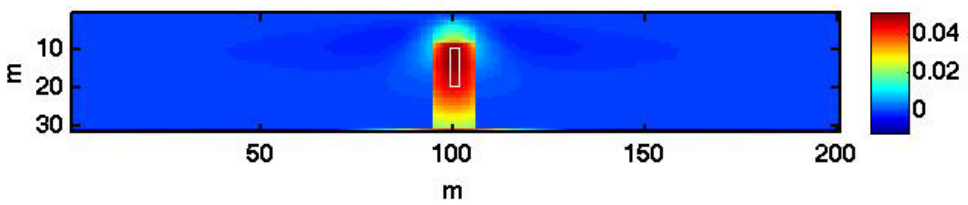

Figure 4.9 - Magnetization distribution derived inverting data in Figure 4.4b using different depth-weighting parameters: 1 (in panel a), depth-weighting index varying with z according to Fig. 4.4a (in panel b), depth-weighting index varying both with x and z according to Fig. 4.7a-b-c-d (in panel c) modified following an "alarm bell" approach.

4.3. Synthetic examples

In the following paragraph we will show the validity of the method for different 2D[3] magnetic synthetic anomalies generated by single sources with different horizontal limits, and multiple sources whose effects interfere on each other.
For each of the following synthetic examples the 2D inversion source domain has been discretized with 200x30 cells, each sized 1x1 m.
We have assumed for all the subsequent examples a vertical direction for both the inducing field and the magnetization vector.

A finite vertical cylinder with unitary vertical magnetization, top base at 10 m and bottom base at 20 m, horizontal boundaries at 97 m and 103 m.

We first applied the workflow to the anomaly (Figure 4.11a) generated by a finite vertical cylinder, whose extension in the x direction (along the anomaly profile) is not unitary. We have upward continued the field and extracted the *N(z)* functions along the profile through multi-scale analysis. As one can easily see from Figure 4.10, the *N(z)* function became unstable at x = 112 m. This information is useful for the construction of the depth-weighting function, since we can use the *N(z)* estimates from the centre of the anomaly (x = 100 m) until the limit of the unstable zone mentioned before (x = 111 m) and use this last stable estimate to cover the rest of the anomaly profile.

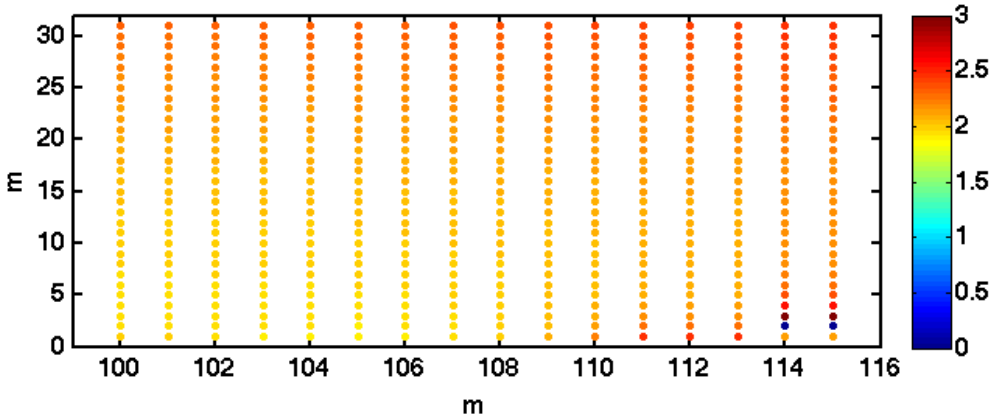

Figure 4.10 – N(z) estimates for different position along the anomaly in Fig. 4.11a. Labels stand for the x position along the profile (refer to Fig. 4.11a).

Figure 4.11c shows the results of the inversion carried on setting a depth-weighting function which varies with both with z and x, while Figure 4.11b

[3] The two-dimensional (2D) approach assumes that the source body causing the anomaly is infinitely long parallel to the strike of the data profile direction.

shows the result of the same inversion with a depth-weighting factor equal to 1. It is clear from the comparison of the magnetization distributions that using a depth-weighting function varying in the x-z space allows to get a better definition of the horizontal and vertical extension of the source, while the maximum of the distribution is placed more towards the source center.
As already mentioned in paragraph 4.1, note that the magnetic anomaly is symmetrical respect to the center of the profile, so the *N(z)* functions are shown only for the eastern side of the anomaly, these findings can be applied symmetrically to the western side.

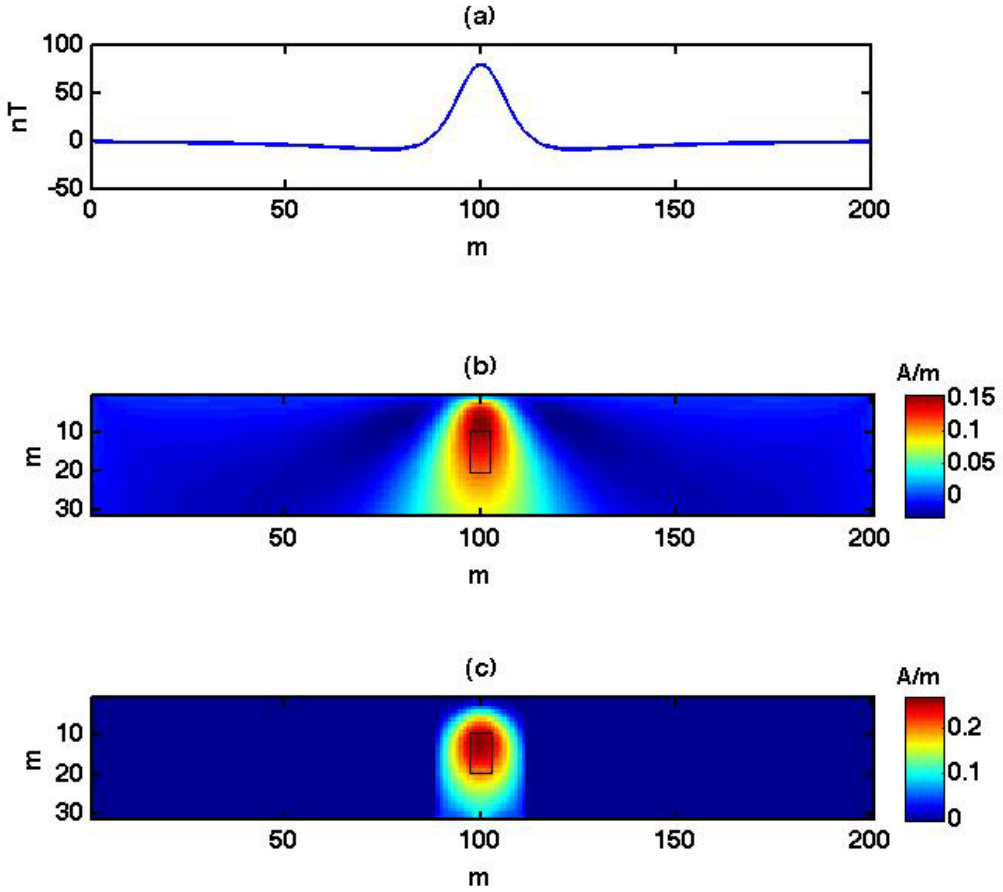

Figure 4.11 – (a) Magnetic anomaly of a finite vertical cylinder, with unitary vertical magnetization, top base at 10 m and bottom base at 20 m, horizontal boundaries at 97 m and 103 m; (b) magnetization distribution using different depth-weighting parameters: 1 (in panel a), depth-weighting index varying with x and z according to Fig. 4.10.

A finite vertical cylinder with unitary vertical magnetization, top base at 10 m and bottom base at 20 m, horizontal boundaries at 90 m and 110 m.

Now we consider the anomaly (Figure 4.10a) generated by a finite vertical cylinder, whose extension in the x direction (along the anomaly profile) is

larger than the previous example. The *N(z)* functions estimated from the multiscale analysis are plotted in Figure 4.12. In this case the area where the *N(z)* can be labelled as stable, is larger than the previous example (from x=100 to x = 115 m) . This issue confirm again our iphotesis that the boundaries of the source would cause some "noise effect" on *N(z)* estimates. In this case the depth-weighting function has been build using *N(z)* from x = 100 m to x = 114 m.

The considerations made for the *N(z)* functions on the east side of the profile have been extendend symmetrically to the west side since the anomaly is symmetrical.

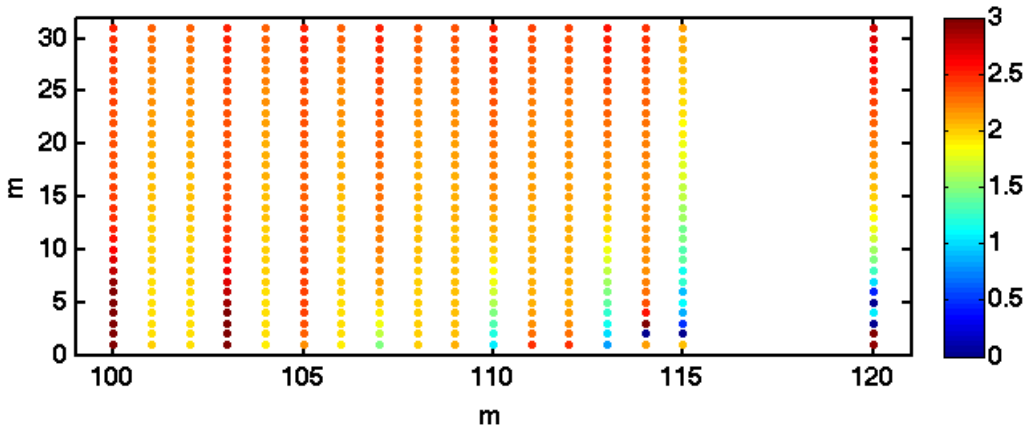

Figure 4.12 - N(z) estimates for different position along the anomaly in Fig. 4.13a. Labels stand for the x position along the profile (refer to Fig. 4.13a).

Figure 4.13c shows the results of the inversion carried on setting a depth-weighting function, which follows the estimates shown in Figure 4.12. The same inversion result, but this time with a depth-weighting factor equal to 1 is shown in Figure 4.13b. Here again the advantages of using the information derived from multi-scale analysis can be clearly appreciated: a better definition of the horizontal and vertical extension of the source, and the maximum of the distribution placed quite at the source center.

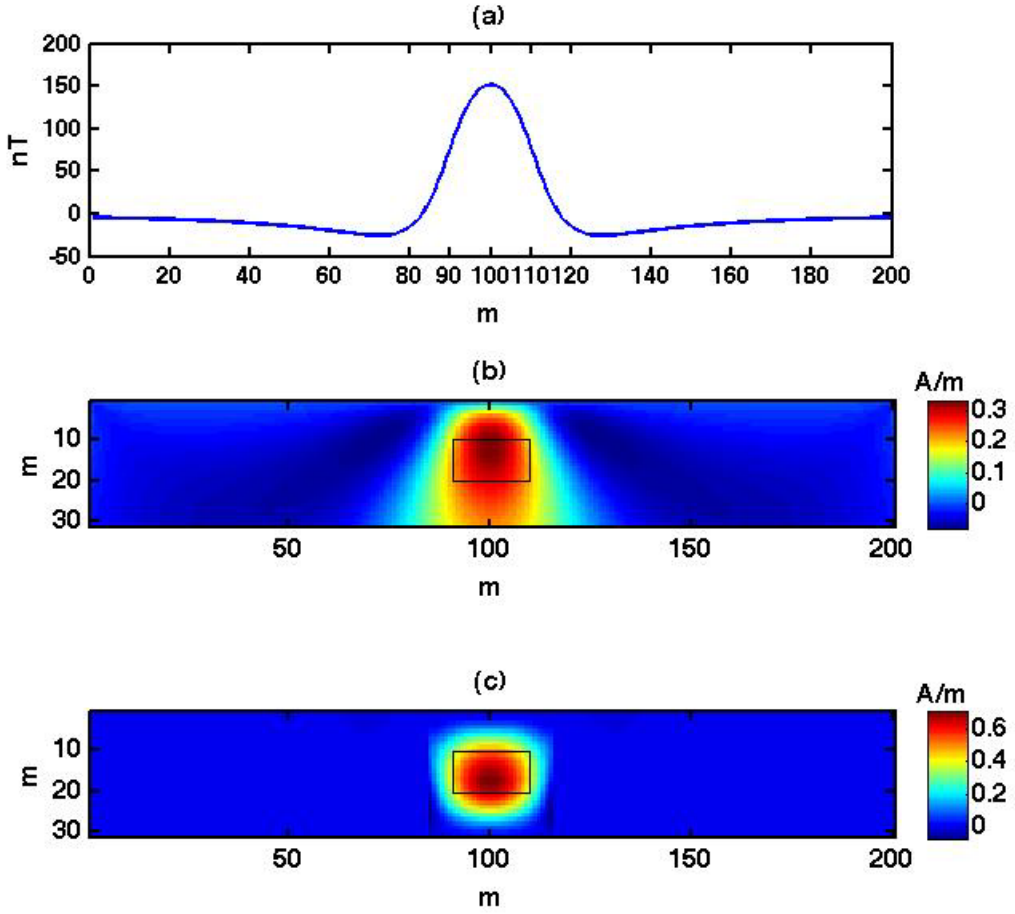

Figure 4.13 - (a) Magnetic anomaly of a finite vertical cylinder, with unitary vertical magnetization, top base at 10 m and bottom base at 20 m, horizontal boundaries at 90 m and 110 m; (b) magnetization distribution using different depth-weighting parameters: 1 (in panel a), depth-weighting index varying with x and z according to Fig. 4.12.

A finite vertical cylinder with unitary vertical magnetization, top base at 10 m and bottom base at 20 m, horizontal boundaries at 80 m and 120 m.

We could now inspect then the anomaly (Figure 4.15a) generated by a finite vertical cylinder, whose extension in the x direction (along the anomaly profile) is even larger than the two previous examples. The *N(z)* functions estimated from the multiscale analysis are plotted in Figure 4.14. In this case the area where the *N(z)* can be labelled as stable span from x = 100 m to x = 123 m). Here again we set the depth-weighting function using *N(z)* estimates from x = 100 m to x = 122 m, and symmetrically on the left side of the profile.
Figure 4.15c shows the results of the inversion where the depth-weighting function follows the estimates of *N(z)* shown in Figure 4.14. The result of the inversion with a depth-weighting factor equal to 1 is shown in Figure 4.15b.

The magnetization intensity model, shown in Figure 4.15c, allow again to define better the horizontal and vertical limits of source.

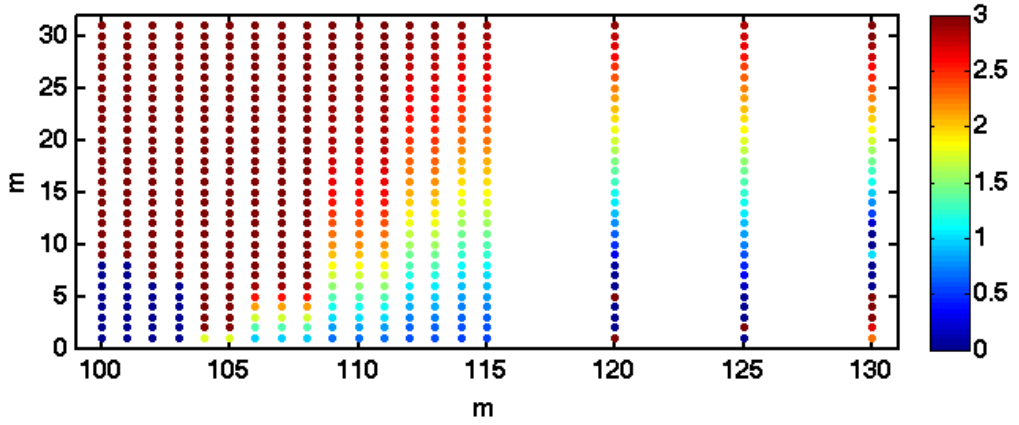

Figure 4.14 - N(z) estimates for different position along the anomaly in Fig. 4.15a. Labels stand for the x position along the profile (refer to Fig. 4.15a).

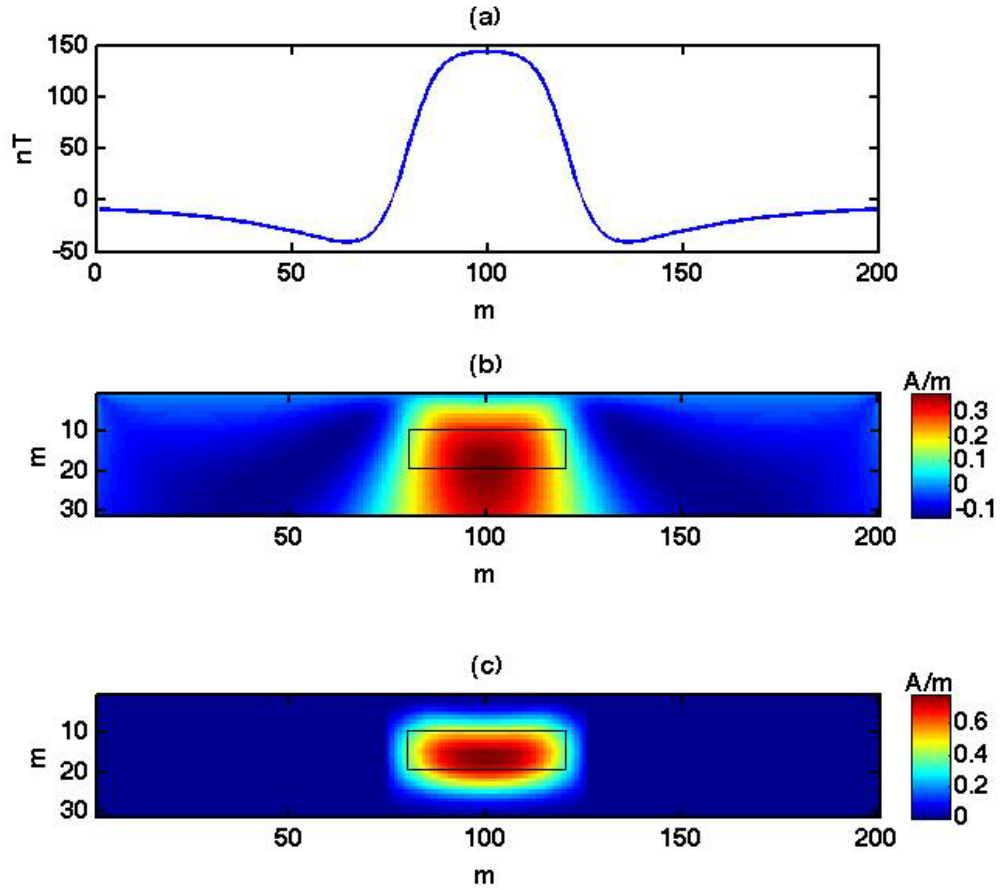

Figure 4.15 – (a) Magnetic anomaly of a finite vertical cylinder, with unitary vertical magnetization, top base at 10 m and bottom base at 20 m, horizontal boundaries at 80 m and 120 m; (b) magnetization distribution using different depth-weighting parameters: 1 (in panel a), depth-weighting index varying with x and z according to Fig. 4.14.

A couple of finite vertical cylinders with unitary vertical magnetization placed at x_1=67 m and x_2=134 m, top base at 10 m and bottom base at 20 m, width of 1 m respect to their centre.

We have applied the workflow to the anomaly (Figure 4.17a) generated by two finite vertical cylinders, whose extension in the x direction (along the anomaly profile) is unitary. Each source contribute does not interfere with the other, as we can clearly distinguish two maxima in the magnetic anomaly.

The multi-source case is particularly interesting in the inversion domain, as we showed in chapter 2.5; usually one shuld set separate depth-weighting parameters for each source and maybe determine a threshold to switch from one to the other; the possibility to determine an *N(z,x)* function with a multi-scaling information would be really useful: we will see in the following example that this will guide the depth-weighting function setting in the zone between the sources.

We have upward continued the field and extracted the *N(z)* functions along the profile through multi-scale analysis.

Starting from x = 67 m, where the left source shows a maximum on the anomaly, and going towards the left border of the anomaly we have seen that *N(z)* function varies gradually, as we have already noticed for the single source case *N(z)* estimates are not shown in this case since they are redundant. The same behaviour has been sampled on the other side of the profile, going from x = 134 m to higher x values.

In the zone between the two maxima of the field *N(z)* varies gradually again becoming noisy between x = 76 m and x = 79 m (Figure 4.16).

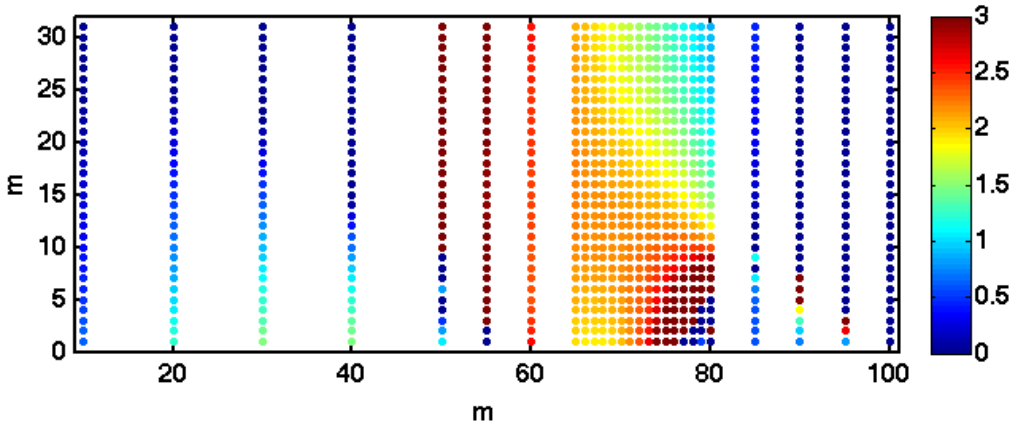

Figure 4.16 - N(z) estimates for different position along the anomaly in Fig. 4.17a. Labels stand for the x position along the profile (refer to Fig. 4.17a).

Looking at the behaviour of the source index function we decided to assign the depth-weighting function as follows:

- for x going from x = 56 m to x = 78 m we used the estimated N(z) function, evaluating the window extension on the basis of the interference zone between the two field maxima;
- the depth-weighting function for the interference zone are derived from the correspondent undisturbed portion of the profile.

The same choices have been done simmetricaly for the source on the right side.

The result of the inversion performed with such a depth-weighting function is shown in Figure 4.17 (c), compared with the inversion result using an invariant depth-weighting factor for the whole model space.

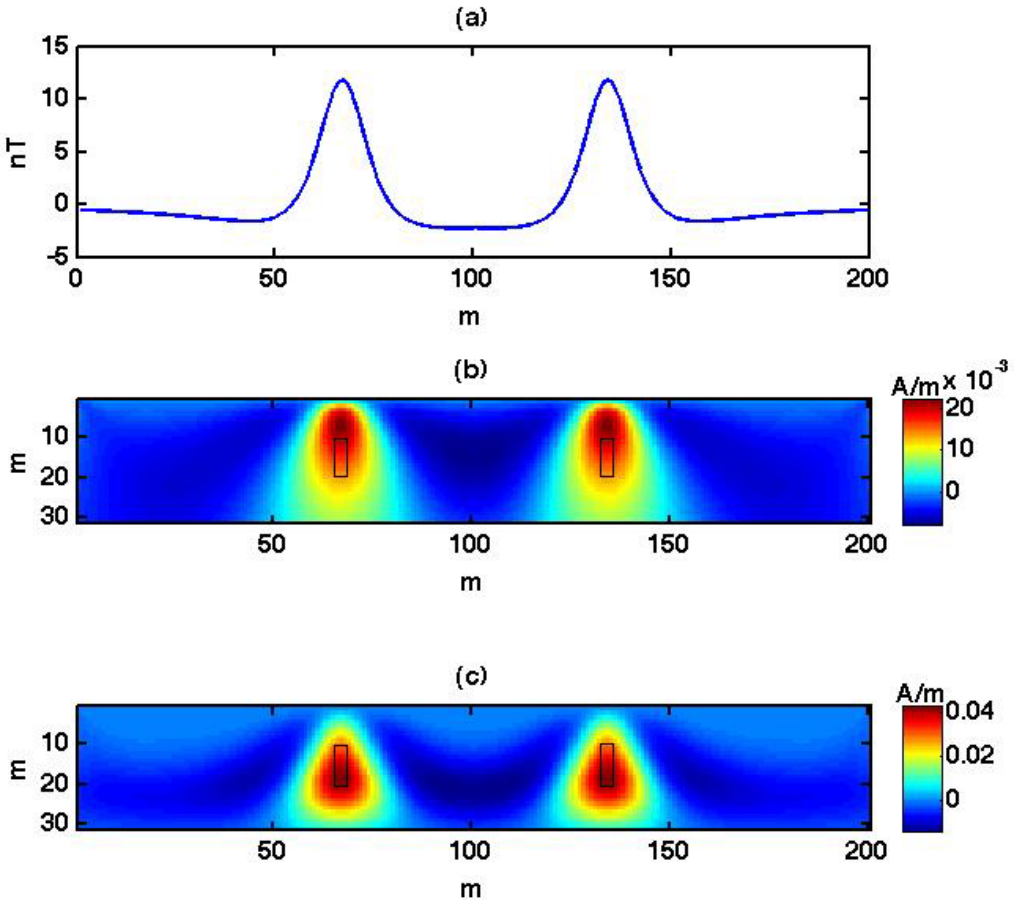

Figure 4.17 - (a) Magnetic anomaly of two finite vertical cylinders, with unitary vertical magnetization, top base at 10 m and bottom base at 20 m, placed at x_1=67 m and x_x=134 m; (b) magnetization distribution using depth-weighting parameters equal to 1 and depth-weighting index varying with x and z (c) according to Fig. 4.16.

A couple of finite vertical cylinders with unitary vertical magnetization placed at x_1=95 m and x_2=105 m, top base at 10 m and bottom base at 20 m, width of 1 m respect to their centre.

We have applied the workflow to the anomaly (Figure 4.17a) generated by two finite vertical cylinders, whose extension in the x direction (along the anomaly profile) is unitary. Each source contribute heavily interferes with the other, as we cannot distinguish two maxima on the magnetic anomaly.
The multi-scale analysis reveals that at x = 100 m, where the field has its maximum, the N(z) function is noisy and become stable again at x = 102 m. From this point on it varies gradually up to x = 108 m. From x = 113 m on, the N(z) does not vary with the position along the profile.

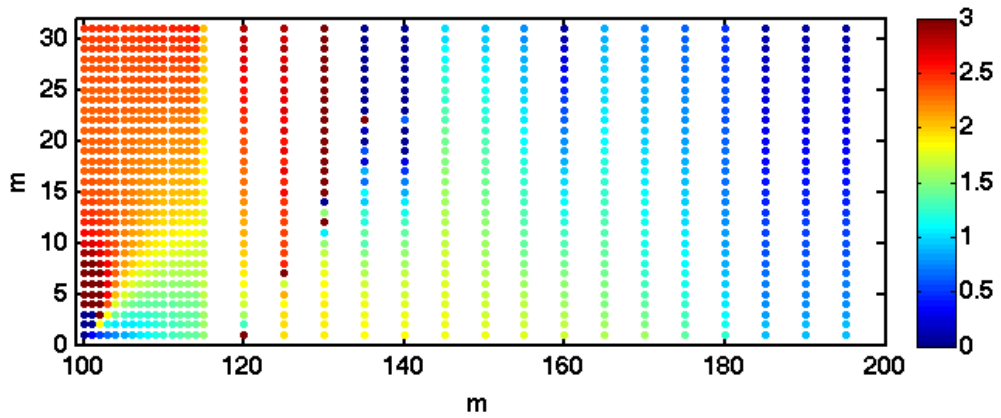

Figure 4.18 - N(z) estimates for different position along the anomaly in Fig. 4.19a. Labels stand for the x position along the profile (refer to Fig. 4.19a).

The depth-weighting function has been set taking in account all the estimated N(z) from x = 102 on, while the noisy N(z) at x = 100 to 101 have been substituted with the nearest stable one, that is N(z, x = 102) and N(z, x = 98) respectively.

The result of the inversion with depth-weighting varying both in z and x direction is shown in figure 4.19c: even if the magnetization distribution is smooth it is possible to distinguish two maxima in the distribution corresponding to the position of the two sources.

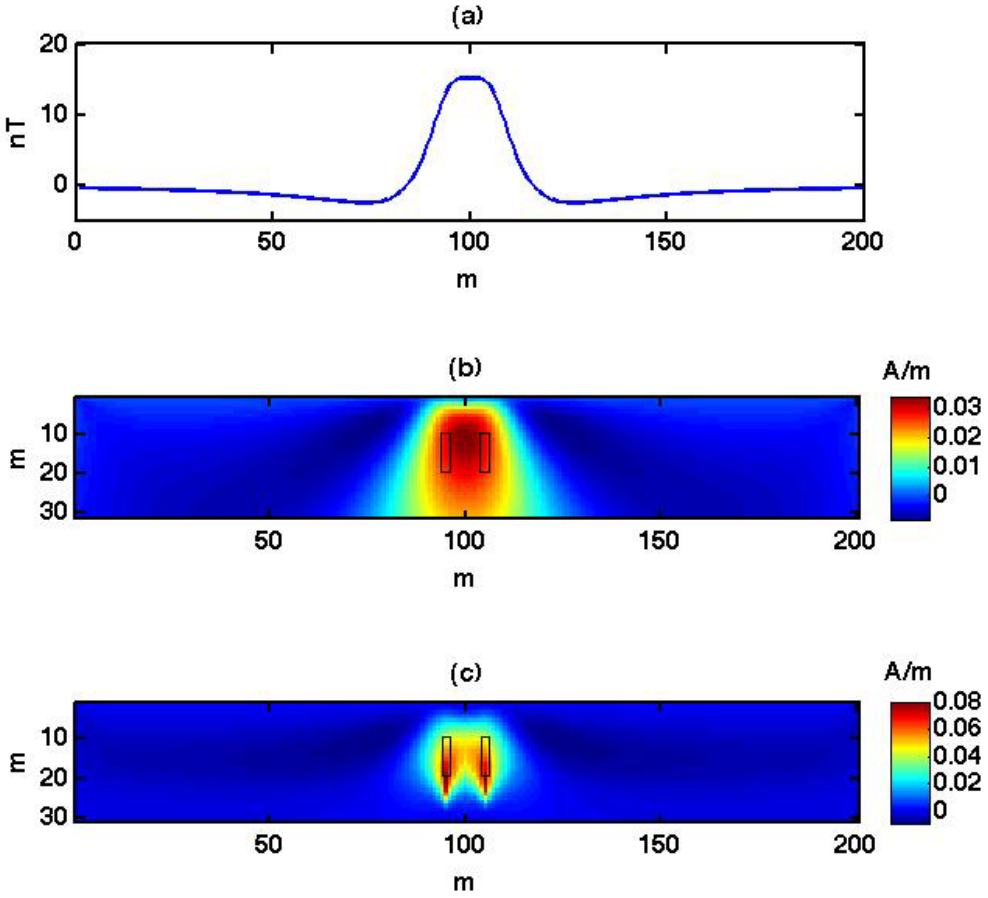

Figure 4.19 - (a) Magnetic anomaly of two finite vertical cylinders, with unitary vertical magnetization, top base at 10 m and bottom base at 20 m, placed at x_1=95 m and x_x=105 m; (b) magnetization distribution using depth-weighting parameters equal to 1 and depth-weighting index varying with x and z (c) according to Fig. 4.18.

The magnetic anomaly shown in Figure 4.19a could be also generated by a single source; we have examined this ambiguous case analysing the magnetic field caused by a 2D prismatic source whose horizontal limits are at x = 88 m and x = 112 m, top depth at 10 m and bottom depth at 15 m, magnetization intensity equal to 0.15 A/m.
The magnetic anomaly is shown in Figure 4.19bis (panel b) with a green dashed line while the anomaly caused by two interferent sources is shown in blue.

The multiscale analysis result can be seen in Figure 4.19 bis (panel a): the N(z) functions show now a regular behaviour in the area between x = 100 m and x = 102 m while in the previous case they showed a noisy shape; this confirms that the multiscale analysis could also help in the inspection of ambiguous cases.

The result of the inversion of the data in Fig. 4.19bis(b) are shown in Fig. 4.19bis(c); we have set-up as usual a variable depth-weighting function following the results from Fig. 4.19bis(a).

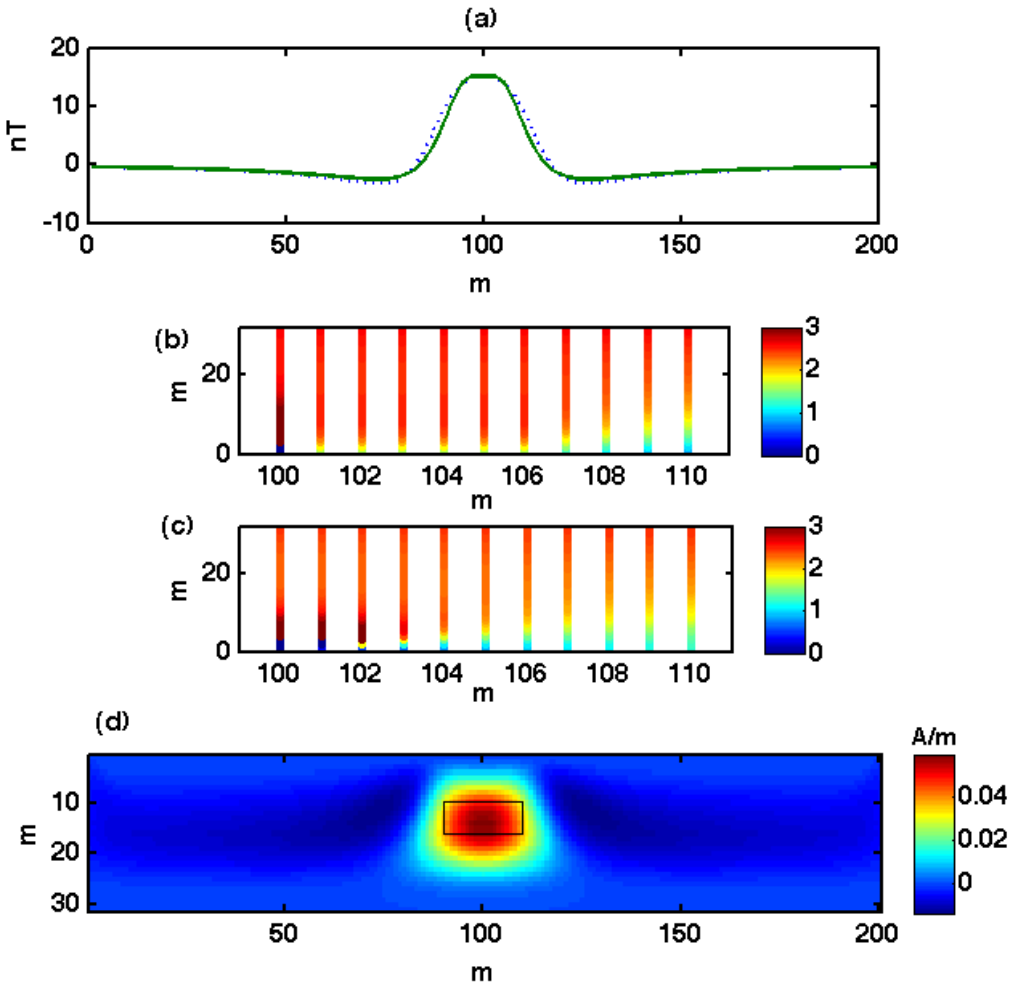

Figure 4.19bis – (a) Magnetic anomaly of a 2D prismatic source whose horizontal limits are at x = 88 m and x = 112 m, top depth at 10 m and bottom depth at 15 m, magnetization intensity equal to 0.15 A/m; (b) N(z) estimates for different position along the anomaly in Fig. 4.19bis(a): labels stand for the x position along the profile (refer to Fig. 4.19bis (b)). (c) magnetization distribution from inversion with depth-weighting index varying with x and z (c) according to Fig. 4.19bis(a).

A couple of finite vertical cylinders with unitary vertical magnetization placed at x_1=95 m and x_2=105 m, top base at 15 m and bottom base at 25 m, width of 1 m respect to their centre.

We have tested the method on a couple of source with the same charachteristic of the previous example but increasing their depths. The resulting anomaly is

shown in Figure 4.21a. The sources contributes heavily interfere on each other, as only one maximum is distinguishable on the magnetic anomaly.

The multi-scale analysis in the previous example showed noisy N(z) in correspondence of the anomaly maximum, now the same N(z) at x = 100-101 m are stable and can be used in the depth-weighting function.

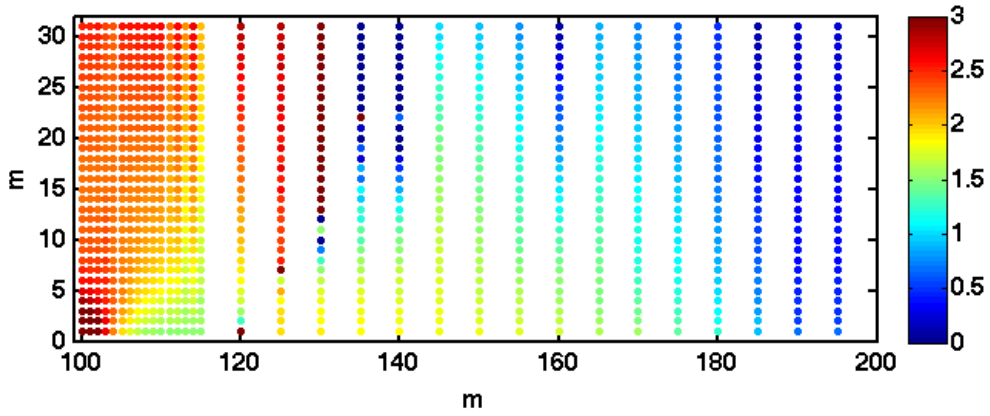

Figure 4.20 – N(z) estimates for different positions along the anomaly in Figure 4.21a. Labels stand for the x position along the profile, refer to Figure 4.21a.

The result of the inversion with depth-weighting varying both in z and x direction is shown in figure 4.21c: here again the magnetization distribution is smooth, but in correspondence of its maxima it is possible to place the sources centres.

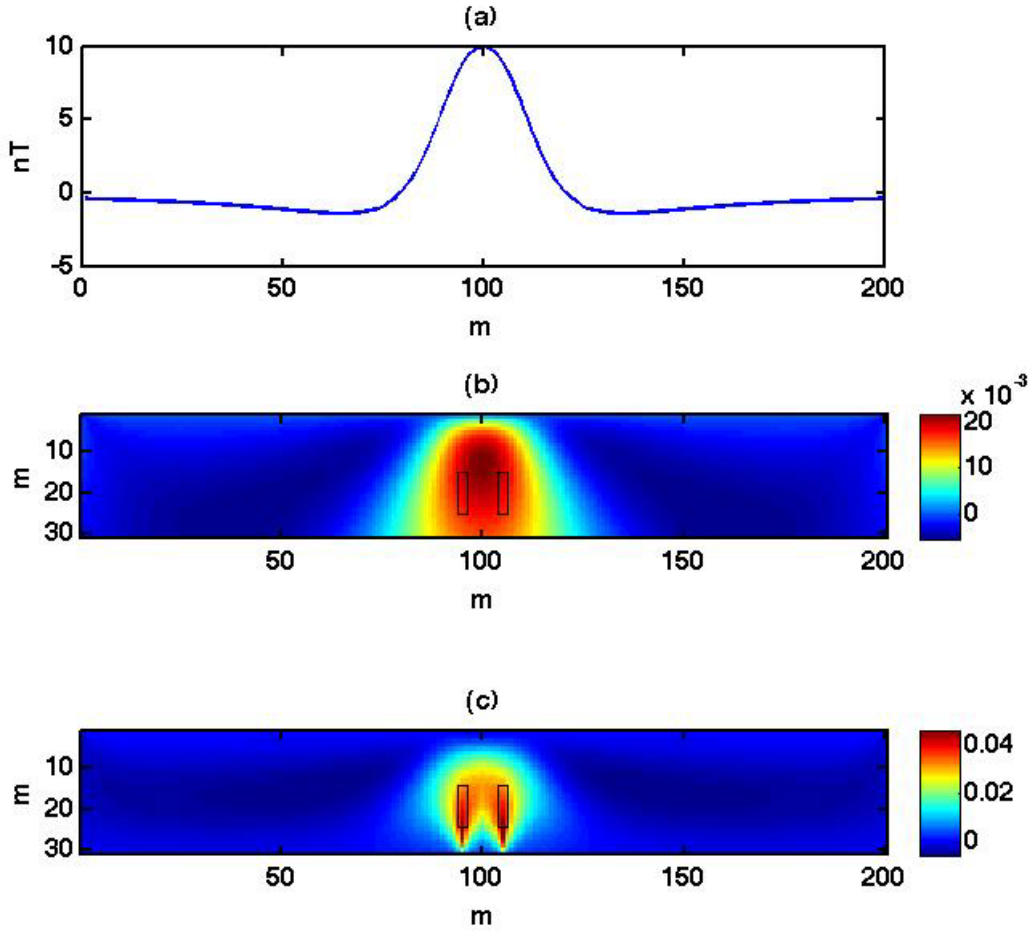

Figure 4.21 - (a) Magnetic anomaly of two finite vertical cylinders, with unitary vertical magnetization, top base at 15 m and bottom base at 25 m, placed at x_1=95 m and x_x=105 m; (b) magnetization distribution using depth-weighting parameters equal to 1 and depth-weighting index varying with x and z (c) according to Fig. 4.20.

A couple of finite vertical cylinders with unitary vertical magnetization placed at x_1=95 m and x_2=105 m, and at different depths, width of 1 m respect to their centre.

The case of the anomaly generated by two finite vertical cylinders can be made more interesting placing the sources at different depth.

The multi-scale analysis results for the magnetic anomaly in Figure 4.23a is shown in Figure 4.22: the stable N(z) have been used for the depth-weighting fuction while the noisiest ones have not (for example N(z) at x = 105-106-107).

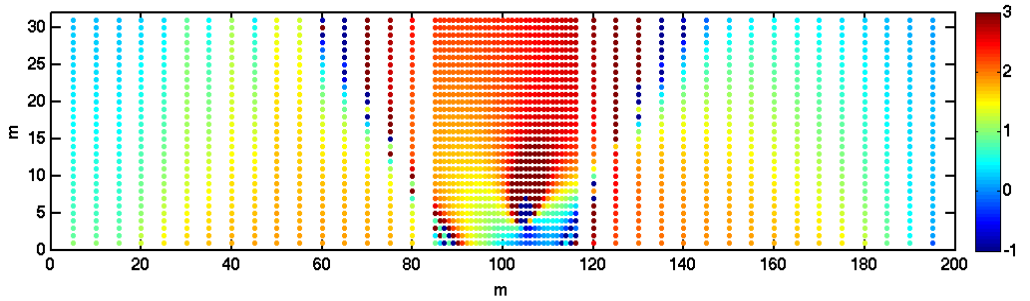

Figure 4.22 – N(z) estimates for different positions along the anomaly in Figure 4.23a. Labels stand for the x position along the profile, refer to Figure 4.23a.

The results of the inversion are shown in Figure 4.23c: it is clear that inverting with a constant depth-weighting factor it is not possible to distinguish the two sources, maybe one could argue that the source has an asymmetric shape; while when we invert using a multi-scale derived depth-weighting two maxima are distinguishable in the magnetization distribution, and their position is comparable with the sources depth.

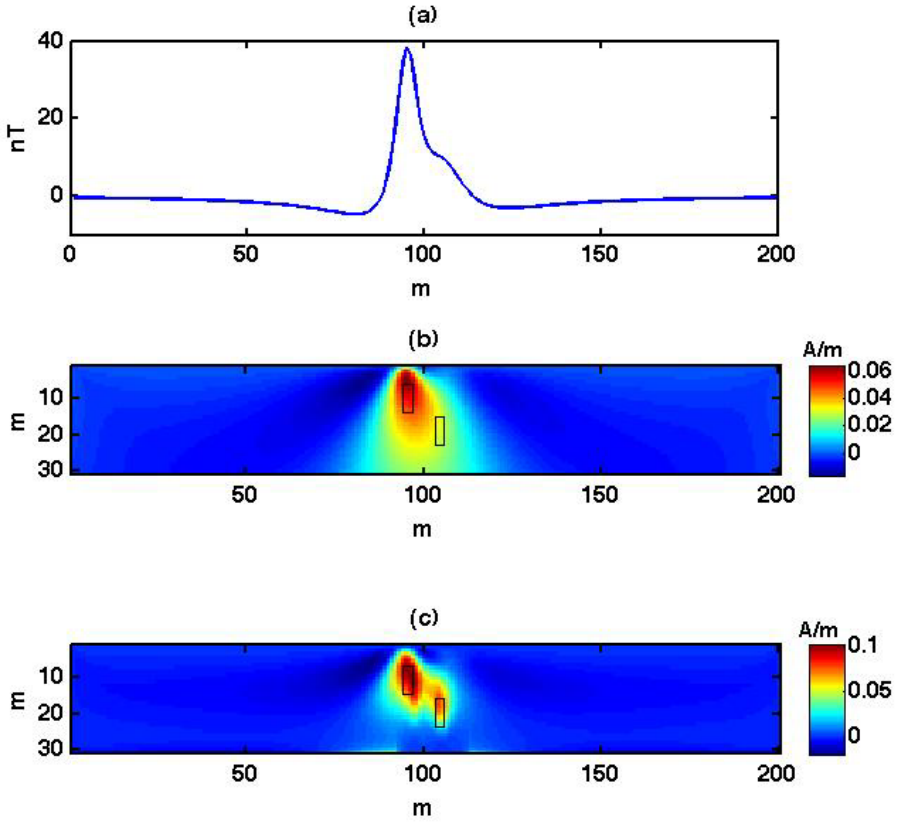

Figure 4.23 - (a) Magnetic anomaly of two finite vertical cylinders, with unitary vertical magnetization, top base 1 at 5 m and top base 2 at 15 m, placed at x_1=95 m and x_x=105 m; (b) magnetization distribution using depth-weighting parameters equal to 1 and depth-weighting index varying with x and z (c) according to Fig. 4.22.

To inspect the behaviour of our approach in the presence of noise we have contaminated the magnetic field generated by a couple of finite vertical cylinders with independent Gaussian noise having a zero mean and a standard deviation of 10% of each data plus 1% of the data maximum (Fig. 4.25a).
The multi-scale analysis results for the magnetic anomaly in Figure 4.25a is shown in Figure 4.22. Most of the N(z) functions showed outlier values, but they all show a trend consistent with the one found in the noise-free case (Fig. 4.22). So we have decided to smooth the noisy N(z) functions before using them for the depth-weighting fuction.

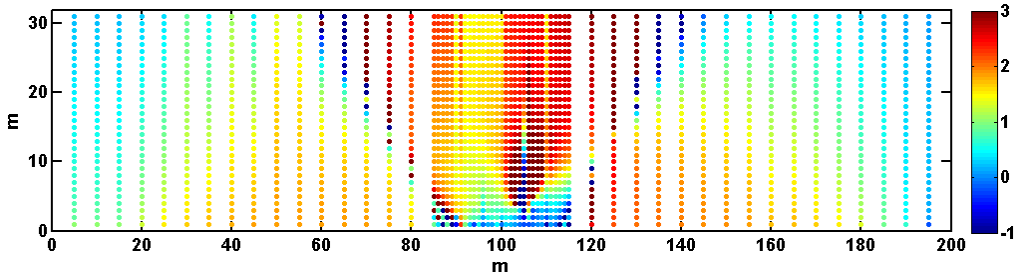

Figure 4.24 - N(z) estimates for different positions along the anomaly in Figure 4.25a. Labels stand for the x position along the profile, refer to Figure 4.25a.

The results of the inversion are shown in Figure 4.25c: as already said for the noise-free case, it is not possible to distinguish between the two sources inverting with a constant depth-weighting factor; while the inversion constrained by a multi-scale derived depth-weighting shows two maxima distinguishable in the magnetization distribution, with their position is comparable with the sources depth.

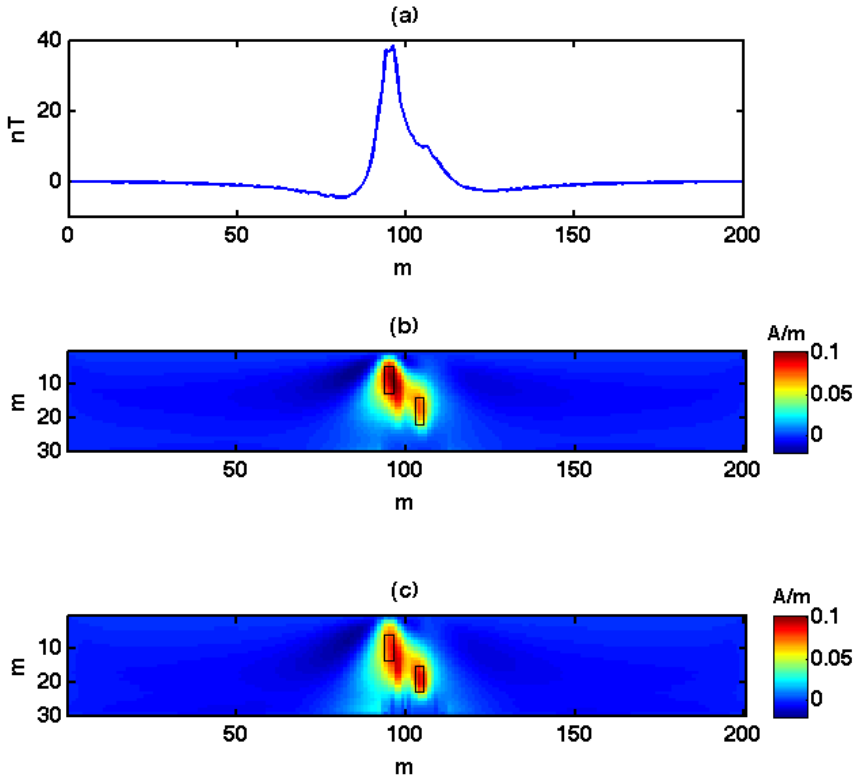

Figure 4.25 - (a) Magnetic anomaly contaminated with noise of two finite vertical cylinders, with unitary vertical magnetization, top base 1 at 5 m and top base 2 at 15 m, placed at x1=95 m and xx=105 m; (b) magnetization distribution using depth-weighting parameters equal to 1 and depth-weighting index varying with x and z (c) according to Fig. 4.22.

A couple of prism, a shallower one and a deeper bigger one, with unitary vertical magnetization placed at x =100 m.

As a further step, we analysed the anomaly generated by two prisms with unitary magnetization intensity, a smaller one, with edges at x = 99 m and x = 101 m, put on top of a bigger one with edges at x = 90 and x = 110. This is the most difficult case bebause the field generated by the smaller source is masked by the one from the deepest one.

The multi-scale analysis of the field is shown in Figure 4.26: the N(z) functions are stable from the maximum of the anomaly (x = 100 m) and start to be noisy at x = 108 m, just in the nearby of the bigger source horizontal limits.

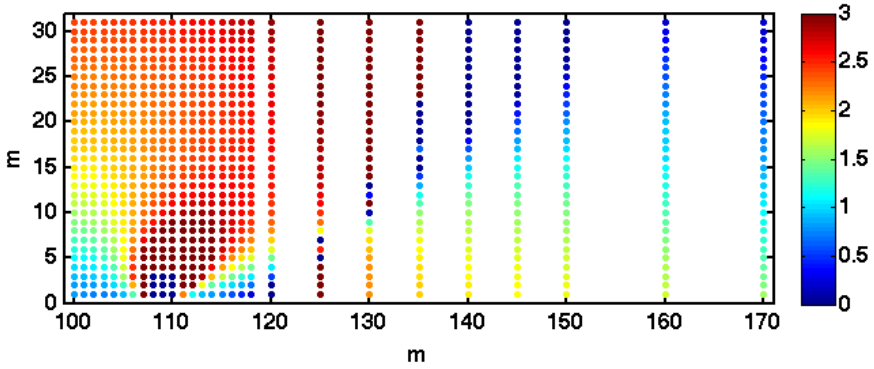

Figure 4.26 - N(z) estimates for different positions along the righ side of the anomaly in Figure 4.25a. For the x position along the profile, refer to Figure 4.27a.

Building a depth weighting function on the base of the N(z) estimates in Figure 4.26 and inverting the data, we obtain the magnetization distribution shown in Figure 4.27 c. We can note that respect to the constant depth-weighting result, the distribution in Fig. 4.26c takes in account the contributes from both sources buti t is quite difficult to argue such correspondence with the sources limits. One suspicious issue could be the effect below the biggest source, which may syggest that more that one source is present.

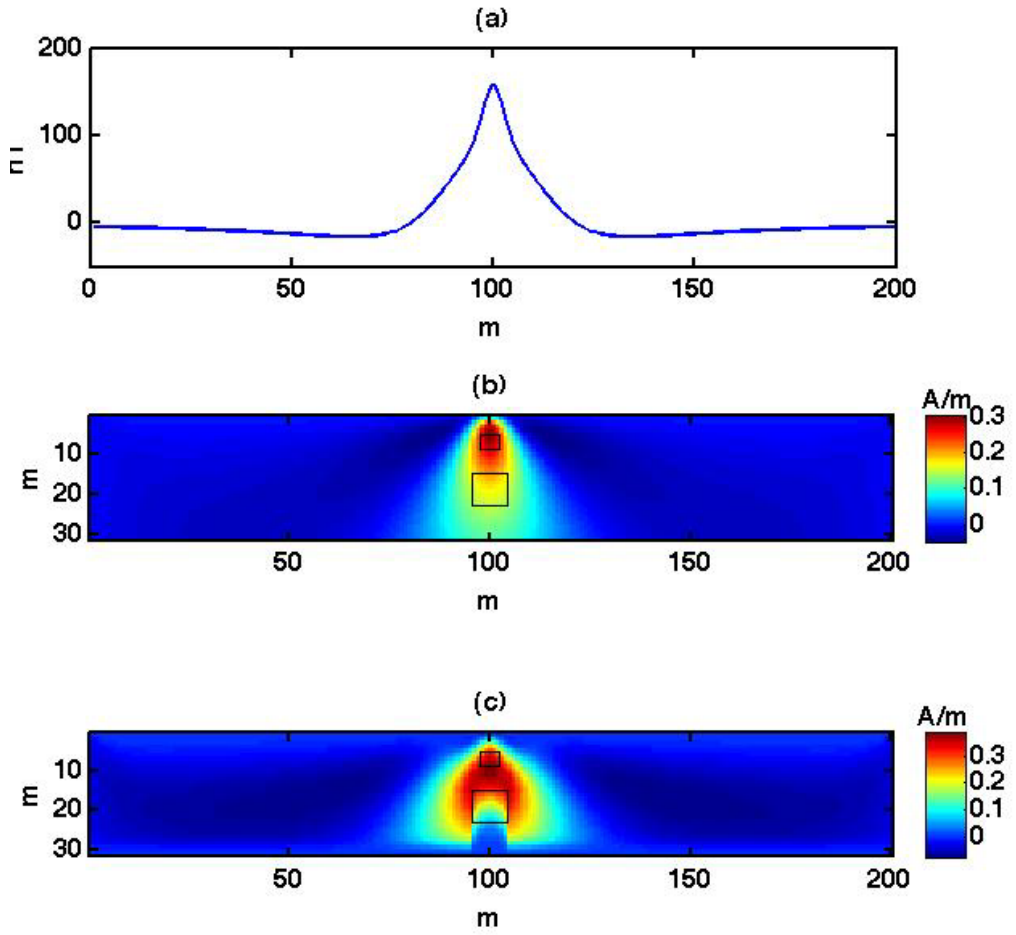

Figure 4.27 - (a) Magnetic anomaly of two overlaid prisms, with unitary vertical magnetization, the smaller is placed at 5 m depth, the bigger is placed at 20 m depth; (b) magnetization distribution using depth-weighting parameters equal to 1 and depth-weighting index varying with x and z (c) according to Fig. 4.26.

4.4. Real data example: Pompei and Acerra Basins

We have lastly applied the integrated method to the real case of the Campanian Plain Bouguer gravity data (southern Italy). The gravity field shown in Figure 4.28 is a residual field after subtraction of a long-wavelength trend (Rapolla et al., 1989).

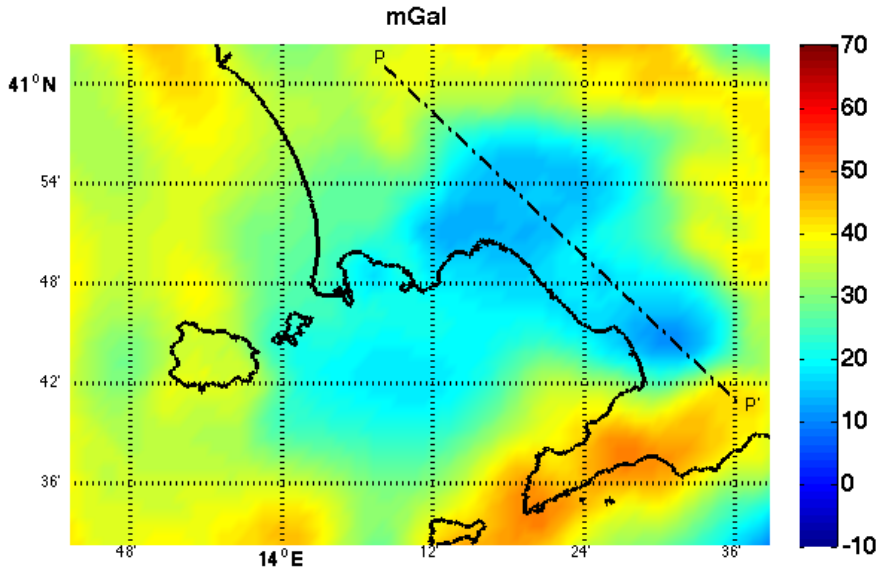

Figure 4.28 – The Bouguer gravity field of the Campanian area (Souther Italy), charachterized by a complex patter of lows, related to basins, and highs, mostly related to carbonate complexes exposed at the surface.

The Campanian Plain is a Plio-Pleistocene tectonic depression, bounded to the northwest, northeast, and southeast by Mesozoic carbonate platforms and to the southwest, by the Tyrrhenian Sea. The maximum depth of the carbonate platforms in this area is of about 5 km, as reported by many autors (i.e. Ippolito et al., 1973). Overlying the carbonates are sediments of alluvial and volcanic origin. Quaternary volcanic areas, including the Somma-Vesuvius and the Phlegrean volcanic district, are also present in the area.
The plain is characterized by a wide Bouguer anomaly low, which includes the area of the town of Naples, between Phlegrean Fields and Somma-Vesuvius (see for further details Florio et al., 1999).
We applied the integrated imaging-inversion approach to the gravity field of the Campanian region without resorting to prefiltering.

We have analysed a profile located along line PP' in Figure 4.28, which crosses some of the shallow lows features of the map, corresponding to several basins, such as Acerra and Pompei.

As we already explained in section 3.2, complex sources like pipes, ridges, valleys, tunnels, volcanic necks, can be seen as infinite cylinders, and so can be considered as 2D sources. This could be the case of the gravity lows and highs recognisable on the profile in Figure 4.28a, which are definitely suitable candidates for our analysis.

The multi-scale analysis of the field is shown in the following figure:

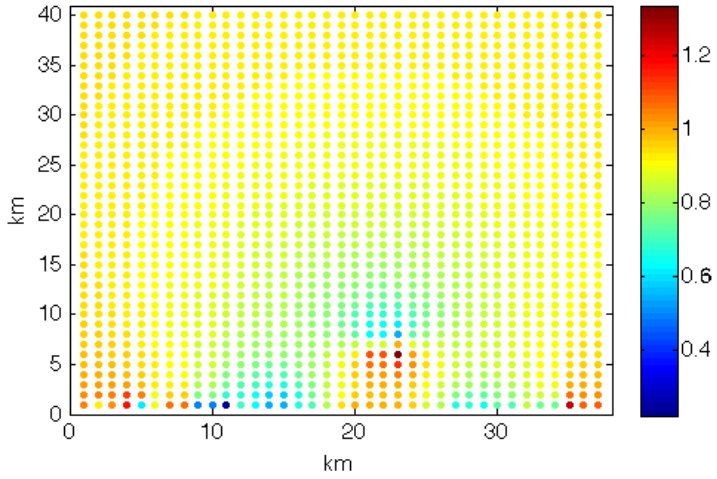

Figure 4.29 - *N(x,z)* estimates for different positions (x axis) along the anomaly in Figure 4.28a.

We first run an inversion setting a constant depth weighting factor equal to 2, which is typical of sources whose shape can be approximated by an infinite cylinder, as estimated also by Fedi (2007). Then we run a second inversion setting a variable depth weighting according to the multiscale *N(z)* estimates we made in Figure 4.29. In both cases the 2D inversion source domain has been discretized with 37x40 cells, each sized 1x1 km. We decided not to take in account *N(z)* estimates derived at x positions 8, 10, 15, 22, 34, 37, and we attribute to these position the closer stable *N(z)*.

The inversion results are show in Figure 4.30b for constant *depth-weighting* and in Figure 4.30c for variable depth weighting. In the second case there is an improvement in the resolution of the density contrasts distribution both in the horizontal direction and in the vertical direction: the minima related to the Pompei and Acerra basin are better separated and do not merge at a certain depth; while a local minimum is distinguishable ata depth of about 30 km, and can be maybe related to an unknoe deep source already identified in previous studies, as mentioned also by Fedi (2007).

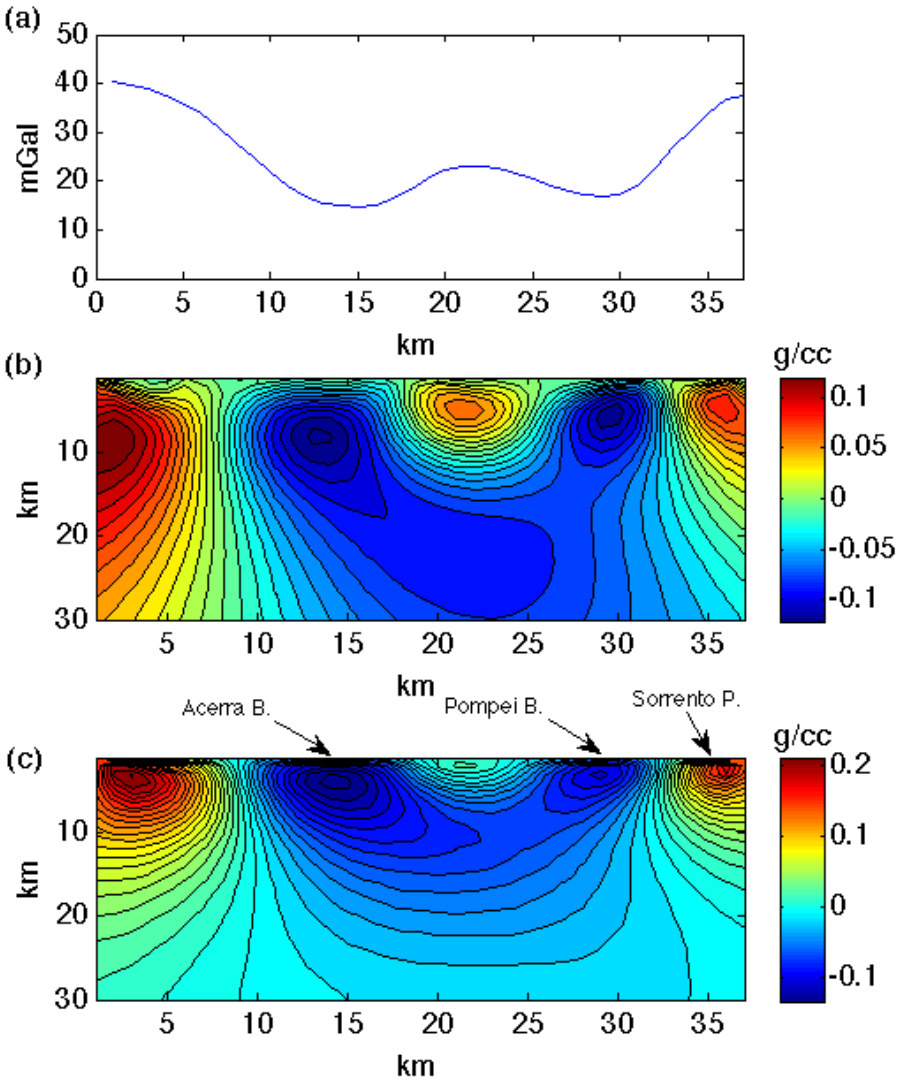

Figure 4.30 - (a) Bouger gravity anomaly along the profile PP' shown in Fig. 4.26; (b) density contrasts inversion distribution using a depth-weighting parameter equal to 2 and a depth-weighting index varying with x and z (c) according to Fig. 4.27. Shallow lows correspond to Acerra and Pompei basins, a relatively deep low marks a deeper source, while the shallow high eastwards correspond to the Sorrento Peninsula carbonate platform.

5. Abstracts of published papers

The PhD research field has been enlarged also on the upward continuation transform of potential field data. This transformation is at the base of most multi-scale methods, which need potential fields data available on a 3D volume. Therefore, we defined an alternative approach to upward continue potential field data: the VOCO (Volume Continuation), which has important advantages above existing techniques and is suitable for all types of data continuation between surfaces in the space. The VOCO approach descriprion and testing on synthetic and real data is the subject of Paper I.
Paper II instead concerns the combination of VOCO and second order horizontal derivatives of gravimetric data for the estimate of the sources horizontal limits with the field continuation height.
Complete published papers I and II are enclosed at the end of this document.

5.1. Paper I

Volume Continuation of potential fields from the minimum-lenght solution: An optimal tool for continuation through general surfaces

Daniela Mastellone, Maurizio Fedi, Simone ialongo, Valeria Paoletti

Many methods have been used to upward continue potential field data. Most techniques employ the Fast Fourier transform, which is an accurate, quick way to compute level-to-level upward continuation or spatially varying scale filters for level-to-draped surfaces.

We here propose a new continuation approach based on the minimum-length solution of the inverse potential field problem, which we call Volume Continuation (VOCO).
For real data the VOCO is obtained as the regularized solution to the Tikhonov problem. We tested our method on several synthetic examples involving all types of upward continuation and downward continuation (levelto-level, level-to-draped, draped-to-level, draped-to-draped). We also employed the technique to upward continue to a constant height (2500 m a.s.l.), the high-resolution draped aeromagnetic data of the Ischia Island in Southern Italy.

We found that, on the average, they are consistent with the aeromagnetic regional data measured at the same altitude. The main feature of our method is that it does not only provide continued data over a specified surface, but it yields a volume of upward continuation. For example, the continued data refers to a volume and thus, any surface may be easily picked up within the volume to get upward continuation to different surfaces. This approach, based on inversion of the measured data, tends to be especially advantageous over the classical techniques when dealing with draped-to-level upward continuation. It is also useful to obtain a more stable downward continuation and to continue noisy data. The inversion procedure involved in the method implies moderate computational costs, which are well compensated by getting a 3D set of upward continued data to achieve high quality results.

Preliminary results shown in this paper have been also presented in one of the poster sessions of the 83rd SEG Annual Meeting, held in Houston (USA) in September 2013.

5.2. Paper II

Accurate evaluation of edges and dip of faults and contacts through the Volume Upward Continuation (VUC) of gravity data

Daniela Mastellone, Maurizio Fedi, Valeria Paoletti

Several methods have been used to retrieve values of dip of faults by using lateral offsets of the zero-crossover point of the second horizontal derivative of upward-continued gravity profiles. The use of derivatives of potential fields represents a signal enhancement technique experimented since a long time. It allows the information content of the signal to be enhanced without implying any arbitrary assumption. Often, such methods are coupled with upward continuation, which is used to transform anomalies measured on one surface into those that would have been measured on some higher altitude surface.

In this paper we demonstrate the efficiency of a new approach to upward continue potential field data, the Volume Upward Continuation (VUC), coupled with traditional horizontal derivative techniques. By using VUC it is immediate showing that upward continuation of the signal to higher altitudes yields information about progressively deeper

sectors of the discontinuity. In particular, looking at the position of the maxima of the horizontal derivative of the continued field, we can observe that they will be laterally shifted toward the dipping direction of the discontinuity, in a way proportional to the continuation height.

We applied VUC followed by horizontal derivative to a gravity profile extracted from a gravity survey on the Venelin-Aksakov fault in Bulgaria, in order to get further information on the dipping direction of this structure.

Preliminary results shown in this paper have been also presented in one of the poster sessions of the Geoitalia 2013 Meeting held in Pisa in September 2013.

6. Conclusions and future research

In this thesis, we have studied in detail the relationship between potential field inversion algorithms (i.e. Li and Oldenburg, 2003), and multi-scale imaging techniques (Fedi, 2007): the aim of our work was to implement an integrated approach of potential fields data analysis using the benefits provided by both methods.

We found that the information derived from the multi-scale analysis, such as source shape parameters, could be efficiently used in the inversion algorithms to improve the resolution and the depth estimate on the inversion solutions. The inversion constraint, which can take advantage of the source-shape multiscale information, is the depth weighting function. This function is necessary to counteract the natural decay of the data kernel with depth, so providing depth resolution to the inverse solution.

Starting from Cella and Fedi (2012), we followed their idea of using a depth-weighting function with an exponent β equal to the correct structural index (N) of the source, and we estimated the variability of this index in a 2D space, getting out an $N(x,z)$ function.

Once a preliminary workflow has been defined, we have tested it on magnetic anomalies generated by simple sources (a dipoles line, a dike, a cylinder) and by more complex sources (e.g. couple of sources whose effects interfere with each other on the overall data). As a further example we have also tested the workflow on some real data from the Bouguer gravity anomaly map of Southern Italy.

We demonstrated the good performance of the integrated approach both for synthetic and real data; in particular, the results obtained from the test on real data show a good correspondence with the results obtained by Fedi (2007) for the same area.

Considering the achieved results, we can state that source information retrieved by a multi-scale analysis of the data has a great potential to lead to well-constrained solutions with respect to the source depth and to the horizontal variations of the source-density/magnetization intensity distribution.

The foundings of this integrated approach could be further expanded for application in the 3-dimensional space, making this topic particularly interesting for future research.

Throughout the development of the main topic of this thesis, we have also expanded our research field defining an alternative approach to upward continue potential field data: the VOCO (Volume Continuation), which has important advantages above existing techniques and is suitable for all types of data continuation between surfaces in the space. VOCO has also been coupled with second order horizontal derivatives of gravimetric data to investigate on the estimate of the sources horizontal limits changing the field continuation height value.

Results from this topic have been also subject for journal and conferences papers.

References

- Barbosa, V. C. F., Silva, J. B. C., Medeiros, W. E., 1999, *Stability analysis and improvement of structural index estimation in Euler deconvolution*. Geophysics, 64, 48-60.
- Blakely, R.J., 1996, *Potential theory in gravity and magnetic applications*; Cambridge University Press, New York, 441 p.
- Cella F., Fedi M. and Florio G., 2009, *Toward a full multiscale approach to interpret potential fields*: Geophysical Prospecting 57, 543–557.
- Cella, F. and Fedi, M., 2012, *Inversion of potential field data using the structural index as weighting function rate decay*. Geophysical Prospecting. 60, 313-336.
- Cribb J. B., 1976; *Application of the generalized linear inverse to the inversion of static potential data*. Geophysics, VOL. 41, no. 6, 1365-1369;
- Fedi M., and Abbas M.A., 2013, *A fast interpretation of self-potential data using the depth from extreme points method*: Geophysics, 78, no. 2, E107-E116.
- Fedi M. and Pilkington M., 2012: *Understanding imaging methods for potential field data*. Geophysics, 77, 1, G13-G24
- Fedi, M., Florio, G. and Paoletti, V., 2015, *MHODE: a local-homogeneity theory for improved source-parameter estimation of potential fields*: Geophys. J. Int., 202 (2): 887-900 doi:10.1093/gji/ggv185
- Fedi M., Cella F., Quarta T., Villani A., 2010, *2D continuous wavelet transform of potential fields due to extended source distributions*. Appl. Comput. Harmon. Anal.; 28(3):320-337.
- Fedi M. and Cascone L., 2011, *Composite continuous wavelet transform of potential fields with different choices of analyzing wavelets*. J. geophys. Res. 2011;116(B7). doi:10.1029/2010JB007882.
- Fedi M., Cella F., Florio G. and Rapolla A., 2005. *Multiscale derivative analysis of the gravity and magnetic fields of Southern Apennines (Italy)*. In: "CROP Project, Deep seismic exploration of the Central Mediterranean and Italy (Atlases in Geoscience, Volume 1)", I. Finetti, ed., Elsevier Science, 281-318..
- Fedi M. and Florio G., 2006, *SCALFUN: 3D analysis of potential field scaling function to determine independently or simultaneously Structural Index and depth to source*. 76° SEG Annual Meeting, New Orleans, 1-6 October, 2006, pp. 963-967.
- Fedi, M., 2007, *DEXP: a fast method to determine the depth and the structural index of potential fields sources*. Geophysics 72, I1-I11.
- Fedi, M., Florio G., Paoletti, V., 2012, *Local homogeneity of potential fields and fractional homogeneous functions: a new theory for improved source parameter estimation.* 82° SEG Annual Meeting, Las Vegas.
- Florio G., Fedi M., Cella F. & Rapolla A., 1999, *The Campanian Plain and Phlegrean Fields: structural setting from potential field data*. Journal of Volcanology and Geothermal Research 91, 361–379.
- Florio G., Fedi M., Rapolla A., 2009, *Interpretation of regional aeromagnetic data by the scaling function method: the case of Southern Apennines (Italy)*. Geophysical Prospecting, 57, 479-489.

- Gill, P. E., Murray, W., Ponceleon, D. B., and Saunders, M., 1991, *Solving reduced KKT systems in barriermethods for linear and quadratic programming*. Technical Report SOL 91–7, Stanford University.
- Kearey P., Brooks M. and Hill I., 2002, *An Introduction to Geophysical Exploration*. Blackwell Publishing, Oxford.
- Li, Y. and Oldenburg, D. W., 1996, *3-D inversion of magnetic data*. Geophysics, 61, no. 02, 394-408.
- Li Y., and Oldenburg D., 1998, *3D inversion of gravity data*: Geophysics, 63, 109–119.
- Li Y., and Oldenburg D., 2003, *Fast inversion of large-scale magnetic data using wavelet transform and logarithmic barrier method*: Geophysical Journal International, 152, 251-265.
- Menke, W., 1989, *Geophysical data analysis: Discrete inverse theory*; Academic Press
- Oldenburg and Li 1994 Oldenburg, D. W., and Y. Li, 1994, *Subspace linear inverse method*, Inverse Problems, 10, 915 - 935.
- Oldenburg, D. W., and Y. Li, 2005, *Inversion for applied geophysics: A tutorial*, in D. K. Butler, ed., Near-surface geophysics: SEG, 89-150.
- Pilkington, M., 2009, *3D magnetic data-space inversion with sparseness constraints*. Geophysics, 74; no. 01; P. L7-L15.
- Pilkington, M. and Roest, W., 1992, *Draping aeromagnetic data in areas of rugged topography*, J. Appl. Geophys. 29 (1992), 135–142.
- Pilkington, m., 1997, *3D magnetic imaging using conjugate gradients*, Geophysics, 62, 1132-1142.
- Rapolla, A., M. Fedi, and G. Fiume, 1989, *Crustal structure of e Ischia Phlegrean fields geoermal area, near Naples (Italy), from gravity and aero-magnetic data*: Geophysical Journal, 97, 409–419.
- Reid, A. B., J. M. Allsop, H. Granser, A. J. Millett, and I. W. Somerton, 1990, *Magnetic interpretation in ree dimensions using Euler deconvolution*: Geophysics, 55, 80–91.
- Reynolds J. M., 1997, *An introduction to applied and environmental geophysics*, John Wiley & Sons Ltd, Chichester, West Sussex.
- Sailhac, P., and D. Gibert, 2003, *Identification of sources of potential fields with the continuous wavelet transform: Two-dimensional wavelets and multi-polar approximations*: Journal of Geophysical Research, 108, B5 2262.
- Stavrev, P. Y., 1997, *Euler deconvolution using differential similarity transformations of gravity or magnetic anomalies*: Geophysical Prospecting, 45, 207–246.
- Zhdanov, M. S., 2002, *Geophysical inverse theory and regularization problems*, Elsevier Science.

Appendix

DEXP transform and N(x,z) function mathematical computation

We have calculated analytically the gravimetric field, the DEXP transform and the *N(z)* function related to "finite vertical cylinder"-shape sources analysed in chapter 4.

We have used the Symbolic Math Toolbox™, which provides functions for solving and manipulating symbolic math expressions and performing variable-precision arithmetic. The computations are performed defining a special data type: symbolic objects, so integration, differentiation, simplification, equation solving, and other mathematical tasks can be performed increasing usual numeric capabilities. Symbolic results can be than converted to numeric results and plotted as shown in the following pictures.

A finite vertical cylinder

The gravity field of a finite vertical cylinder is a simple inhomogenous potential field (Fedi et al., 2012). For a cylinder extended from z_{01} to z_{02}, the gravity field can be expressed as the difference between the fields of two infinite vertical cylinders, whose tops are placed respectively at z_{01} and z_{02}.

If we suppose that the sources have unitary density and radius, and that the gravitational constant is equal to 1 we can expresse the gravity field of the two infinite vertical cylinders as:

$$V_1 = -2\pi \frac{1}{r_1} \qquad \textbf{(A.1)}$$

and

$$V_2 = -2\pi \frac{1}{r_2} \qquad \textbf{(A.2)}$$

where

$$r_1 = \sqrt{(x - x_0)^2 + (y - y_0)^2 + (z - z_{01})^2} \qquad \textbf{(A.3)}$$

and

$$r_2 = \sqrt{(x - x_0)^2 + (y - y_0)^2 + (z - z_{02})^2}$$

So the difference between the two can be expressed as:

$$f = -2\pi \left(\frac{1}{r_1} - \frac{1}{r_2} \right) \qquad \textbf{(A.4)}$$

Symbolic calculation of the gravity field of two infinite vertical cylynders, and of a finite vertical cylinder, which is the combination of the two, have been converted to numeric results and shown in Figure A1.

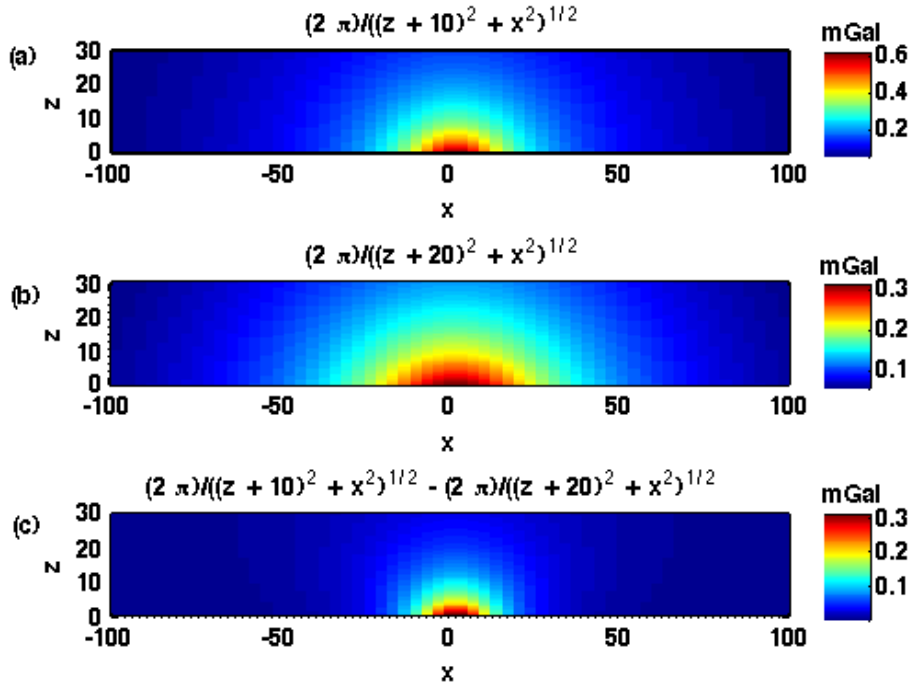

Figure A1 – (a) gravimetric anomaly of an infinite vertical cylinder with top placed at z = 10 (lenght units), (b) gravimetric anomaly of an infinite vertical cylinder with top placed at z = 20, (c) gravimetric anomaly of a finite vertical cylinder with top placed at z = 10 and bottom placed at z = 20.

In the same way we can compute the DEXP transform of a finite vertical cylinder, starting from the simple expressions of the DEXP of two infinite vertical cylinders:

$$W_1 = V_1 \cdot z^{0.5} \qquad \textbf{(A.5)}$$

and

$$W_2 = V_2 \cdot z^{0.5} \qquad \textbf{(A.6)}$$

where z is the continuaton height and 0.5 is the scaling exponent from Table 3.1, and then computing the difference between the two:

$$W = W_1 - W_2 = \left(-2\pi \left(\frac{1}{r_1} - \frac{1}{r_2} \right) \right) \cdot z^{0.5} \qquad \textbf{(A.7)}$$

Figure A2 shows how equations A.5-7 can be converted into numerical results.

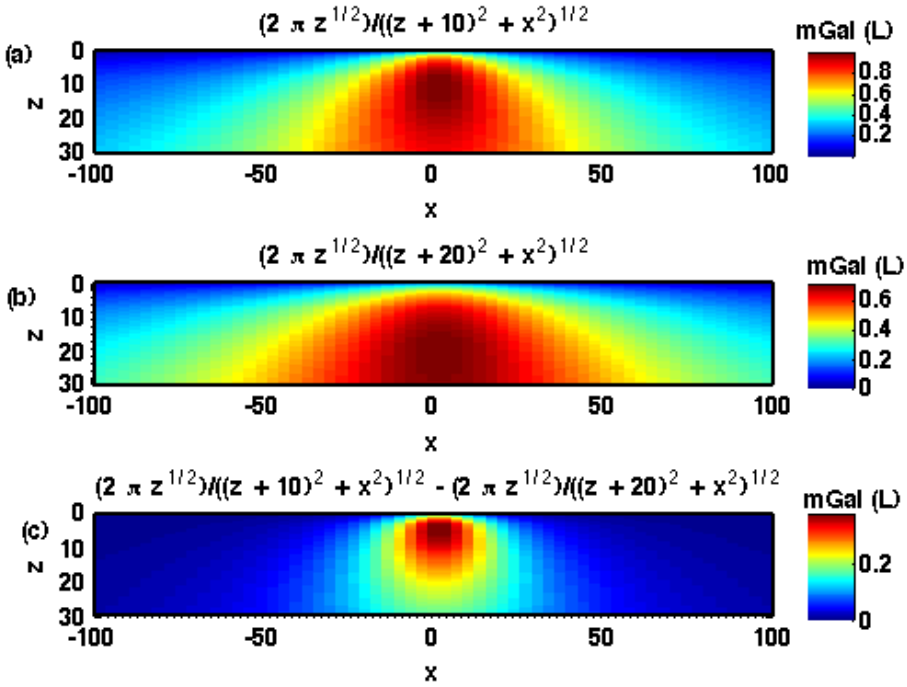

Figure A2 - (a) DEXP transform of the gravimetric anomaly of an infinite vertical cylinder with top placed at z = 10 (lenght units), (b) DEXP transform of the gravimetric anomaly of an infinite vertical cylinder with top placed at z = 20, (c) DEXP transform of the gravimetric anomaly of a finite vertical cylinder with top placed at z = 10 and bottom placed at z = 20.

The *N(x,z)* function can be computed from the DEXP result as follows:

$$N(x,z) = -2\left(\frac{\log(W(x,z))}{\log(z)}\right) \qquad \textbf{(A.8)}$$

and its numerical results is shown in Figure A3.

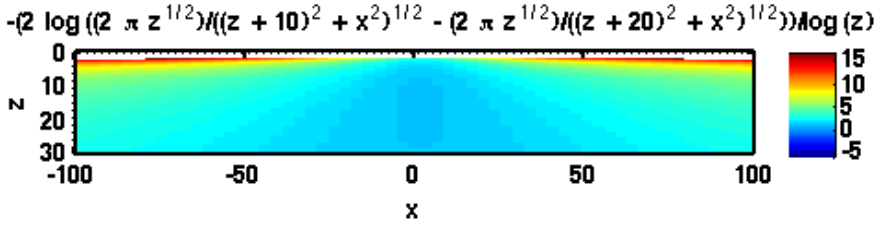

Figure A3 – *N(z)* function from the DEXP transform of the gravimetric anomaly of a finite vertical cylinder with top placed at z = 10 and bottom placed at z = 2

Two finite vertical cylinders

Starting from the gravimetric anomaly, DEXP transform and N(z) index of a finite vertical cylinder, we have re-arranged Equations A1-to-8 to calculate the field of two finite vertical cylinders following the well known principle of superposition.

The symbolic results, converted to numeric results are shown in the following pictures.

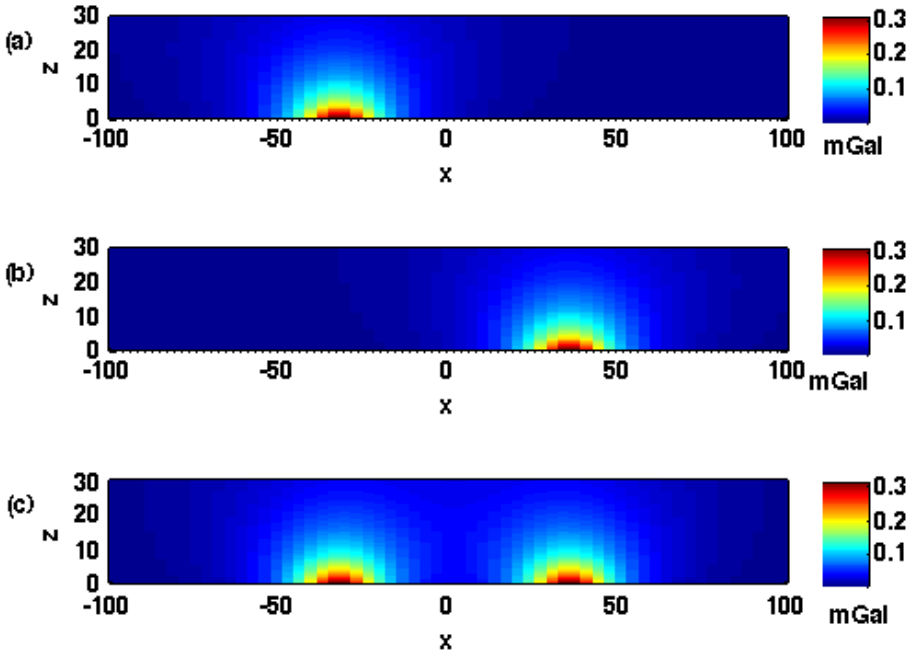

Figure A4 - (a) gravimetric anomaly of a finite vertical cylinder with top placed at z = 10 (lenght units), bottom placed at z = 20 and center placed at x = - 30, (b) gravimetric anomaly of a finite vertical cylinder with top placed at z = 10, bottom placed at z = 20 and center placed at x = 30, (c) gravimetric anomaly of two finite vertical cylinders with tops placed at z = 10, bottoms placed at z = 20 and centres places at x = -30 and x = 30 respectively.

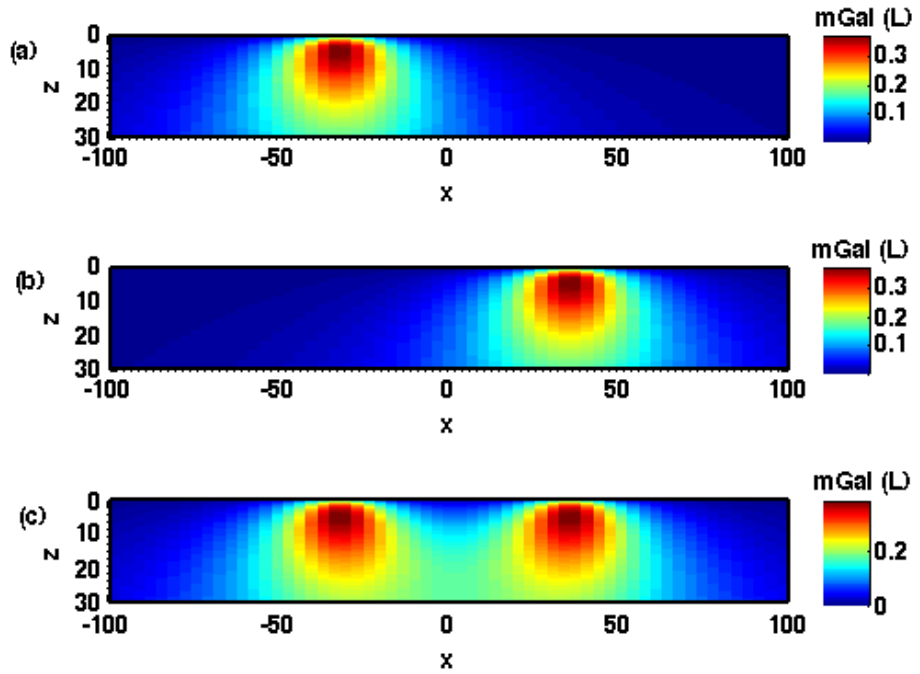

Figure A5 - (a) DEXP transform of the gravimetric anomaly of a finite vertical cylinder with top placed at z = 10 (lenght units), bottom placed at z = 20 and center placed at x = - 30, (b) DEXP transform of the gravimetric anomaly of a finite vertical cylinder with top placed at z = 10, bottom placed at z = 20 and center placed at x = 30, (c) DEXP transform of the gravimetric anomaly of two finite vertical cylinders with tops placed at z = 10, bottoms placed at z = 20 and centres places at x = -30 and x = 30 respectively.

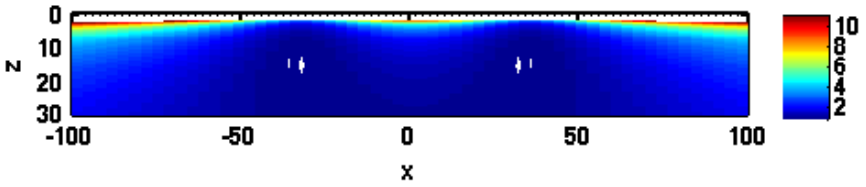

Figure A6 - *N(z)* function from the DEXP transform of the gravimetric anomaly of two finite vertical cylinders with tops placed at z = 10, bottoms placed at z = 20 and centres places at x = -30 and x = 30 respectively.

Two interferent finite vertical cylinders

We have also calculated the gravimetric anomaly generated by two finite vertical cylinders, whose contribute heavily interferes with the other, as it is not possible to distinguish the sources-related maxima on the anomaly.

The symbolic results, converted to numeric results are shown in the following pictures.

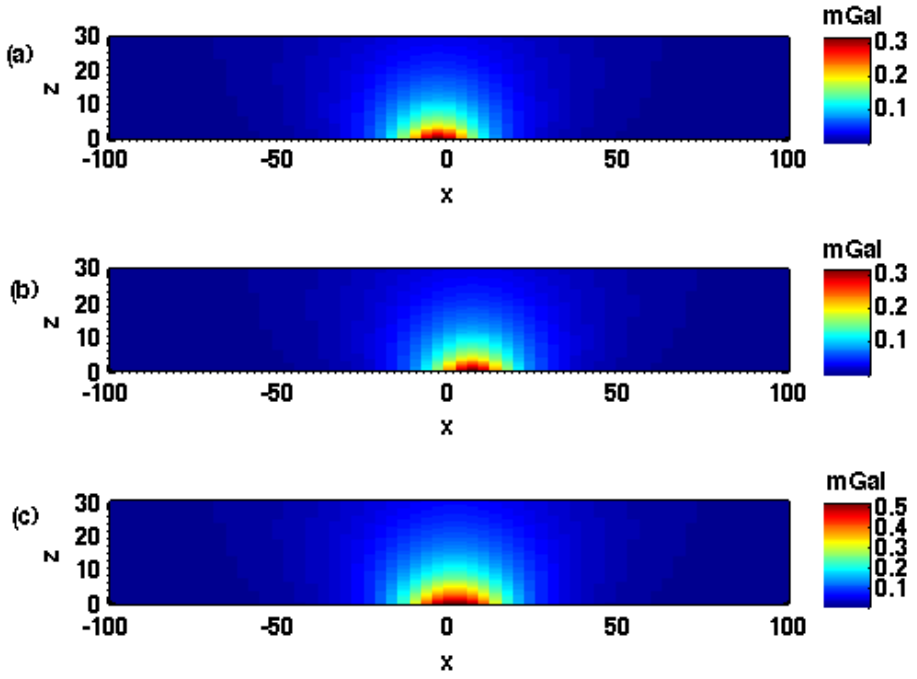

Figure A7 - (a) gravimetric anomaly of a finite vertical cylinder with top placed at z = 10 (lenght units), bottom placed at z = 20 and center placed at x = - 10, (b) gravimetric anomaly of a finite vertical cylinder with top placed at z = 10, bottom placed at z = 20 and center placed at x = 10, (c) gravimetric anomaly of two finite vertical cylinders with tops placed at z = 10, bottoms placed at z = 20 and centres places at x = -10 and x = 10 respectively.

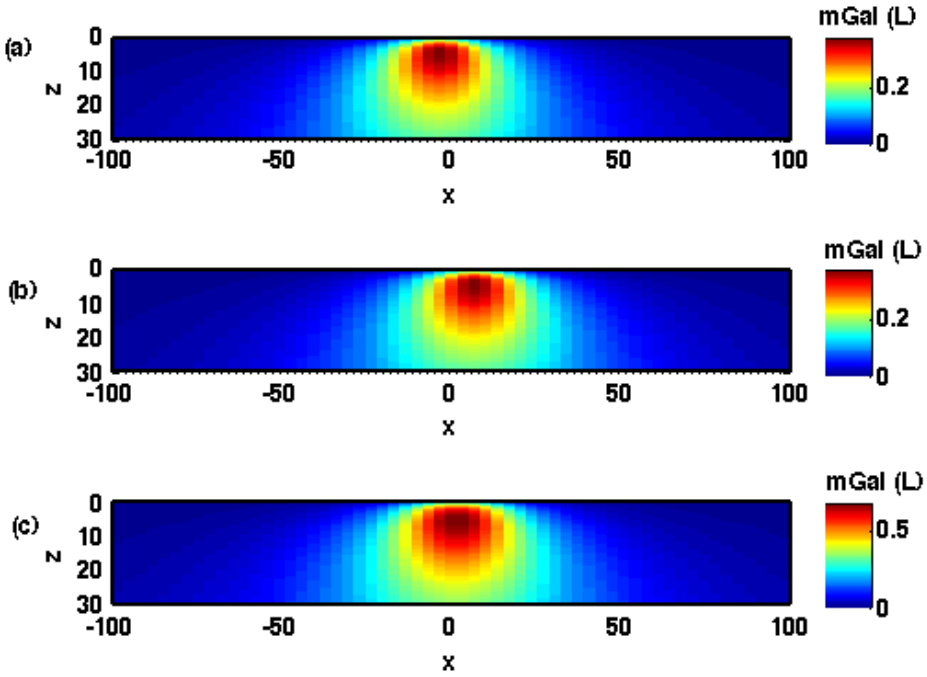

Figure A8 - (a) DEXP transform of the gravimetric anomaly of a finite vertical cylinder with top placed at z = 10 (lenght units), bottom placed at z = 20 and center placed at x = - 10, (b) DEXP transform of the gravimetric anomaly of a finite vertical cylinder with top placed at z = 10, bottom

placed at z = 20 and center placed at x = 10, (c) DEXP transform of the gravimetric anomaly of two finite vertical cylinders with tops placed at z = 10, bottoms placed at z = 20 and centres places at x = -10 and x = 10 respectively.

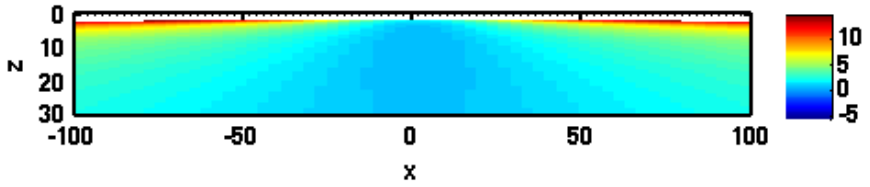

Figure A9 - N(z) function from the DEXP transform of the gravimetric anomaly of two finite vertical cylinders with tops placed at z = 10, bottoms placed at z = 20 and centres places at x = -10 and x = 10 respectively.

Two deeper interferent finite vertical cylinders

The following pictures show, instead, the symbolic results, converted to numeric results, of the gravimetric anomaly generated by two deeper finite vertical cylinders, whose contribute heavily interferes with the other, as it is not possible to distinguish the sources-related maxima on the anomaly.

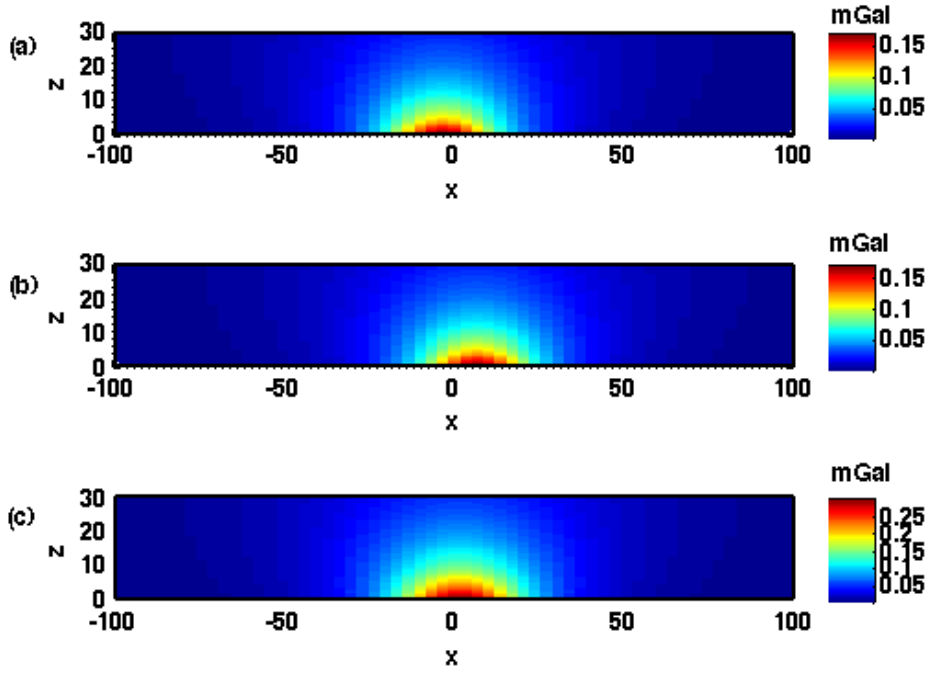

Figure A10 - (a) gravimetric anomaly of a finite vertical cylinder with top placed at z = 15 (lenght units), bottom placed at z = 25 and center placed at x = - 15, (b) gravimetric anomaly of a finite vertical cylinder with top placed at z = 15, bottom placed at z = 25 and center placed at x = 10, (c) gravimetric anomaly of two finite vertical cylinders with tops placed at z = 15, bottoms placed at z = 25 and centres places at x = -10 and x = 10 respectively.

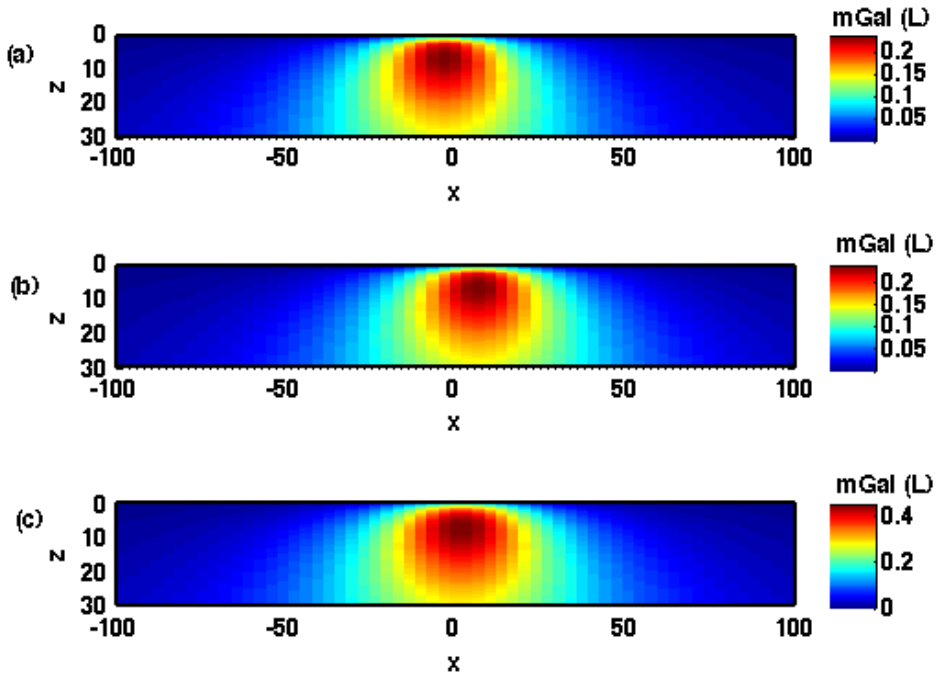

Figure A11 - (a) DEXP transform of the gravimetric anomaly of a finite vertical cylinder with top placed at z = 15 (lenght units), bottom placed at z = 25 and center placed at x = - 10, (b) DEXP transform of the gravimetric anomaly of a finite vertical cylinder with top placed at z = 15, bottom placed at z = 25 and center placed at x = 10, (c) DEXP transform of the gravimetric anomaly of two finite vertical cylinders with tops placed at z = 15, bottoms placed at z = 25 and centres places at x = -10 and x = 10 respectively

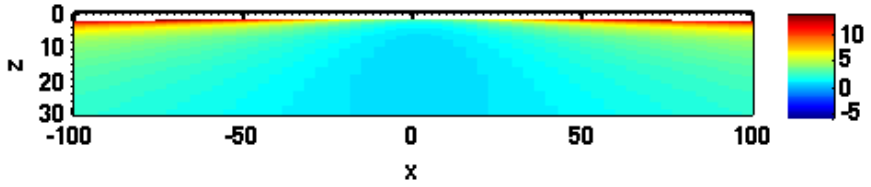

Figure A12 - N(z) function from the DEXP transform of the gravimetric anomaly of two finite vertical cylinders with tops placed at z = 15, bottoms placed at z = 25 and centres places at x = -10 and x = 10 respectively.

Two interferent finite vertical cylinders at different depths

The case of two interferent finite vertical cylinders has been made harder to interpret placing the sources at different depth from each others.We have calculated the gravimetric anomaly, DEXP transform and *N(z)* function also for this case.

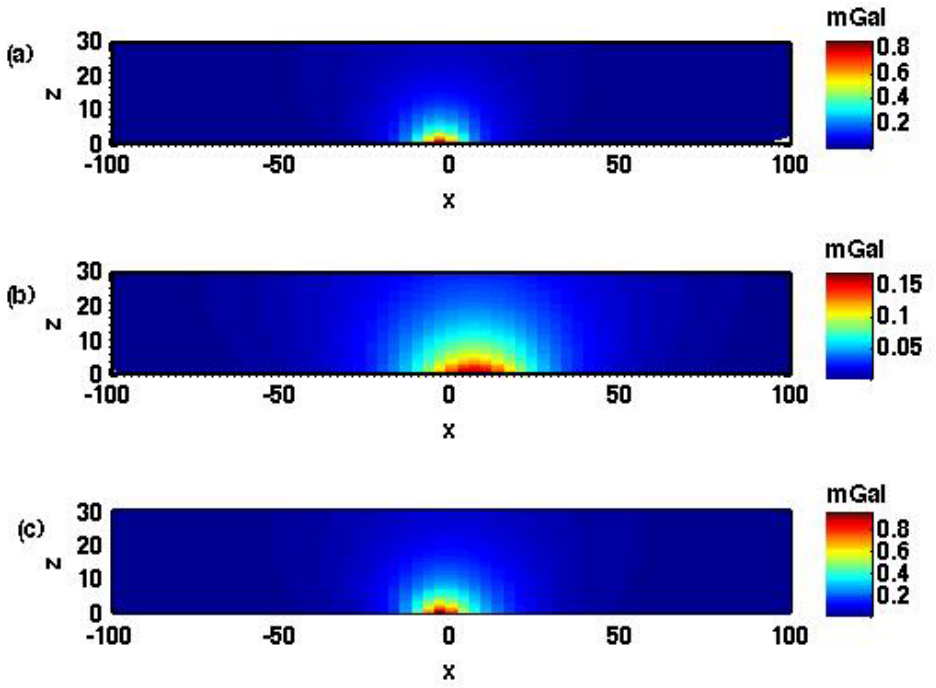

Figure A13 - (a) gravimetric anomaly of a finite vertical cylinder with top placed at z = 5 (lenght units), bottom placed at z = 15 and center placed at x = - 15, (b) gravimetric anomaly of a finite vertical cylinder with top placed at z = 15, bottom placed at z = 25 and center placed at x = 10, (c) gravimetric anomaly of the two finite vertical cylinders in (a) and (b).

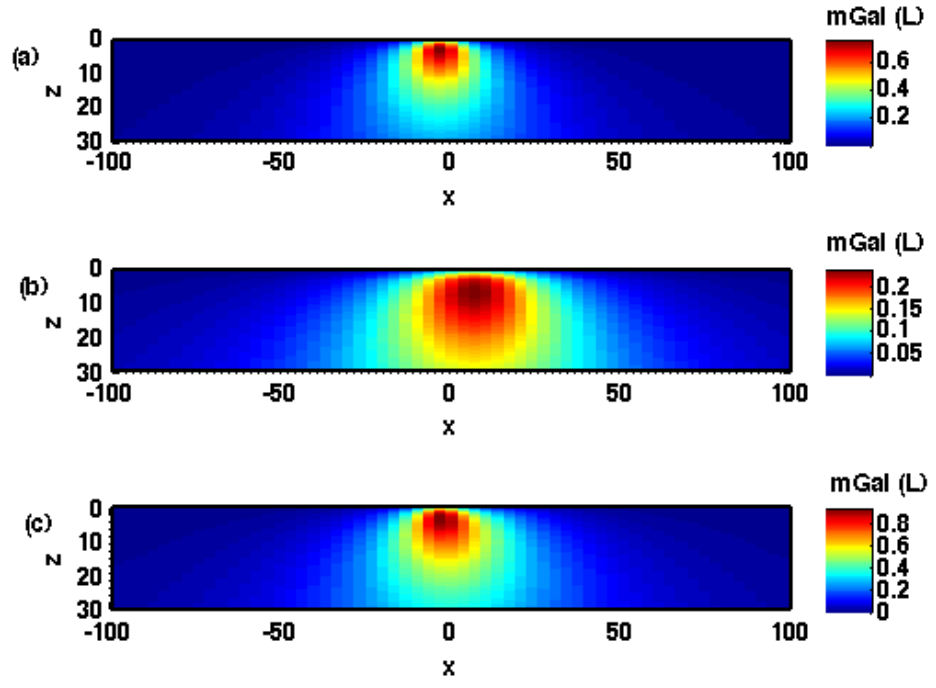

Figure A14 - (a) DEXP transformn of the gravimetric anomaly of a finite vertical cylinder with top placed at z = 5 (lenght units), bottom placed at z = 15 and center placed at x = - 15, (b) DEXP transformn of the gravimetric anomaly of a finite vertical cylinder with top placed at z = 15, bottom

placed at z = 25 and center placed at x = 10, (c) DEXP transformn of the gravimetric anomaly of the two finite vertical cylinders in (a) and (b).

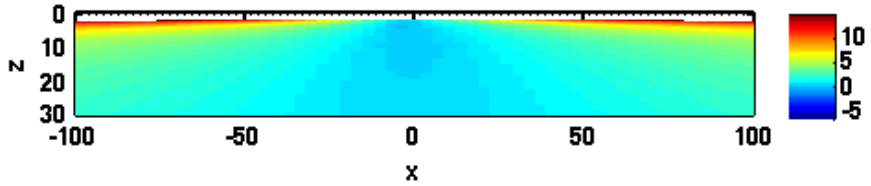

Figure A15 – N(z) function from the DEXP trasnform of the gravimetric anomaly of two finite vertical cylinders in Fig. A13(c).

Papers

Journal of Applied Geophysics 111 (2014) 346–355

Contents lists available at ScienceDirect

Journal of Applied Geophysics

journal homepage: www.elsevier.com/locate/jappgeo

Volume Continuation of potential fields from the minimum-length solution: An optimal tool for continuation through general surfaces

Daniela Mastellone, Maurizio Fedi, Simone Ialongo, Valeria Paoletti *

Dipartimento di Scienze della Terra, dell'Ambiente e delle Risorse, University of Naples Federico II, Largo S. Marcellino 10, IT-80138 Naples, Italy

ARTICLE INFO

Article history:
Received 6 May 2014
Accepted 23 October 2014
Available online 1 November 2014

Keywords:
Upward continuation
Potential fields
Inversion
Minimum-length solution

ABSTRACT

Many methods have been used to upward continue potential field data. Most techniques employ the Fast Fourier transform, which is an accurate, quick way to compute level-to-level upward continuation or spatially varying scale filters for level-to-draped surfaces. We here propose a new continuation approach based on the minimum-length solution of the inverse potential field problem, which we call *Volume Continuation* (VOCO). For real data the VOCO is obtained as the regularized solution to the Tikhonov problem. We tested our method on several synthetic examples involving all types of upward continuation and downward continuation (level-to-level, level-to-draped, draped-to-level, draped-to-draped). We also employed the technique to upward continue to a constant height (2500 m a.s.l.), the high-resolution draped aeromagnetic data of the Ischia Island in Southern Italy. We found that, on the average, they are consistent with the aeromagnetic regional data measured at the same altitude. The main feature of our method is that it does not only provide continued data over a specified surface, but it yields a volume of upward continuation. For example, the continued data refers to a volume and thus, any surface may be easily picked up within the volume to get upward continuation to different surfaces. This approach, based on inversion of the measured data, tends to be especially advantageous over the classical techniques when dealing with draped-to-level upward continuation. It is also useful to obtain a more stable downward continuation and to continue noisy data. The inversion procedure involved in the method implies moderate computational costs, which are well compensated by getting a 3D set of upward continued data to achieve high quality results.

1. Introduction

Upward continuation is used to transform anomalies measured at a surface into anomalies that would be measured at some higher altitude surface. It can also be used to merge data at different altitudes, such as, e.g., those measured on irregular surfaces (i.e. in case of draped airborne surveys) and to continue the whole dataset to a given surface (e.g., Paoletti et al., 2004, 2005; Paterson et al., 1990; Pilkington and Roest, 1992; Ridsdill-Smith, 2000). This transformation is also helpful to enhance the effects of deep sources, as it attenuates the highest frequency content of the signal, which is usually associated to shallow sources. Finally, multiscale methods such as the continuous wavelet transform (Fedi and Cascone, 2011; Fedi et al., 2010; Mauri et al., 2010; Sailhac et al., 2009), the DEXP transformation (Fedi, 2007) and the multiridge analysis (Cella et al., 2009) involve potential field data available on a 3D volume, which in turn is generated by upward continuation of data measured at a single – flat or draped – surface.

Upward continuation originates from Green's third identity (Blakely, 1996), which states that if U is a harmonic continuous function, with continuous derivatives through a regular region R, then its value at any point P within the harmonic region R, can be evaluated from its behaviour on the boundary S:

$$U(P) = \frac{1}{4\pi}\int_S \left(\frac{1}{r}\frac{\partial U}{\partial n} - U\frac{\partial}{\partial n}\frac{1}{r}\right) dS \tag{1}$$

where n is the outward normal direction, r the distance from P to the point of integration on S. No information about the source is needed except that it is not located within the region R.

In the following, we will describe the four types of performing upward continuation: level-to-level, level-to-draped, draped-to-level and draped-to-draped. The simplest case is the level-to-level upward continuation, when the potential field data is measured on a constant altitude surface z_0 and continued to some higher altitude plane. The process is defined by an integral formulation:

$$U(x, y, z_0 - \Delta z) = \frac{\Delta z}{2\pi}\int_{-\infty}^{+\infty}\int_{-\infty}^{+\infty} \frac{U(x', y', z_0)}{\left[(x-x')^2 + (y-y')^2 + \Delta z\right]^{3/2}} dx' dy' \tag{2}$$

* Corresponding author. Tel.: +39 812538149.
E-mail address: paoletti@unina.it (V. Paoletti).

http://dx.doi.org/10.1016/j.jappgeo.2014.10.020
0926-9851/

where $\Delta z > 0$, and z is assumed negative outward. Eq. (2) is a convolution integral and can be solved via the Fourier transform and the convolution theorem. The numerical implementation of this formula obviously considers a finite-extent dataset and equally spaced data, which leads to known types of errors for the continued data (Fedi et al., 2012). Upward continued data can be calculated by convolution in either the space domain or the Fourier domain. In this last domain, the Fourier transform of the data is simply multiplied by the frequency operator:

$$e^{-|\mathbf{k}|\Delta z} \quad \Delta z>0 \tag{3}$$

where $\mathbf{k}$ is the wavenumber vector. As said before, real data is discrete and refers to a finite survey area. Thus, when using circular convolution to calculate upward continuation in the frequency domain, aliasing errors can affect the low-frequency content of upward continued data. These errors can be reduced by performing the Fourier transform on a larger dataset, which extends outside the survey area (Fedi et al., 2012; Oppenheim and Schafer, 1975). The enlarged dataset may be built utilizing data from other surveys or through extrapolation algorithms: zero-padding and symmetric extension (Fedi et al., 2012), maximum entropy extension (Gibert and Galdéano, 1985) and others.

Eqs. (2) and (3) are strictly valid for level-to-level continuations; however potential field literature is rich in algorithms performing upward continuation between uneven surfaces. Among them, Cordell (1985), Pilkington and Roest (1992) and Ridsdill-Smith (2000) developed algorithms for level-to-draped upward continuation. Whereas, Xia et al. (1993), Meurers and Pail (1998), Fedi et al. (1999), Ridsdill-Smith (2000) and Wang (2006) formulated upward continuation algorithms for draped-to-level surfaces.

In this paper we define a new approach that performs upward continuation using the relation established by Cribb (1976) between the minimum-length solution of the inverse potential field problem and upward continuation. We call this method Volume Upward Continuation (VOCO) as this approach has the advantage of generating the field as a unique solution in a 3D volume, in which all four types of continuations (level-to-level, level-to-draped, draped-to-level and draped-to-draped) are naturally defined.

As known, inversion implies higher computational costs than standard continuation algorithms. They are however, well compensated by the versatility of the method in providing from a single inversion, the continuation along any desired surface inside the source volume and by the high-quality of the continuation.

2. Volume Upward Continuation of potential fields

2.1. Theoretical background

As described in the following, the Volume Upward Continuation of a magnetic field is computed by: i) inverting the magnetic anomaly to obtain the minimum-length solution; and ii) converting the magnetization volume into an upward continued field volume.

The inverse problem for potential fields (e.g., Fedi et al., 2005) can be formulated by the following integral:

$$f(\mathbf{r}) = \int_V K(\mathbf{r},\mathbf{r}_0)M(\mathbf{r}_0)d\mathbf{r}_0^3 \tag{4}$$

where $f(\mathbf{r})$ is the potential field measured at the point $\mathbf{r}$, $M(\mathbf{r}_0)$ is the unknown source distribution in the volume Ω and $K(\mathbf{r},\mathbf{r}_0)$ is the kernel. In the case of the magnetic field we will denote $f = \Delta T$ and consider K as the field measured at a distance $\mathbf{r}$ given by a magnetic dipole with unit-magnetization at the point $\mathbf{r}_0$.

The kernel K can be expressed as:

$$K(\mathbf{r},\mathbf{r}_0) = \frac{\mu_0}{4\pi}\frac{\partial^2}{\partial n \partial t}\frac{1}{\|\mathbf{r}-\mathbf{r}_0\|_2} \tag{5}$$

where μ_0 is the magnetic permeability of free space, $\mathbf{t}$ and $\mathbf{n}$ are unit-vectors along the inducing field and magnetization vectors, and $\|\mathbf{r}-\mathbf{r}_0\|_2$ denotes the Euclidean norm of $\mathbf{r}-\mathbf{r}_0$.

Discretizing the volume Ω in an $N_x \times N_y \times N_z$ grid of blocks, assuming that the magnetization is a piecewise function constant in each cell Ω_j, we can write a linear system of equations, calculating expression (5) in each cell. In this way we will get $P = N_x \times N_y$ equations (one for each measurement point). Every equation will then have $N = N_x \times N_y \times N_z$ unknowns leading to the linear system:

$$\mathbf{Km} = \mathbf{d} \tag{6}$$

where $\mathbf{K}$ is the kernel coefficients matrix and $\mathbf{d}$ is the measured data vector. The coefficient matrix $\mathbf{K}$ has elements given by the expression:

$$K_{ij} = \int_{\Omega_j} K(\mathbf{r},\mathbf{r}_0)d\mathbf{r}_0^3 \qquad i = 1,\ldots,P, \qquad j = 1,\ldots,N. \tag{7}$$

The simplest solution of such an under-determined inverse problem is the one minimizing the Euclidean norm of the solution $\mathbf{m}$: $\left(\sum_{i=1}^{N}|m_i|^2\right)^{1/2}$. This is called minimum-length solution (Menke, 1989):

$$\mathbf{m} = \mathbf{K}^T\left(\mathbf{K}\mathbf{K}^T\right)^{-1}\mathbf{d}. \tag{8}$$

In order to obtain an upward continued field volume, we can use the relation shown by Cribb (1976). For a vertical direction of both the inducing field and magnetization vectors, Cribb (1976) showed that the Fourier transform of $\mathbf{m}$ could be simply expressed as:

$$F[\mathbf{m}_i] = 4e^{-|\mathbf{k}|h_i}F[\mathbf{d}] \qquad i = 1,\ldots,L \tag{9}$$

where F denotes the Fourier transformation, L is the number of layers, $\mathbf{m}_i$ is the magnetization intensity vector of the ith layer, $\mathbf{h}_i$ is its depth and $\mathbf{k}$ is the wavevector with components k_x, k_y and $(k_x{}^2 + k_y{}^2)^{1/2}$. The important information contained in Eq. (9) is that the Fourier Transform of the ith layer of the magnetization distribution $\mathbf{m}_i$ is directly related to the upward continued field of $\mathbf{d}$, to a distance equal to the opposite of the layer depth: $z_i = -h_i$ (Fedi and Pilkington, 2012). Thus, we can obtain $\mathbf{d}$ by anti-transforming the second member of Eq. (9):

$$\mathbf{d}_{h_i} = \frac{\mathbf{m}_i}{4} \qquad i = 1,\ldots,L\,. \tag{10}$$

This shows that the field at the altitude $z_i = -h_i$ differs only for a numeric constant from the magnetization of the ith layer. We may therefore first compute the minimum-length solution (Eq. (8)), inserting $\mathbf{n} = \mathbf{t} = (0,0,1)$ in the kernel (Eq. (5)), then compute the Volume upward Continuation (VOCO) through Eq. (10). This procedure may therefore be viewed as an effective alternative to common techniques of upward continuation of the magnetic field.

Note that for real data, a regularized solution may be preferable in order to dampen the disturbing error-propagation of the data noise. This may be accomplished not by minimizing the model norm (as in the case of the solution in Eq. (8)), but using the Tikhonov regularization that takes the form:

$$\min_{\mathbf{m}}\left\{\|\mathbf{Km}-\mathbf{d}\|_2^2 + \lambda^2\|\mathbf{m}\|_2^2\right\} \tag{11}$$

where λ is a regularization parameter. Eq. (11) can be solved efficiently by iterative methods such as the conjugate gradient method and its variants (CGLS, LSQR, etc.) (e.g. Hansen, 2010). By solving such regularized problems, we can obtain a solution which is nearly that yielded by Eq. (8) if the signal-to-noise ratio is high, or a more smoothed solution when the signal-to-noise ratio is low. In the latter case, Eq. (10) should be replaced by:

$$\mathbf{d}_{h_i} \cong \frac{\mathbf{m}_i}{4} \qquad i = 1, \ldots, L. \tag{12}$$

Note that the observation surfaces may be either flat or uneven to handle the different cases: flat-to-flat, draped-to-flat, flat-to-draped and draped-to-draped.

In the case of the gravity inverse problem starting from Eq. (4), we will denote $f(\mathbf{r})$ as the gravity field measured at point $\mathbf{r}$, and K as the gravity field measured at distance $\mathbf{r}$, given by a pole with unit-density at point $\mathbf{r}_0$. The kernel K will be expressed as:

$$K(\mathbf{r}, \mathbf{r}_0) = \gamma \frac{\partial}{\partial z} \frac{1}{\|\mathbf{r} - \mathbf{r}_0\|_2} \tag{13}$$

where γ is the gravitational constant. Similar to the magnetic field case, the density distribution of the minimum-length solution may be used to get a VOCO of the gravity field. In this case, according to Cribb (1976), the anomalous density distribution is proportional to the upward continuation of the vertical derivative of the observed data:

$$F[\mathbf{m}_i] = \frac{\mathbf{k} e^{-|\mathbf{k}| h_i}}{\pi \gamma} F[\mathbf{d}] \qquad i = 1, \ldots, L \tag{14}$$

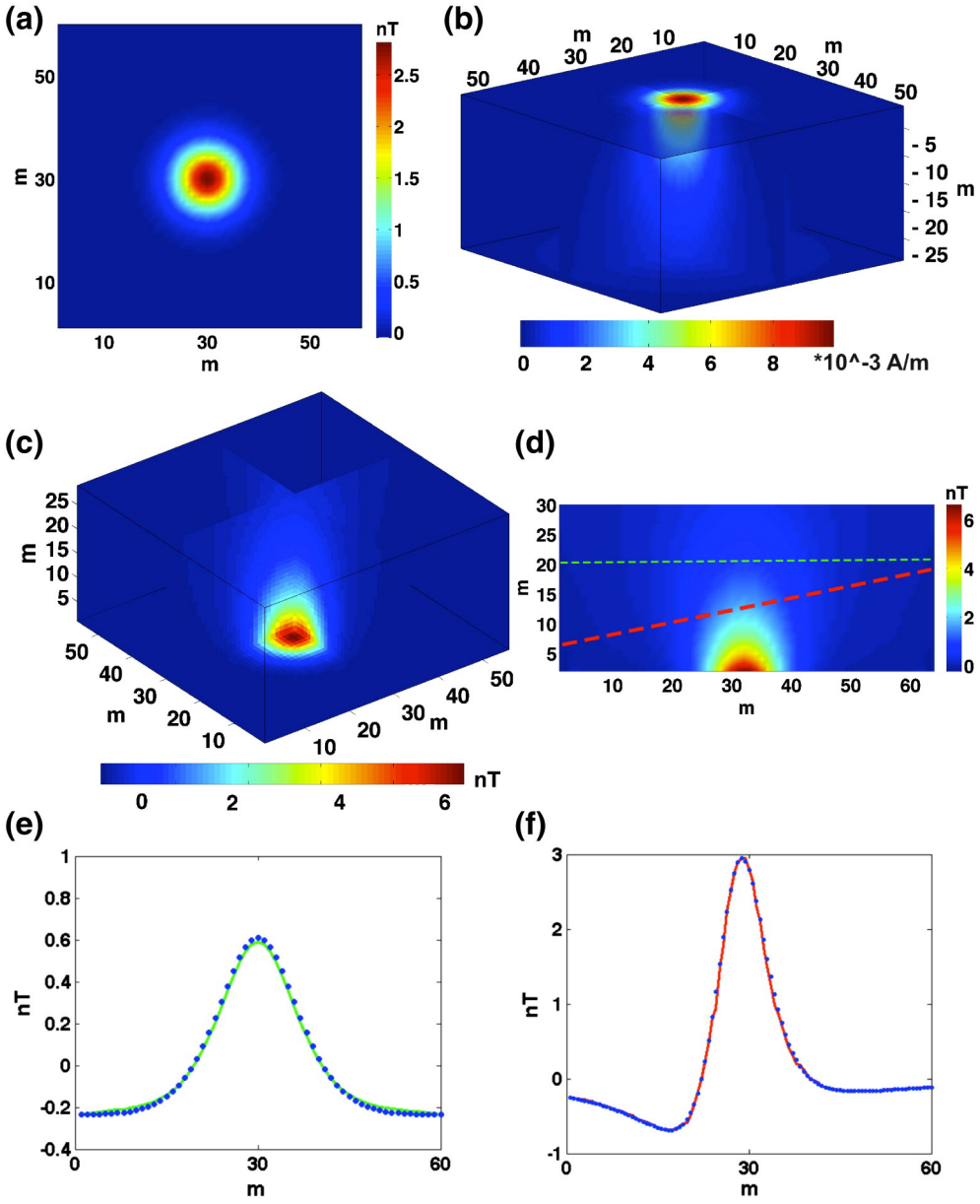

Fig. 1. VOCO flowchart. (a) Synthetic magnetic anomaly due to a horizontal dipole line located at 30 m depth and with 1 A/m magnetization intensity; (b) Magnetization model resulting from minimum-length inversion of the anomaly field in (a); (c) Volume Upward Continuation after transformation of the magnetization model in (b); (d) Vertical section of the VOCO in (c). The green dashed line shows a level at h = 20 m where a level-to-level continuation is extracted (see plot e). The red line shows a dipping level where a level-to-draped continuation is extracted (see plot f); (e)–(f) Comparison between VOCO profiles (green and red lines) and the magnetic anomalies computed at the same levels (blue dots). (For interpretation of the references to colour in this figure legend, the reader is referred to the web version of this article.)

where F denotes the Fourier transformation, L is the number of layers, $\mathbf{m}_i$ is the density vector of the ith layer, $\mathbf{h}_i$ is its depth and $\mathbf{k}$ is the wavevector with components k_x, k_y and $(k_x^2 + k_y^2)^{1/2}$. Therefore the ith layer of the density distribution $\mathbf{m}_i$ is directly related to the upward continued field of the vertical derivative of the data $\mathbf{d}$, to a distance equal to the opposite of the layer depth: $z = -h_i$.

2.2. Method workflow

In order to show the applicability of the VOCO method, we tested it in two simple cases: the level-to-level and level-to-draped upward continuation of the magnetic anomaly of a horizontal dipole-line (Fig. 1a). The source has unitary magnetization intensity and it is located at 30 m depth. In both cases we employed Eq. (8) to perform the minimum-length inversion to obtain a 3D magnetization model (Fig. 1b). Then we applied Eq. (10) for every ith layer of the magnetization domain to transform this volume into an upward-continued-field volume (Fig. 1c). From this field volume, it is then possible to extract any desired surface of data laying on either a flat surface or a draped surface, by linearly interpolating data to find the values of the underlying three-dimensional function VOCO at the points located at the desired altitude.

In the level-to-level case, we extracted the ith layer corresponding to the desired continuation altitude $z = -h_i$ (green line in Fig. 1d). Whereas, in the level-to-draped case we extracted the field corresponding to a dipping surface (red line in Fig. 1d). We note that the VOCO field obtained from the minimum-length solution, reproduces well the anomaly computed at the same levels for both the level-to-level (Fig. 1e) and

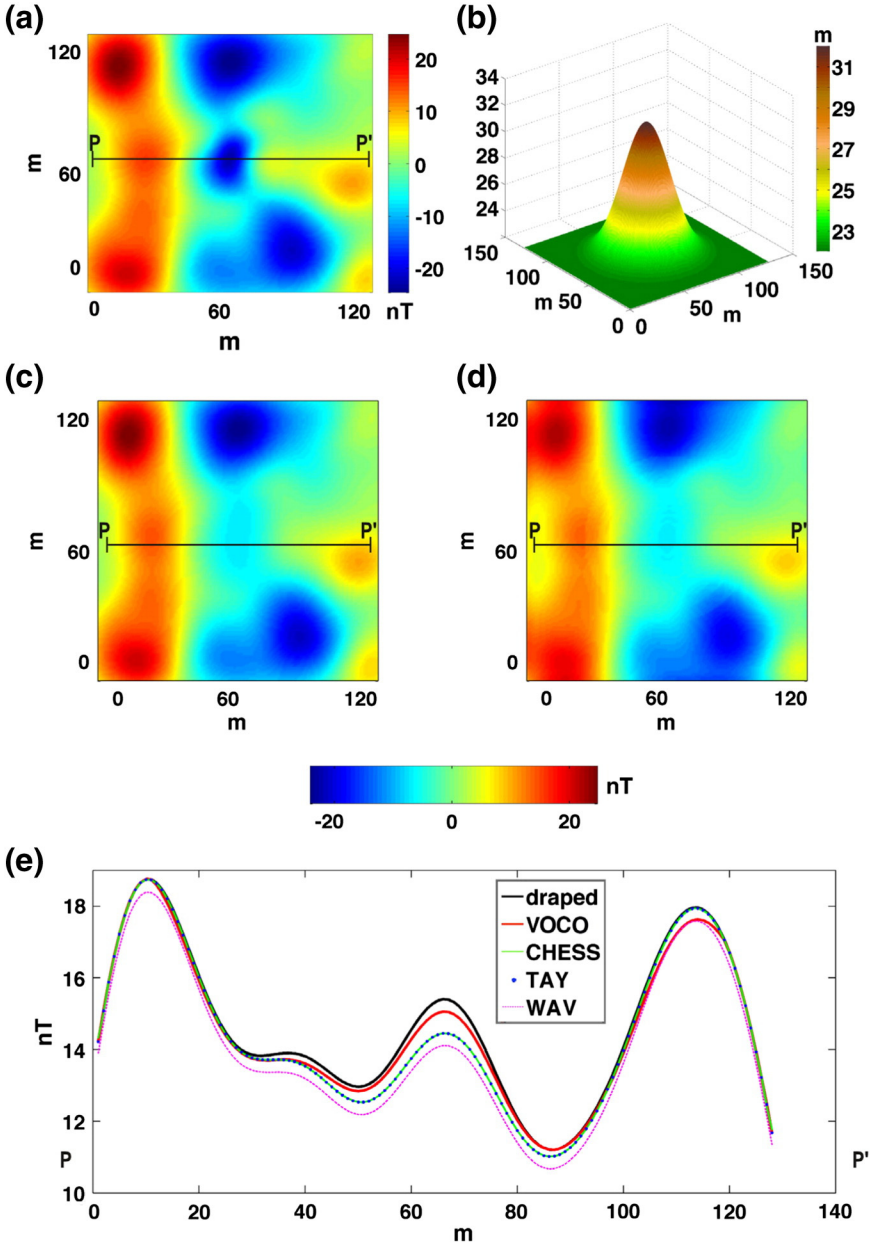

Fig. 2. Level-to-draped upward continuation: (a) synthetic magnetic anomaly computed at $h = 0$ m (from Ridsdill-Smith, 2000). PP′ is the profile along which we compared the performance of VOCO and other methods; (b) Gaussian-shaped topographic surface; (c) synthetic draped magnetic anomaly computed over the topographic surface in (b); (d) VOCO of the magnetic anomaly in (a) converted from the minimum-length solution along the topographic surface in (b), according to Eq. (10); (e) comparison among different level-to-draped upward continuation algorithms along the PP′ profile: black line is data from the synthetic draped magnetic anomaly in (c); red line refers to data from the VOCO in (d); green line, blue dots and magenta line refer to data computed by using the CHESS, TAY and WAV algorithms, respectively. (For interpretation of the references to colour in this figure legend, the reader is referred to the web version of this article.)

the level-to-draped cases (Fig. 1f). We obtained, indeed, a RMSE = 0.0241 nT between the computed field (blue dots in Fig. 1e) and the VOCO (green line in Fig. 1e) for the flat surface case, and a RMSE = 0.0393 nT between the computed field (blue dots in Fig. 1f) and the VOCO (red line in Fig. 1f) for the dipping surface case.

3. Synthetic examples

3.1. Level-to-draped upward continuation

Here we tested the level-to-draped VOCO of a complex synthetic magnetic anomaly and we compared it with the results from other well-tested methods. The magnetic anomaly test in Fig. 2a, originally generated by Ridsdill-Smith (2000) using a magnetization distribution with a power-law decay (i.e., containing more energy at low frequencies than at high frequencies), was draped over the Gaussian-shaped topography in Fig. 2b, yielding the field shown in Fig. 2c. The major field changes are in the central area where, due to the rapid altitude increase of the draped surface, the field amplitude increases nearly to zero. The VOCO (computed through Eqs. (8) and (10)) produced an accurate upward continued field (see Fig. 2d) on the draped surface with RMSE = 0.1818 nT. We obtained the VOCO anomaly from an inversion of a volume of 128 × 128 × 30 cells in about 347 s using a couple of Quad-Core Intel Xeon processors of 2.26 GHz speed each and a 32 GB RAM memory.

We compared the results of the continuation from the VOCO and other algorithms along an E–W profile (PP′ in Fig. 2a). Fig. 2e shows the VOCO anomaly field (red line; RMSE = 0.1818 nT) compared with the computed draped anomaly (black line) and the anomalies produced by other upward continuation algorithms briefly described here.

The Chessboard method (green line; RMSE = 0.3759 nT) (Cordell, 1985) uses a set of different level-to-level upward continuations to generate a 3D volume of data around the sampling points of the desired continuation surface. Also cubic interpolation around values computed on a set of 11 upward continuation levels.

The Taylor series method (blue dots; RMSE = 0.3756 nT) (Pilkington and Roest, 1992) approximates the field on the draped surface using 5 terms of the Taylor-series of the measured field. Such a large number of terms are not always necessary in the Taylor-series expansion as the higher-order derivative terms are generally too noisy to be useful. However, we decided to include these terms to ensure the accuracy of the result.

The upward continuation through the spatially-varying-scale filter (WAV — pink line; RMSE = 0.6544 nT) defined in the wavelet domain (Ridsdill-Smith, 2000) is performed using the Perrier 6 wavelet, n = 54 frequencies and k = 30 scales.

The computational efficiency of each of the methods is similar, but the Taylor-series method can be made more efficient than the other methods by reducing the number of iterations. Neither the Chessboard filter, nor the wavelet methods can be made much faster without a significant reduction in effectiveness.

The VOCO result has the lowest RMSE and provides a good tracking of the original anomaly shape, especially in the central area where the field changes the most. As mentioned, the method performs a level-to-Volume upward Continuation. In this way, the user has the option to choose one or multiple surfaces to extract from the volume after viewing what it looks like, and then makes a choice driven by the specific purpose of the data analysis and/or interpretation.

3.2. Level-to-draped downward continuation

Downward continuation is essentially the inverse process of upward continuation. It allows the calculation of the potential field on a new surface that is located below the observation surface. The frequency response of the level-to-level downward continuation filter is the inverse of the one given in Eq. (3) for upward continuation:

$$e^{-|\mathbf{k}|\Delta z} \quad \Delta z < 0\,. \tag{15}$$

Thus, downward continuation behaves as a high-pass filter and the filter amplitude increases exponentially with frequency. It is well

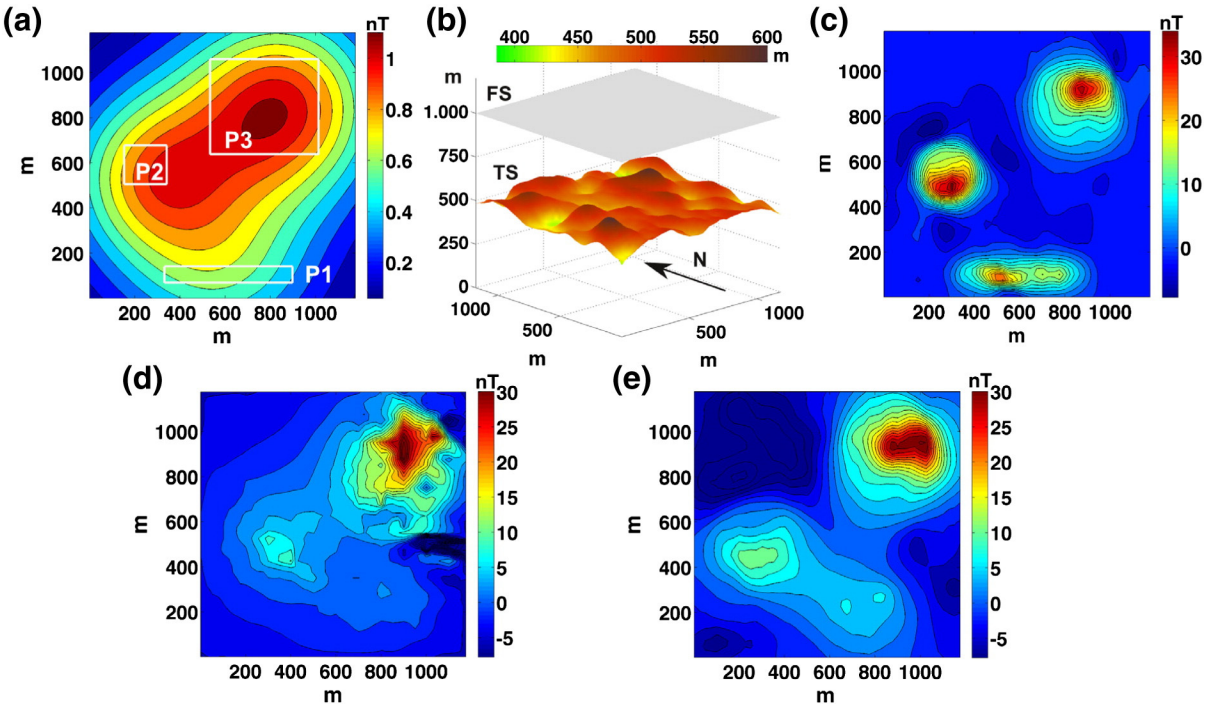

Fig. 3. VOCO applied to downward continuation: (a) magnetic data measured on a flat surface (FS) at 1000 m height. White rectangles outline the *x*–*y* prisms positions; (b) sketch of the acquisition and continuation surfaces; (c) data computed on the topographic surface (TS) shown in plot b; d)–e) results of the downward continuation on the TS surface from WAV (d) and VOCO (e).

Table 1
Source parameters for the magnetic anomaly in Fig. 3a. Depths are referred to the sea level z = 0 m.

	x_1 (m)	x_2 (m)	y_1 (m)	y_2 (m)	Depth (m)	Magnetization intensity (A/m)
P1	375	875	125	150	−250	1
P2	250	375	500	625	−275	1
P3	750	1000	750	1000	−325	0.5

known that downward continuation is an extremely unstable field transformation and any high-frequency noise component in the measured signal is exponentially amplified. We applied the VOCO method to the downward continuation problem of a synthetic anomaly (Fig. 3a), computed 1000 m above the ground (Fig. 3b). The source model consists of three prismatic sources of different shapes (white outlines in Fig. 3a) placed at different depths so that their magnetic effects mutually interfere. Table 1 defines the positions of the sources vertices, and their depth and magnetization intensity. The inducing field and magnetization are both vertical.

We decided to downward continue the data from the measurement flat surface FS, located 1000 m above the ground, to a severely rugged topographic surface TS located 200–600 m above the sea level. Fig. 3c–e shows a comparison between the synthetic data computed on the topographic surface TS (Fig. 3c) and the downward continuation results from the wavelet (WAV, RMSE 7.3368 nT, Fig. 3d), and VOCO (RMSE 6.1294 nT, Fig. 3e) methods. Computation time for VOCO was about 1089 s for a volume model discretized in 48 × 48 × 35 cells using an Intel Core 2 Duo processor of 2.4 GHz speed and a 4 GB RAM memory. We are not including the results from the CHESS and TAY algorithms, as we were not able to produce results comparable with WAV and VOCO. Both the CHESS and TAY methods indeed performed very poorly, yielding to very noisy results even when a smoothing was applied. The Chessboard results were calculated using from 11 to 100 continuation levels and a sliding rule filter of orders from 1 to 5. For the Taylor method (Pilkington and Roest, 1992) we used up to 5 terms of the Taylor series expansion and a low-pass smoothing with taper frequencies $\omega_0 = 0.123$ and $\omega_1 = 0.975$ rad for the cosine roll-off filter.

Looking at the maps resulting from the WAV and VOCO methods and at their RMSE values we note that the WAV result is characterized by topography-connected artefacts even when a smoothing factor is added. On the other hand the VOCO field is the less affected by topography-driven effects while also being capable of locating all three sources.

Note that the WAV algorithm incorporates low-pass filtering tools that attenuate the signal's high-frequency components and stabilize the downward continuation operation. In the VOCO case, the downward continued data is extracted from a 3D volume converted into magnetic field units (Eq. (12)) from a magnetization volume which is the solution of the Tikhonov regularized problem (Eq. (11)). As noted in Section 2.1, this kind of inversion yields stable results optimized by a suitable choice of the regularization parameter λ.

3.3. Draped-to-level upward continuation on a real topographic surface

We now show one more application of the VOCO method namely, the case of field data measured on a draped surface (e.g., a topographic

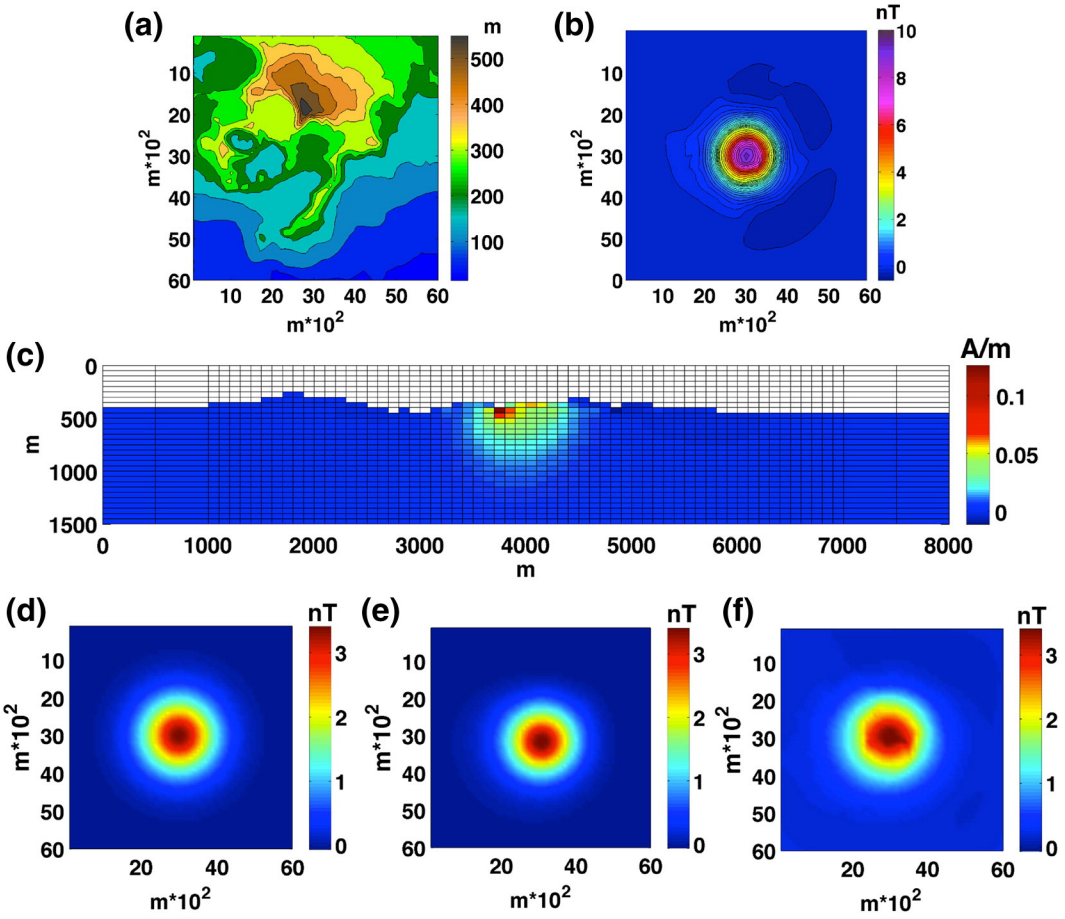

Fig. 4. Draped-to-level-upward continuation on a real topographic surface: (a) real topographic surface located in the area of Naples (Italy); (b) draped synthetic magnetic anomaly of a prismatic source placed at 1 km depth with a magnetization intensity of 5 A/m; (c) minimum-length inversion solution; (d) synthetic magnetic anomaly computed at 600 m altitude; (e) VOCO of the anomaly in (b), extracted at 600 m altitude; (f) WAV upward continuation at 600 m altitude of the anomaly in (b).

surface) and continued to a constant level. This case is especially important because typical imaging, inversion, differentiation, reduction to the pole and other algorithms need data at a constant altitude surface (e.g. Fedi et al., 2005; Paoletti et al., 2013a). To this end, we applied the VOCO method (through Eqs. (8) and (10)) to data (Fig. 4b) generated by a prismatic source with 5 A/m magnetization intensity on a real topographic surface located in the vicinity of Naples, Italy (Fig. 4a).

The source was placed at a depth of 1 km, centred in the block volume and sized 0.3 km × 0.3 km × 0.3 km. Fig. 4c shows a vertical section of the minimum length solution, from which we easily selected the desired level of the draped-to-level upward continuation. The inversion procedure was applied over a 64 × 64 × 30 block model; each sized 0.1 × 0.1 × 0.05 km^3. Note that we extended the source-volume in correspondence with its borders by adding more blocks (we added 2 blocks on each side of the grid, sized 0.5 km × 0.5 km × 0.05 km), to reduce border effects.

After converting the magnetization model into the upward continuation domain (Eq. (10)) we represented the field at the selected level $z = -600$ m (Fig. 4e). The result is very close to the true field (shown in Fig. 4d), with RMSE = 0.0289 nT. Comparing this result with that produced by using the WAV algorithm by Ridsdill-Smith (2000) shown in Fig. 4f, we noted that some of the topographic effects still remain in the continued data, while the computed RMSE = 0.0441 nT is about 50% higher than the previous one.

3.4. Draped-to-draped upward continuation

In the previous section we showed how VOCO supplies good results in the draped-to-level upward continuation. The same approach is adjustable to perform a draped-to-draped upward continuation, by simply selecting an uneven surface in the VOCO 3D model. We applied the VOCO method (by using Eqs. (8) and (10)) to data generated by a stack of 3D polygonal prisms arranged to form a "stair model" dipping westward (Fig. 5c). The prisms' magnetization intensity is unitary, thickness is 50 m, horizontal dimensions are 150 m × 250 m, and depth ranges are from 75 m to 425 m. In Fig. 5b and d we show the anomalies computed on the lower and upper surfaces of Fig. 5a, respectively.

Fig. 5e shows the result of the VOCO of the data of Fig. 5b, extracted from the upper surface; the computed RMSE with respect to the

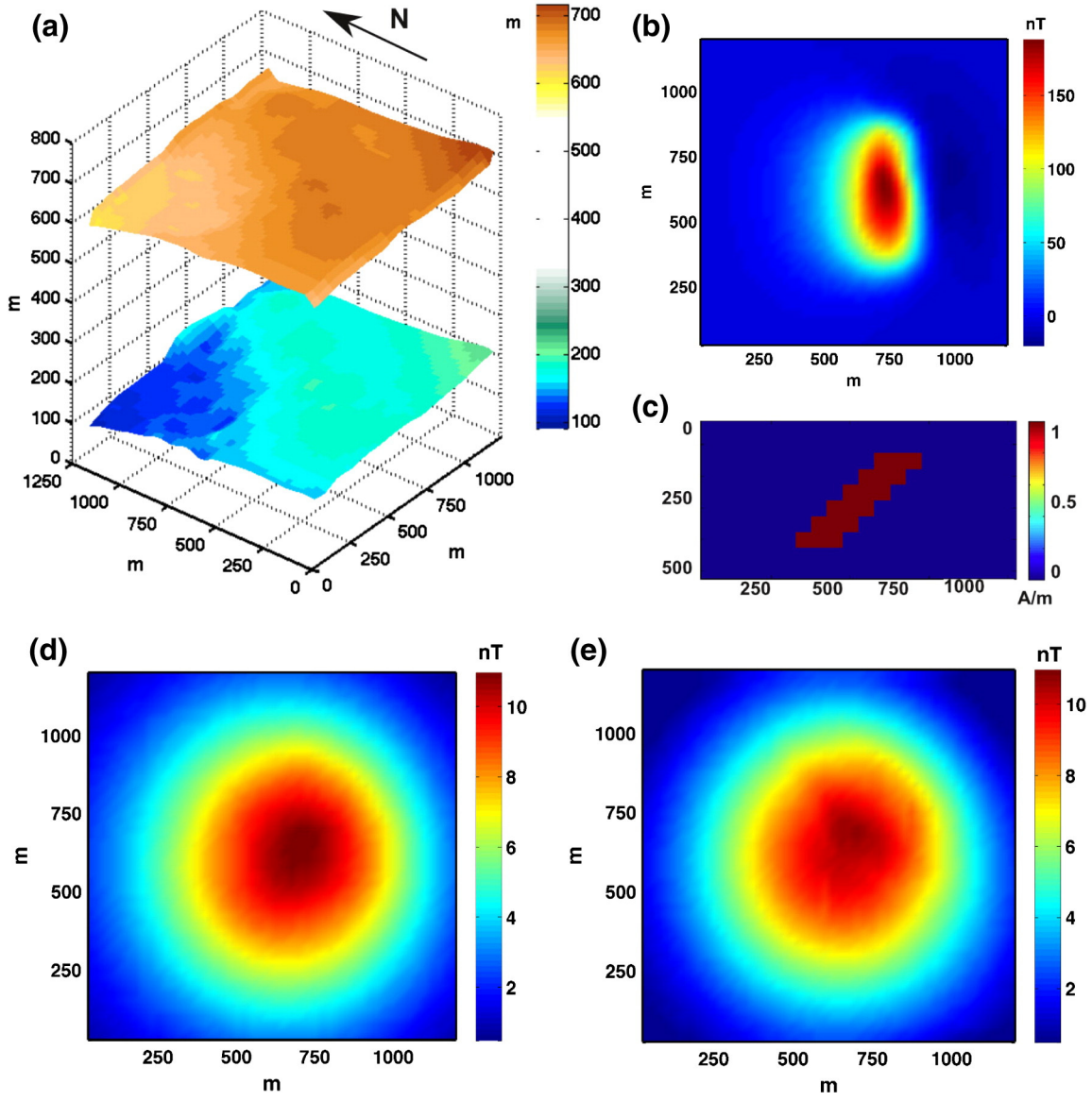

Fig. 5. Draped-to-draped upward continuation: (a) acquisition and continuation surfaces. The lower surface is where the data are acquired, the upper one is where the data are upward continued to, topography lies 50 m below the lower surface; (b) magnetic anomaly of the dipping dike source in (c) computed on the lower surface; (d) magnetic anomaly computed on the upper surface; (e) VOCO of the data in (b) extracted from the upper surface.

observed data in Fig. 5d is 0.6239 nT. We note that VOCO performs rather well for this case too.

4. Case history

We applied the VOCO method to the draped aeromagnetic map of the Ischia Island (Southern Italy) (Fig. 6c) acquired at a constant clearance of 300 m over the island's topography (Paoletti et al., 2009). The results of the upward continuation of the Ischia draped data through VOCO are then compared with the aeromagnetic regional data measured over the island at 2500 m a.s.l. by the National Geological Survey and AGIP (AGIP, 1994). The island of Ischia is one of the volcanic fields of the Phlegrean Volcanic District, a volcanic area of Southern Italy located in the Campanian Plain. Ischia (Fig. 6a) is the emerged top of a large volcanic edifice rising ca. 1000 m from the seafloor, located along a NE–SW ridge. The island extends over a surface of about 42 km^2 and is morphologically dominated by Mt. Epomeo (787 m a.s.l.). It is the result of a prominent resurgence phenomenon; while a valley is located in the north-eastern sector of the island. The island is composed of volcanic rocks (mostly trachytes and phonolites, and minor shoshonites and latites), marine sediments and landslide deposits (e.g., Orsi et al., 1991).

The draped magnetic data of Ischia Island (Fig. 6c, Paoletti et al., 2009) was acquired in October 2005 using a helicopter with a 300 m line-spacing (N–S azimuth) and a 5 m sampling step along each flight line (Fig. 6b). The survey was flown at a constant clearance of about 300 m. The aeromagnetic dataset employed for the VOCO was previously processed for spikes and gaps in data acquisition, GPS positioning, Earth's magnetic field variations and IGRF removal. With respect to the previous regional ones, the new detailed data allowed a more enhanced definition of the island's and offshore anomalies (Paoletti et al., 2008, 2013b).

The magnetic anomalies correlate fairly well with the main volcanological features of the island: the most prominent maxima of the field are placed in correspondence with lava deposits younger than 10 ka before present (B.P.), and the older (28 ka–18 ka B.P.) lava deposits on the coast. Smaller anomalies are located over lavas older than 55 ka B.P. Mt. Epomeo is characterized by a less prominent anomaly connected to the tuffs of the area. With regard to the offshore areas, we observe only a few relevant anomalies in the offshore area west of Ischia and two others in the offshore area west of Procida. The lack of a clear magnetic signature in the central sector of Ischia was interpreted by Paoletti et al. (2009, 2013b). They explained the probable cause was due to the hydrothermal alteration phenomena of igneous materials constituting the basement of the island and/or the presence of partially molten areas inside the basement. The draped dataset was upward continued through the VOCO algorithm by using the surface of acquisition located 300 m above the topography. The inversion procedure was applied over a $54 \times 54 \times 30$ block model with cells sized $0.3 \times 0.3 \times 0.15$ km. Additional blocks were placed at the model borders to reduce border effects. Due to some noise in the data we preferred using Eq. (11) to obtain a regularized solution. Then the magnetization model was converted into VOCO magnetic data by using Eq. (12). Finally, the data were extracted at a 2500 m a.s.l. (Fig. 7a).

The VOCO results of Fig. 7a were compared with a dataset extracted over the same area from the aeromagnetic map of Italy. These regional data were measured by AGIP in 1981 during a regional survey carried

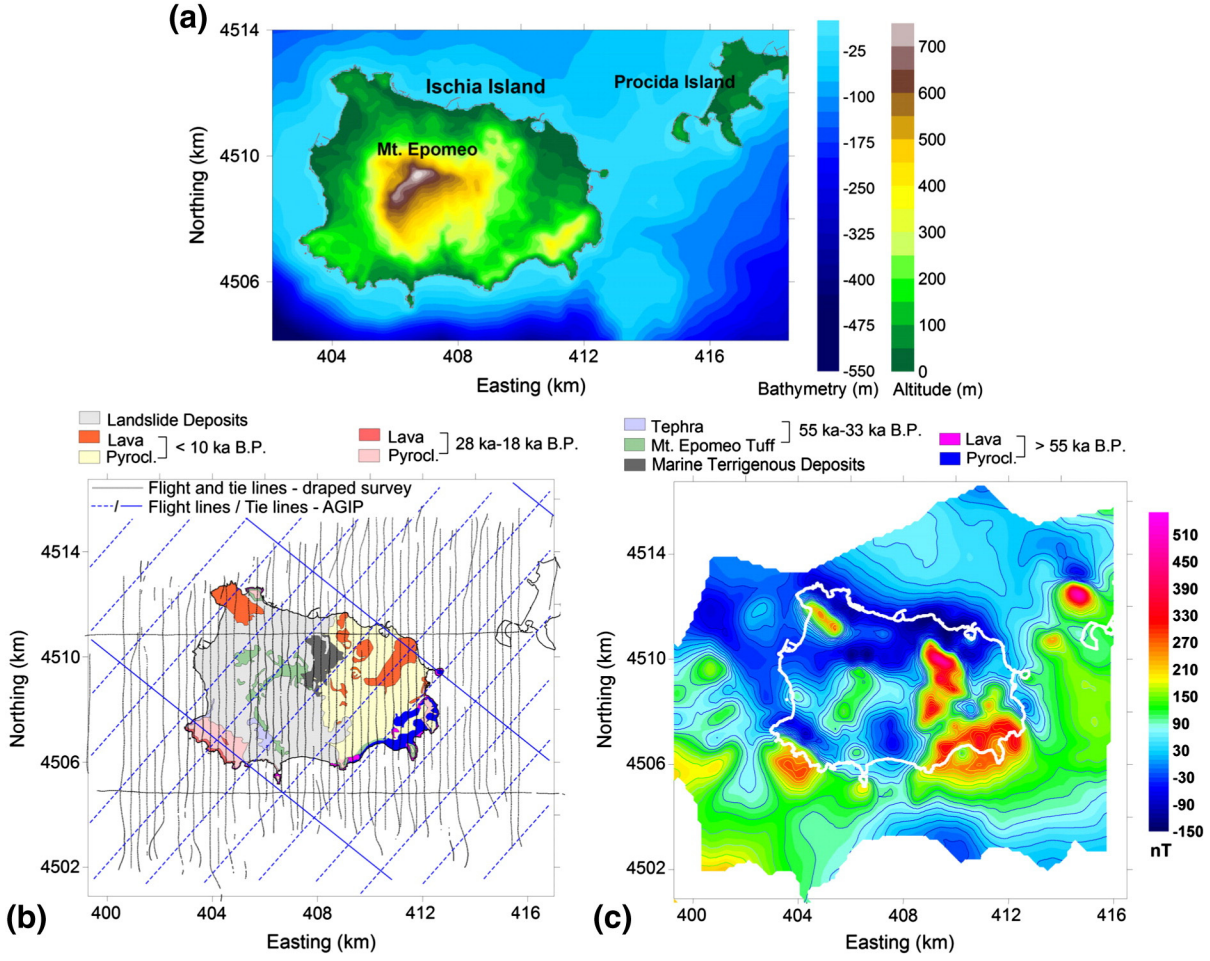

Fig. 6. VOCO applied to the aeromagnetic data measured at the Ischia Island, Southern Italy: (a) topography of the area; (b) geological setting of Ischia (Vezzoli, 1988) with overlapped the flight lines of a high-resolution draped survey and a regional survey (AGIP, 1994); (c) magnetic map from the high-resolution survey.

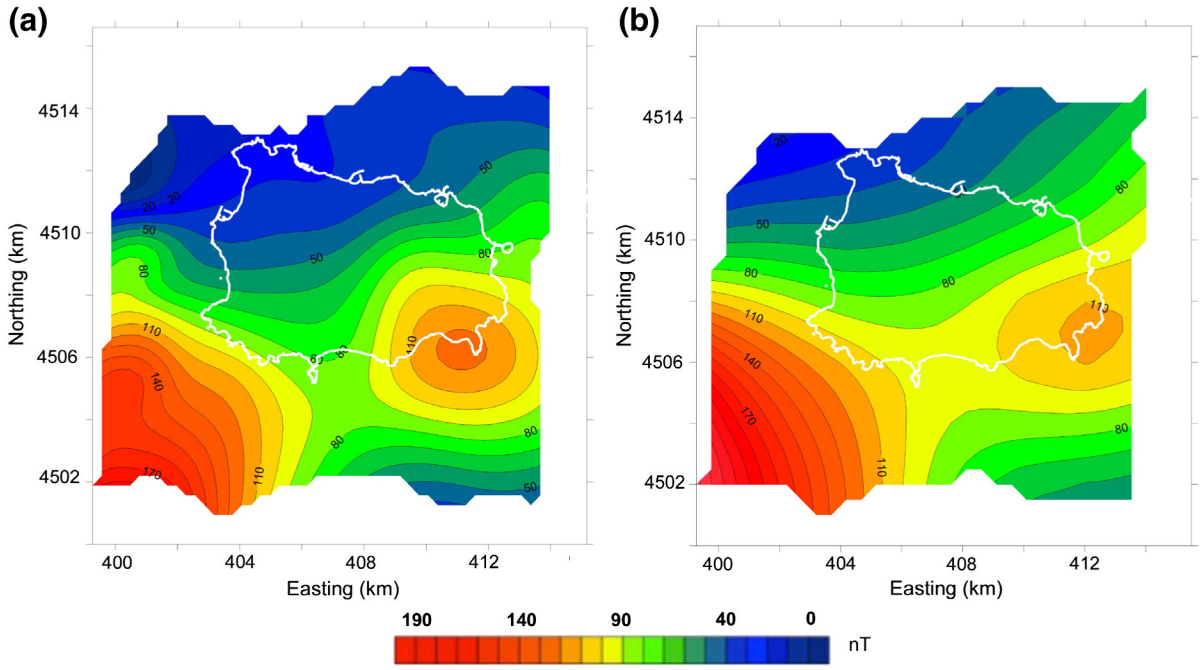

Fig. 7. Comparison of data obtained through the VOCO from a draped high-resolution dataset with measured regional data: (a) Volume upward Continuation computed at 2500 m a.s.l.; (b) AGIP dataset measured at 2500 m a.s.l.

out at a flight altitude of 2500 m a.s.l. with a line spacing of 2000 m (Fig. 7b). The AGIP data outlined a prominent magnetic anomaly in the south western offshore of the island and a smaller anomaly in the south-eastern area of the island. Whereas there is a decreasing trend of the magnetic field both northward and southward. These features are described in more detail in the VOCO map at 2500 m altitude (Fig. 7a), due to the fact that the VOCO data was obtained from high-resolution draped data with a spacing of about 1/6 of the AGIP dataset spacing (see Fig. 6b). Despite a few differences in the two maps due to the different survey layouts and detail, the datasets exhibit a rather similar anomaly amplitude and pattern, showing that the VOCO yields reliable results.

5. Conclusions

In this paper we proposed a new approach to upward continue potential field data, which yields good results on all types of measurements and continuation surfaces. Moreover, the method is also useful for downward continuation, as a regularized inversion may be used to obtain stable results, instead than the minimum-length solution. One advantage of this novel approach is that the VOCO method yields a Volume upward Continuation, and thus it may be used to extract in a simple way, the continuation on any kind of surface, including multiple levels. We may in fact define all four kinds of continuation problems (*level-to-level, level-to-draped draped-to-level and draped-to-draped*) by simply transforming the magnetization model into an upward continued 3D volume (Eqs. (10) and (12)) and by picking up the sought surface from it. The real-case example from Ischia Island confirms the effectiveness of this method, as the VOCO result computed at a 2500 m above sea level is in good agreement with the regional data measured at the same altitude. Inversion obviously implies higher computational costs than standard continuation algorithms, especially for large-scale problems. Computational costs are however well compensated by: a) the versatility of the method in providing, from a single inversion, the continuation along any desired surface intersecting the source volume; and b) the high-quality of the continuation of all four kinds of upward continuation problems as well as the downward continuation case.

Acknowledgements

We are indebted to Mark Pilkington for his for comments and suggestions that greatly helped to improve our manuscript. We are grateful to David Giampietro for the language revision.

References

Agip, 1994. Servizio Geologico Nazionale, Carta Aeromagnetica d'Italia, scala 1:1000000. Istituto Poligrafico Zecca dello Stato (in Italian).
Blakely, R., 1996. Potential Theory in Gravity and Magnetic Applications. Cambridge University Press, p. 437.
Cella, F., Fedi, M., Florio, G., 2009. Toward a full multiscale approach to interpret potential fields. Geophys. Prospect. 57 (4), 543–557. http://dx.doi.org/10.1111/j.1365-2478.2009.00808.x.
Cordell, L., 1985. Techniques, applications and problems of analytical continuation of New Mexico aeromagnetic data between arbitrary surfaces of very high relief. International Meeting on Potential Fields in Rugged Topography 7, pp. 96–99.
Cribb, J.B., 1976. Application of the generalized linear inverse to the inversion of static potential data. Geophysics 41 (6), 1365–1369. http://dx.doi.org/10.1190/1.1440686.
Fedi, M., 2007. DEXP: a fast method to determine the depth and the structural index of potential fields sources. Geophysics 72 (1), I1–I11. http://dx.doi.org/10.1190/1.2399452.
Fedi, M., Cascone, L., 2011. Composite continuous wavelet transform of potential fields with different choices of analyzing wavelets. J. Geophys. Res. 116, B07104. http://dx.doi.org/10.1029/2010JB007882.
Fedi, M., Pilkington, M., 2012. Understanding imaging methods for potential field data. Geophysics 77 (1), G13–G24. http://dx.doi.org/10.1190/geo2011-0078.1.
Fedi, M., Rapolla, A., Russo, G., 1999. Upward continuation of scattered potential field data. Geophysics 64 (2), 443–451. http://dx.doi.org/10.1190/1.1444549.
Fedi, M., Hansen, P.C., Paoletti, V., 2005. Analysis of depth resolution in potential-field inversion. Geophysics 70 (6), A1–A11. http://dx.doi.org/10.1190/1.2122408.
Fedi, M., Cella, F., Quarta, T., Villani, A., 2010. 2D continuous wavelet Transform of potential fields due to extended source distributions. Appl. Comput. Harmon. Anal. 28, 320–337. http://dx.doi.org/10.1016/j.acha.2010.03.002.
Fedi, M., Florio, G., Cascone, L., 2012. Multiscale analysis of potential fields by a ridge consistency criterion: the reconstruction of the Bishop basement. Geophys. J. Int. 188, 103–114. http://dx.doi.org/10.1111/j.1365-246X.2011.05259.x.
Gibert, D., Galdéano, A., 1985. A computer program to perform transformations of gravimetric and aeromagnetic surveys. Comput. Geosci. 11, 553–588.
Hansen, P.C., 2010. Discrete Inverse Problems — Insight and Algorithms. Society of Industrial and Applied Mathematics.
Mauri, G., Williams-Jones, G., Saracco, G., 2010. Accurately determining the depths of hydrothermal systems by self-potential and multi-scale wavelet tomography. J. Volcanol. Geotherm. Res. 191, 233–244. http://dx.doi.org/10.1016/j.jvolgeores.2010.02.004.

Menke, W., 1989. Geophysical Data Analysis: Discrete Inverse Theory. Academic Press, p. 289, (ISBN 01249092130).
Meurers, B., Pail, R., 1998. Potential-field continuation between irregular surfaces — remarks on the method by Xia et al. Geophysics 63 (1), 104–108. http://dx.doi.org/10.1190/1.1444301.
Oppenheim, A.V., Schafer, R.W., 1975. Digital Signal Processing. Prentice-Hall, p. 608.
Orsi, G., Gallo, G., Zanchi, A., 1991. Simple-shearing block resurgence in caldera depressions. A model from Pantelleria and Ischia. J. Volcanol. Geotherm. Res. 47, 1–11.
Paoletti, V., Fedi, M., Florio, G., Supper, R., Rapolla, A., 2004. The new integrated aeromagnetic map of the Phlegrean Fields volcano and surrounding areas. Ann. Geophys. 47 (5), 1569–1580.
Paoletti, V., Secomandi, M., Fedi, M., Florio, G., Rapolla, A., 2005. The integration of magnetic data in the Neapolitan volcanic district. Geosphere 1, 85–96. http://dx.doi.org/10.1130/GES00003.1.
Paoletti, V., Rapolla, A., Secomandi, M., 2008. Magnetic signature of submarine volcanoes in the Phlegrean Fields-Ischia Ridge (North-Western side of the Bay of Naples, Southern Italy). Ann. Geophys. 51 (4), 575–584.
Paoletti, V., Di Maio, R., Cella, F., Florio, G., Motschka, K., Roberti, N., Secomandi, M., Supper, R., Fedi, M., Rapolla, A., 2009. The Ischia volcanic island (Southern Italy): inferences from potential field data interpretation. J. Volcanol. Geotherm. Res. 179, 68–86. http://dx.doi.org/10.1016/j.jvolgeores.2008.10.008.
Paoletti, V., Ialongo, S., Florio, G., Fedi, M., Cella, F., 2013a. Self-constrained inversion of potential fields. Geophys. J. Int. 195 (2), 854–869. http://dx.doi.org/10.1093/gji/ggt313.
Paoletti, V., D'Antonio, M., Rapolla, A., 2013b. The structural setting of the Ischia Island (Phlegrean Volcanic District, Southern Italy): Inferences from geophysics and geochemistry. J. Volcanol. Geotherm. Res. 249, 155–173. http://dx.doi.org/10.1016/j.jvolgeores.2012.10.002.
Paterson, N., Reford, S., Kwan, K., 1990. Continuation of magnetic data between arbitrary surfaces: advances and applications. 60th Annual International Meeting, SEG, Expanded Abstracts, pp. 666–669.
Pilkington, M., Roest, W., 1992. Draping aeromagnetic data in areas of rugged topography. J. Appl. Geophys. 29 (2), 135–142. http://dx.doi.org/10.1016/0926-9851(92)90004-5.
Ridsdill-Smith, T.A., 2000. The Application of the Wavelet Transform to the Processing of Aeromagnetic Data(PhD thesis) University of Western Australia, p. 197.
Sailhac, P., Gibert, D., Boukerbout, H., 2009. The theory of the continuous wavelet transform in the interpretation of potential fields: a review. Geophys. Prospect. 57, 517–525. http://dx.doi.org/10.1111/j.1365-2478.2009.00794.x.
Vezzoli, L., 1988. Island of Ischia. Quaderni de La Ricerca Scientifica 114 (10). CNR, Progetto Finalizzato Geodinamica, Rome, p. 133 (10).
Wang, B., 2006. 2D and 3D potential-field upward continuation using splines. Geophys. Prospect. 54 (2), 199–209. http://dx.doi.org/10.1111/j.1365-2478.2006.00526.x.
Xia, J., Sprowl, D.R., Adkins-Heljeson, D., 1993. Correction of topographic distortions in potential-field data, a fast and accurate approach. Geophysics 58 (4), 512–523. http://dx.doi.org/10.1190/1.1443434.

ACCURATE EVALUATION OF EDGES AND DIP OF FAULTS AND CONTACTS THROUGH THE VOLUME UPWARD CONTINUATION (VUC) OF GRAVITY DATA

D. Mastellone, M. Fedi, V. Paoletti
DISTAR, Department of Earth Sciences, Environment and Resources, University of Naples Federico II, Italy

Introduction. Several methods have been used to retrieve values of dip of faults by using lateral offsets of the zero-crossover point of the second horizontal derivative of upward-continued gravity profiles. The use of derivatives of potential fields represents a signal enhancement technique experimented since a long time. It allows the information content of the signal to be enhanced without implying any arbitrary assumption. Often, such methods are coupled with upward continuation, which is used to transform anomalies measured on one surface into those that would have been measured on some higher altitude surface.

In this paper we demonstrate the efficiency of a new approach to upward continue potential field data, the Volume Upward Continuation (VUC), coupled with traditional horizontal derivative techniques. By using VUC it is immediate showing that upward continuation of the signal to higher altitudes yield information about progressively deeper sectors of the discontinuity. In particular, looking at the position of the maxima of the horizontal derivative of the continued field, we can observe that they will be laterally shifted toward the dipping direction of the discontinuity, in a way proportional to the continuation height.

We applied VUC followed by horizontal derivative to a gravity profile extracted from a gravity survey on the Venelin-Aksakov fault in Bulgaria, in order to get further information on the dipping direction of this structure.

Upward continuation and horizontal derivatives. Upward continuation operator uses measurements of a field at one elevation, level or surface to determine the values of the field at a higher level.

Upward continued data can be calculated by convolution in either the space domain or the Fourier domain. In this last domain the Fourier transform of the data is simply multiplied by the frequency filter:

$$e^{-|\mathbf{k}|\Delta z} \qquad \Delta z > 0 \qquad (1)$$

where **k** is the wavenumber vector and Δz is the distance between the original surface and the final one. Real data are discrete and refer to a finite survey area; so, when using circular convolution to calculate upward continuation in the frequency domain, aliasing errors can affect the low frequency content of upward continued data. These errors can be reduced by performing the Fourier transform on a larger dataset, which spreads outside the survey area (Oppenheim and Schafer, 1975; Fedi *et al*., 2012), built with other surveys data or, through extrapolation algorithms (zero-padding, maximum entropy extension, symmetric extension).

Upward continuation is mostly helpful to enhance the effects of deep sources, as it attenuates the highest frequency content of the signal, which is usually associated to shallow sources; or to trace the dipping direction of oblique discontinuities (e.g. faults) (Rapolla *et al*., 2002; Cella *et al*., 2000; Tatchum *et al*., 2011).

The horizontal derivative method (Cordell and Grauch, 1985) represents one of the most used derivative approaches of potential fields, as it allows locating the horizontal position of the density or magnetization boundaries (Paul and Goodacre, 1984; McGrath, 1991; Rapolla *et al*., 2002; Cella *et al*., 2010; Stavred and Reid, 2010; Tatchum *et al*., 2011).

The expression for the horizontal derivative of a potential field M, in the space domain (x,y) is

$$h(x,y) = \sqrt{\left(\frac{\partial M}{\partial x}\right)^2 + \left(\frac{\partial M}{\partial y}\right)^2} \qquad (2)$$

The horizontal derivative has its maxima in correspondence of the lateral boundaries of the source anomaly. This supplementary information cannot be, of course, straightaway

recognized from the original signal and can be really helpful to constrain geological models and guide the geological interpretation.

However, as suggested by Grauch and Cordell (1987) and Rapolla *et al.* (2002), the maxima of the horizontal gradient magnitude can be offset from a position directly above the geologic contacts, especially when contacts are not steep or when several contacts are close together; so this link between maximum points and edges position is consistent only in the case of vertical or sub-vertical discontinuities. For example Khattach *et al.* (2004) associated the horizontal gradient magnitude of the Bouguer gravity anomaly to the upward continuation of the field to characterize the faults of the Triffa basin in North Morocco.

However, in the presence of oblique surfaces, the maxima of the horizontal derivative are located in correspondence with the discontinuity at an intermediate depth (Grauch and Cordell, 1987), without any information about the dipping direction.

Therefore, the efficacy of this simple method is good in the case of structural features typical of an extensional regime (normal faults, transform faults) or in the presence of dykes, volcanic conduits, plutonites, etc. On the contrary, the method is hardly usable when the structural setting is characterised by a compressive tectonic style (presence of inverse faults, transpressive faults, multiple thrust systems, etc.).

To overcome this issue many authors (i.e. Cella *et al*., 2000; Martelet *et al*; 2001; Rapolla *et al*., 2002; Tatchum *et al*., 2011; Fedi and Pilkington, 2012) propose to couple upward continuation with gradient: first upward continuing the data and then computing its horizontal derivative to see how its maxima shift with respect to the subsurface structure. In fact, the position of the maxima of the horizontal derivative of the continued field will be laterally shifted toward the dipping direction of the discontinuity, proportionally to the continuation level.

The DEXP method adds a third step to this procedure consisting in multiply the derived field with a scaling function (Fedi, 2007; Fedi and Pilkington, 2012).

The maxima of the horizontal derivative of the field continued at different levels can also be localized automatically (see for example Blakely and Simpson, 1986) to speed up the data analysis.

In this work we propose to follow this procedure, but taking in account the VUC method for upward continuation. One of the first advantages of using VUC instead of standard upward continuation algorithms is that edge effects are automatically encountered as long as the final result is built. Another important advantage occurs especially in the gravity case, where the VUC has an intrinsic connection also with the vertical derivative of the field. These two topics will be better clarified in the paragraph on VUC method.

Volume Upward Continuation. We propose a new approach to upward continue potential field data, based on the *minimum-length* solution of the inverse potential field problem. The method yields a volume upward continuation, and reveals to be advantageous over the classical techniques based on the Fast Fourier transform (Cordell, 1985; Pilkington and Roest, 1992; Blakely, 1996; Fedi *et al*., 1999; and Ridsdill-Smith, 2000) especially when dealing with truncated anomalies and when draped-to-level upward continuation is needed.

This approach has the advantage of generating the field in the upward continuation domain (i.e., at many altitudes) as a unique solution in a 3D volume. Within this volume, all the three types of continuation (level-to-level, level-to-draped and draped-to-level) are naturally defined. In fact, the upward continued data volume can be immediately visualized and used to obtain the field on several surfaces of whatever kind (draped or level).

Due to this feature we will call this method Volume Upward Continuation (VUC). In the VUC the border effects, typical of upward continuation, are controlled in an optimal way: the upward continued data are in fact proportional to a least-square solution of the inverse problem.

Starting from the continuous inverse geomagnetic problem (e.g., Fedi *et al*., 2005) discretized over a volume Ω of N cells, each of them with constant magnetization m_j, we can write a linear system of equations:

$$\mathbf{Km}=\mathbf{d} \qquad (3)$$

where **K** is the kernel coefficients matrix and **d** is the measured data vector. This inverse problem is under-determined, as the unknowns are more than data, so it has infinite solutions. The simplest solution is that minimizing the Euclidean norm of the solution **m**:

$$\mathbf{m} = \mathbf{K}^T(\mathbf{K}\mathbf{K}^T)^{-1}\mathbf{d} \qquad (4)$$

Cribb (1976) showed, for this solution, this remarkable equation in the frequency domain:

$$e^{-|\mathbf{k}|h_i}F[\mathbf{d}] = F[\mathbf{m}_i]\frac{V(\mathbf{k})}{4} \qquad i=1, \ldots, L \quad (5)$$

where F denotes the Fourier transformation, L is the number of layers, $\mathbf{m}_i$ is the magnetization intensity vector of the i^{th} layer, $\mathbf{h}_i$ is its depth, $\mathbf{k}$ is the wavevector with components k_x, k_y and $(k_x^2+k_y^2)^{1/2}$, $V(\mathbf{k})=(\mathbf{t}.\mathbf{k})(\mathbf{n}.\mathbf{k})/|\mathbf{k}|^2$, with **t** and **n** unit-vectors along the inducing field and magnetization vectors. Therefore the i^{th} layer of the magnetization distribution $\mathbf{m}_i$ is directly related to the upward continued field of the data **d**, to a distance equal to the opposite of the layer depth: $z=-h_i$. Anti-transforming the second member of Eq. (5) and assuming, for simplicity, magnetization and inducing field both vertical, we find:

$$\frac{\mathbf{m}_{z_i}}{4} = \mathbf{d}_{h_i} \qquad i=1,\ldots,L \qquad (6)$$

showing that $\mathbf{d}_{h_i}$ and $\mathbf{m}_{z_i}$ differ only for a numeric constant.

Based on Eqs. (5) and (6) we therefore may use the *minimum length* solution as an effective alternative to common upward continuation techniques.

In Fig. 1 we tested the VUC approach in two simple cases: level-to-level and level-to-draped upward continuation of the magnetic anomaly due to a horizontal dipole line located at 30 m depth. We observe that the field obtained from the *minimum-length* solution well reproduces the computed anomaly at the same altitude.

The result has been achieved following these steps:

- inverting the magnetic anomaly to obtain the *minimum-length* solution;
- converting the magnetization volume to an upward continued field volume through Eq. (6);
- extracting the i^{th} layer corresponding to the desired continuation altitude $z=-h_i$ (level-to-level);
- or extracting the field corresponding to the desired draped surface (level-to-draped).

The most valuable advantage of the VUC method occurs when the field data are on a draped surface (e.g., a topographic surface) and are continued to a constant level. Some synthetic tests (Mastellone *et al.*, 2013) shows that the VUC result, compared with that produced by using other continuation algorithms, can better avoid topographic effects in the continued data.

VUC is helpful also if the profile is severely truncated, and extrapolation is needed before performing upward continuation. In this case, one could obtain very different results, from several extrapolation algorithms. In this case VUC helps to circumvent the border effects by extending the source-volume with additional blocks at its borders. The border effects are better controlled, because of the constraint, inherent in the inversion process, that the predicted data must fit the measured data..

VUC in the gravity case: the role of the vertical derivative. In the gravity case the anomalous density distribution coming from a *minimum-length* inversion is proportional to the upward continuation of the vertical derivative of the observed data:

$$F[\mathbf{d}] = \frac{\mathbf{k}e^{-|\mathbf{k}|h_i}}{\pi G}F[\mathbf{m}_i] \qquad i=1, \ldots, L \quad (7)$$

where G is the gravitational constant, F denotes the Fourier transformation, L is the number of layers, $\mathbf{m}_i$ is the density vector of the i^{th} layer, $\mathbf{h}_i$ is its depth, $\mathbf{k}$ is the wavevector with components k_x, k_y and $(k_x^2+k_y^2)^{1/2}$. Therefore the i^{th} layer of the density distribution $\mathbf{m}_i$ is directly

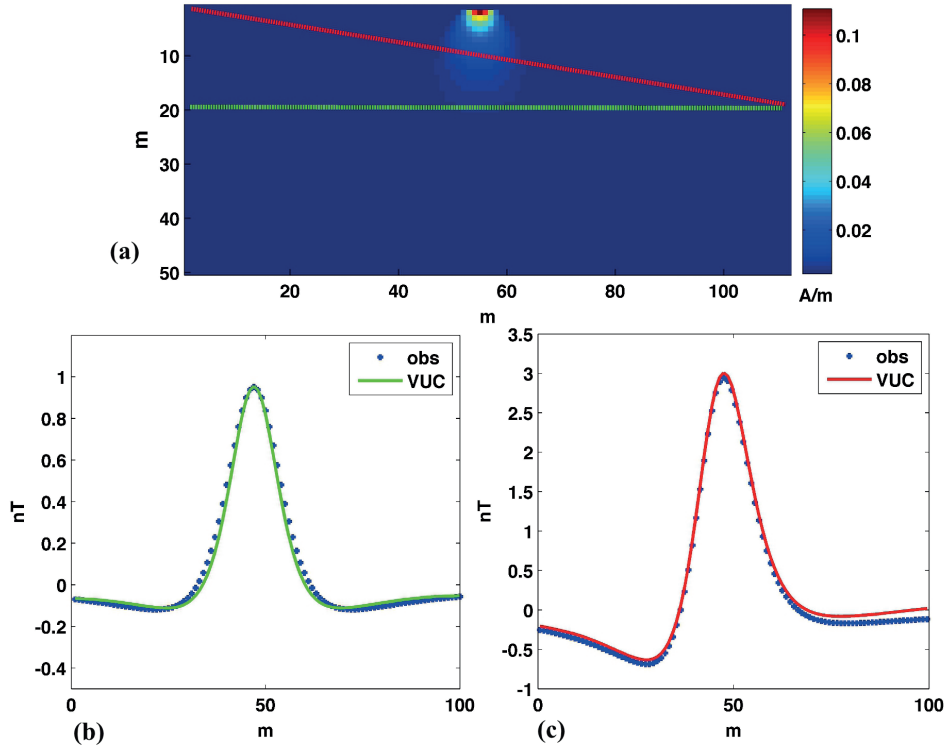

Figure 1 - VUC continuation workflow: synthetic test on a magnetic anomaly due to a horizontal dipole line located at 30 m depth. **a**) *minimum-length* solution section; **b**) *level-to-level* VUC profile (green line) converted, in agreement with equation **(6)**, from the *minimum-length* solution (green line at z= -20 m in (**a**)); **c**) *level-to-draped* VUC profile (red line) converted from the *minimum-length* solution (inclined red line in (**a**) rising from 0 to 20 m). We note a good agreement of VUC field with the true data (blue lines in (**b**) and (**c**)).

related to the upward continued field of the vertical derivative of the data **d**, to a distance equal to the opposite of the layer depth: $z=-h_i$.

So the resulting signal is a combination of a vertical derivative filter, which amplifies the high-frequency components of the data, and an upward continuation, which is, on the contrary, a low pass filter for definition.

This feature is interesting and has been investigated by many authors who tested the coupling of upward continuation and field derivatives.

The benefits of using the vertical derivative were documented by Fedi and Florio (2001): they showed that when the gravity fields of several sources interfere, it is more accurate to use the vertical derivative of the field rather than the field itself to determine the location of contacts of the sources. This is in part due to the vertical derivative being able to isolate the gravity effects of individual sources better than the Bouguer anomaly. Hence, the signatures of small-scale features that are not easily identified in Bouguer anomaly maps can be identified and mapped using the vertical derivative response.

So from the horizontal derivative magnitude of the VUC response, it is possible to outline and differentiate vertical and dipping geological contacts as well as the direction of the dip; and also to separate multiple anomalies.

The higher frequencies will be enhanced at the expense of lower frequencies; however, if the data contain noise or small errors, the coupled filter already inbuilt in Cribb's relationship

[Eq. (7)] for gravity fields, by first suppressing the highest frequencies, (upward continuation), can help to remove that noise.

Case history: the Venelin-Aksakov fault (Bulgaria). The VUC method combined with horizontal derivative was applied to an anomalous gravity profile (Stavrev and Reid, 2010) in the area of the Dolna Kamchia depression (Bulgaria), across the Venelin-Aksakov fault, at the western bound of the depression.

The Dolna (lower) Kamchia depression lies in Eastern Bulgaria along the lower course of the Kamchia river. This depression is elongated west to east and runs into the adjoining Black Sea shelf, according also to geophysical data. It belongs geologically to the most northeastern part of the Balkan orogenic system. The Venelin-Aksakov fault is the western bound of the depression.

An intense gravity gradient zone (see Figs. 5 and 6 in Stevrev and Reid, 2010) indicates a steep contact structure with north-to-south orientation. Exploratory wells west and east of the line of the gravity gradient zone indicate a considerable difference in the depth to the boundary between the low-density tertiary-upper Cretaceous layers and the denser lower Cretaceous and deeper sediment layers, the depth to high-density strata increases by a factor of 10, going from the western elevated horst structure to the eastern depression.

Core samples from wells in the Dolna Kamchia depression show also a significant difference in the density of tertiary-upper Cretaceous layers and lower Cretaceous-Jurassic-Triassic layers.

The analysed Bouguer gravity profile was extracted across the gradient axis of the gravity anomaly map shown in Fig. 2a and the geologic data available for the area strongly suggest that this is a contact of considerable depth extent.

We performed VUC on the anomaly gravity profile in Fig. 2b obtaining the vertical section showed in Fig. 2c. Then we calculated the horizontal derivative of the VUC result, following Eq. (2), and we extracted from the section profiles corresponding to increasing continuation heights (see Fig. 2d and the related key table).

For a vertical contact, the derivative maximum values, related to different continuation heights, are along the same vertical line, whereas for dipping contacts, the maxima gradually move in the direction of dip.

Furthermore the absolute values of the horizontal derivative maxima decrease as the height continuation height increases, as one could obviously expect. In fact the resulting signal is related to progressively deeper sectors of the discontinuity, if increasing continuation heights are analysed.

In the case shown in Fig. 2c the position of the maxima slightly shifts in the direction of dipping, but the shape of the derivative function is skewed in the direction of dipping. This is in agreement with other geophysical and geological data, suggesting a steep and abrupt contact between tertiary-upper Cretaceous layers and lower Cretaceous-Jurassic-Triassic layers.

Conclusions. In this paper we introduce a new tool, the VUC (Volume Upward Continuation), for the well-known procedure of combining upward continuation and vertical and horizontal derivatives of potential field data.

The VUC by itself yields good results especially in case of draped-to-level upward continuation and when dealing with the continuation of severely truncated anomalies. One advantage of the VUC tool is that it yields a volume upward continuation, and thus it may be used to extract in a simple way the continuation on any kind of surface and also to multiple levels. We may in fact define all the three kinds of continuation problems (*level-to-level, level-to-draped and draped-to-level*) by simply picking up the sought surface on the inverted 3D magnetization model and then transforming the corresponding magnetization data into upward continued data, through Eqs. (5) and (6). So it can be usefully placed side by side to common upward continuation techniques.

In the gravity case, moreover, the VUC absorbs also the vertical derivative in its result, fulfilling a remarkable feature, already examined by many authors who tested its efficiency if

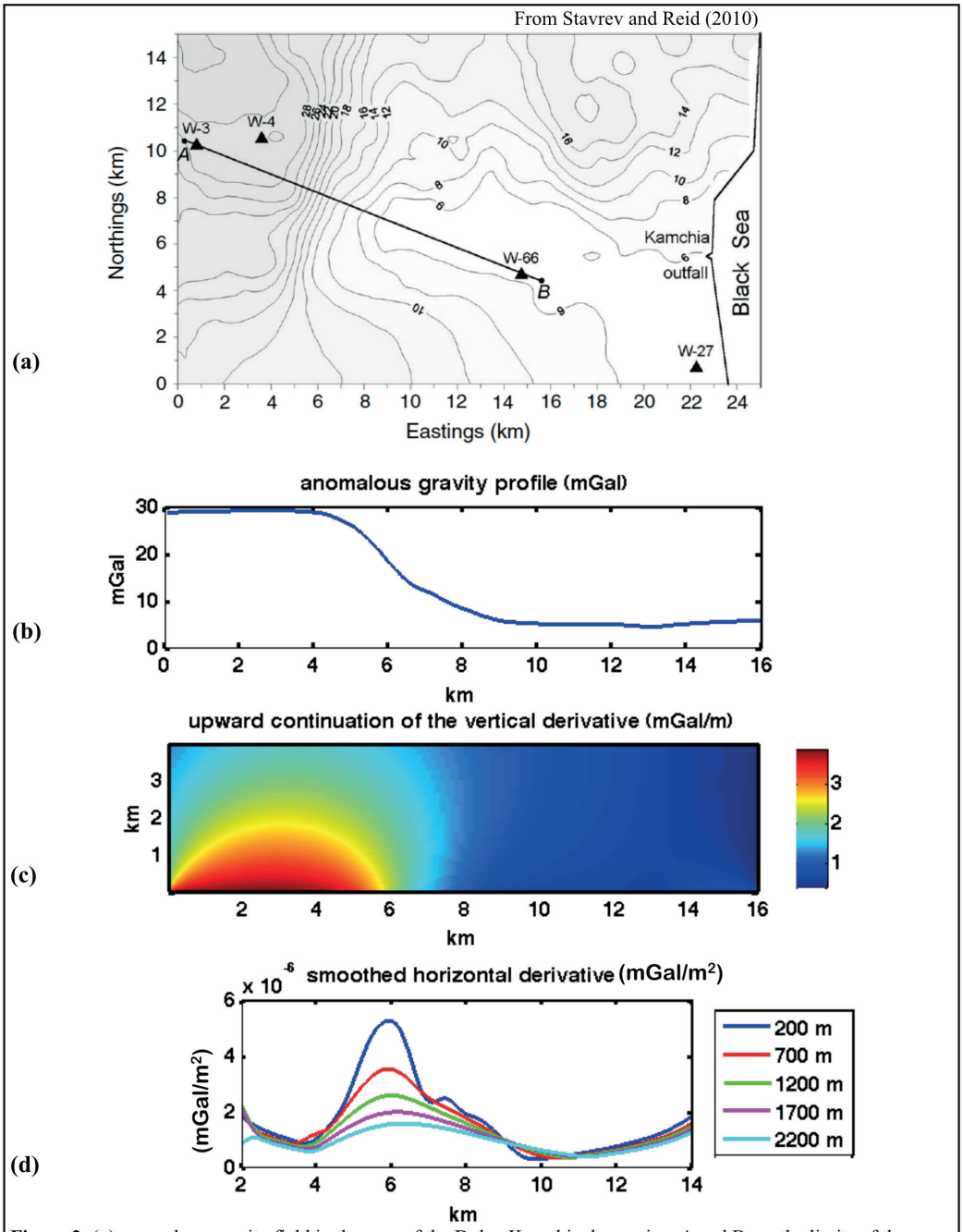

Figure 2: (**a**) anomalous gravity field in the area of the Dolna Kamchia depression, A and B are the limits of the gravity profile across the Venelin-Aksakov fault shown in (**b**); (**c**) VUC of the first vertical derivative of the gravity profile in (**b**); (**d**) horizontal gradient of the VUC for different continuation heights listed in the box at the right side).

combined with horizontal derivatives also (Fedi and Florio, 2001; Florio *et al.*, 2006; Tatchum *et al.*, 2011). The VUC, when applied to a real field data example from the Venelin-Aksakov fault in Bulgaria, to locate fault edge and dipping direction, provides results in agreement with geological and geophysical studies already performed in the same area.

References

Blakely R.J., 1996: *Potential theory in gravity and magnetic applications*. Cambridge University Press.

Blakely R.J. and Simpson R.W., 1986: *Approximating edges of source bodies from magnetic or gravity anomalies*. Geophysics, **51** (7), 1494-1498.

Cella F., Fedi M., Florio G. and Rapolla A., 2000: *Boundary analysis del campo 3D di anomalie gravimetriche*. XIX Convegno del Gruppo Nazionale di Geofisica della Terra Solida – Riassunti delle Comunicazioni, Novembre 2000, CNR, p. 131.

Cordell L., 1985, *Techniques, applications and problems of analytical continuation of New Mexico aeromagnetic data between arbitrary surfaces of very high relief*. International Meeting on Potential Fields in Rugged Topography, **7**, 96–99.

Cordell L. and Grauch V.J.S., 1985: *Mapping basement magnetization zones from aeromagnetic data in the San Juan basin, New Mexico*. Hinze, W.J., (Ed.), The utility of regional gravity and magnetic anomaly Maps: Society of Exploration Geophysicists, 181–197.

Cribb J. B., 1976: *Application of the generalized linear inverse to the inversion of static potential data*. Geophysics, **41**, no. 6, 1365-1369.

Fedi M., Rapolla A., and Russo G., 1999: *Upward continuation of scattered potential field data*. Geophysics, **64**, no. 2, 443-451, doi: 10.1190/1.1444549.

Fedi M. and Florio G., 2001: *Detection of potential fields source boundaries by enhanced horizontal derivative method*. Geophysical Prospecting, **49**, 40–58.

Fedi M., Hansen P. C., and Paoletti V., 2005: *Analysis of depth resolution in potential-field inversion*. Geophysics, **70**, no. 6; P. A1–A11; doi: 10.1190/1.2122408

Fedi M. and Pilkington M., 2012: *Understanding imaging methods for potential field data*. Geophysics, **77**, 1, G13-G24

Fedi, M., 2007: *DEXP: a fast method to determine the depth and the structural index of potential fields sources*. GEOPHYSICS, **72**, I1.

Fedi, M., Florio G. and Cascone L., 2012: *Multiscale analysis of potential fields by a ridge consistency criterion: the reconstruction of the Bishop basement*. Geophysical Journal International, **188**, 103-114.

Florio G., Fedi M. and Pasteka R., 2006: *On the application of Euler deconvolution to the analytic signal*. Geophysics, **71**, L87–L93.

Grauch V.J.S. and Cordell L., 1987: *Limitations of determining density or magnetic boundaries from the horizontal gradient of gravity or pseudogravity data*. Geophysics, **52**, 118–121.

Khattach D., Keating P., Mostafa M.L., Chennouf T., Andrieux P. and Milhi A., 2004: *Apport de la gravimétrie à l'étude de la structure du bassin des Triffa (Maroc nord-oriental): implications hydrogéologiques*. C. R. Geosciences **336**, 1427–1432.

Martelet G., Sailhac P., Moreau F. and Diament M., 2001: *Characterization of geological boundaries using 1-D wavelet transform on gravity data: Theory and application to the Himalayas*. Geophysics, **66**(4), 1116.

Mastellone D., Fedi M., Ialongo S. and Paoletti V., 2013: *Volume upward continuation of potential fields from the minimum-length solution: An optimal tool for continuation through general surfaces*. SEG Technical Program Expanded Abstracts 2013: pp. 1200-1205. doi: 10.1190/segam2013-0593.1

McGrath P.H., 1991: *Dip and depth extent of density boundaries using horizontal derivatives of upward continued gravity data*. Geophysics, **56** (10), 1533-1541

Oppenheim A. V. and Schafer R. W., 1975: *Digital Signal processing*: Prentice-Hall.

Paul M.K. and Goodacre A.K., 1984: *The gravity profile and its role in positioning the edge of a two-dimensional faulted structure having an arbitrary vertical variation of density*. Geophysics, **49**, 1097-1104.

Pilkington M., and Roest W., 1992: *Draping aeromagnetic data in areas of rugged topography*. Journal of Applied Geophysics, **29**, no. 2, 135–142.

Rapolla A., Cella F., Fedi M. and Florio G., 2002: *Improved techniques in data analysis and interpretation of potential fields: examples of application in volcanic and seismically active areas*. Annals of geophysics, **45**, 6; and references therein.

Ridsdill-Smith T. A., 2000: *The Application of the Wavelet Transform to the Processing of Aeromagnetic Data*. PhD thesis, University of Western Australia.

Stavrev P. and Reid A., 2010: *Euler deconvolution of gravity anomalies from thick contact/fault structures with extended negative structural index*. Geophysics, **75**, 6; p. i51–i58, 6 figs., 2 tables.

Tatchum, C. N., Tabod T. C., Koumetio F. and Manguelle-Dicoum E., 2011: *A gravity model study for differentiating vertical and dipping geological contacts*. Geophysica, **47** (1-2), 43-55.